UC Irvine

UC Irvine Electronic Theses and Dissertations

Title

Engineered Artificial Cu Proteins: Investigating the Effects of the Local Environment

Permalink

https://escholarship.org/uc/item/6592k9zj

Author

Mann, Samuel I.

Publication Date

2017

Peer reviewed|Thesis/dissertation

eScholarship.org Powered by the California Digital Library
University of California

UNIVERSITY OF CALIFORNIA,
IRVINE

Engineered Artificial Cu Proteins: Investigating the Effects of the Local Environment

DISSERTATION

submitted in partial satisfaction of the requirements
for the degree of

DOCTOR OF PHILOSOPHY

in Chemistry

by

Samuel I. Mann

Dissertation Committee:
Professor A. S. Borovik, Chair
Professor William J. Evans
Assistant Professor Jenny Y. Yang

2017

Chapter 2 © 2016 American Chemical Society
© 2017 Samuel I. Mann

DEDICATION

To my parents,
for embracing who I am,
for igniting my curiosity,
for pushing me when I need it most

Better to remain silent and be thought a fool than to speak out and remove all doubt.
–Abraham Lincoln

TABLE OF CONTENTS

LIST OF FIGURES

Page

LIST OF SCHEMES

Page

LIST OF TABLES

Page

LIST OF EQUATIONS

Page

ACKNOWLEDGMENTS

My experience at UCI has been influenced by a number of people. First, I would like to thank my advisor, Andy, who has truly helped me grow as a scientist. Your confidence in me, despite some of the dark times we saw with this project, has helped me develop my own scientific self-confidence. Working on AMP has tested us both in many ways, but your encouragement and utter certainty that we would succeed kept me going. Thank you for letting me explore the paths that this chemistry took me down, even when it wasn't the path we set out for ourselves. I am excited to build upon the foundation you helped me build for myself and I hope, somewhere along the way, I can acquire your gifts of mentoring and inspiring young scientists. I also want to thank my committee, Bill and Jenny. Bill, your visit to Cal Poly convinced me to come to UCI and now you are here at end, thank you for always being interested and engaged whenever we talked about science. Jenny, you have been a wonderful resource for me, thank you for listening to my electrochemical problems and for helping me choose the path I am taking next.

I have been fortunate to work with a group of talented scientists. I was able to learn so much from the my senior labmates, Dave, Nate, Jon, Sarah, Ethan, Taketo, and Yohei, thank you for welcoming me into the group and always being willing to talk with me about science. Jon, thank you for braving the unknown waters of biotin and Sav and for developing the foundation of AMP that I still build upon today: *One metal to rule them all, one ligand to find them, biotin to bring them all, and in the protein bind them.* Thank you for teaching me how make molecules, for showing me column chromatography can be "fun", and for the best advice anyone can give, "Don't f*ck up". And thank you for being my friend, I knew you were always there when things were not going my way in lab. Sarah, thank you for always being willing to talk with me, for reading every document I wrote (even at the last minute!), and for introducing me to Bad Life Choices and Sharks with Lasers. Ethan, you are one of the most skilled scientists I know and I thank you for helping me do my experiments correctly and efficiently. And thank you for always seeing any Marvel movie with me! Jason and Nate, thank you for going through this whole process right alongside me. From the beginning to the end, we have all grown a lot and you both will always be my bros. The group has also recruited many capable scientists after I joined, Victoria, Kelsey, Noam, Maisha, Justin (TMEDA), Lisa, Suman, Sunny, Dolores, Justin (the younger), and Deborah. Thank you all for making the lab a place I enjoyed working every day. Victoria, thank you for keeping my stomach full, for letting me touch the EPR spectrometer (despite your better judgment), and for keeping me humble. Kelsey, Lisa, and Deborah thank you for being as excited about AMP as I have been for the last 5 years and as I pass the torch to you I am excited to see where you will take it.

I had the privilege of working with many scientists outside of our lab, as well. I have to thank the Ward lab for hosting me for 5 weeks while I learned about protein chemistry. A special thank you to Tillmann for teaching me protein crystallography, for sitting with me for hours in the Biozentrum building models of our compounds, and for all of the discussions we had about the power of this approach. I also owe many thanks to the Poulos lab for putting up with my constant presence, especially Dr. Li who always answered all of

my (probably stupid) questions and generously let me send innumerable crystals with them to the synchrotron.

My friends and family outside of the lab have played an important role throughout my time here: you all have kept me sane. Thank you to all of my friends who make sure I have a life outside of lab. Hannah, Kyle, Andrew, Andrea, Gerald, Lindsay, Alana, and Will thank you for letting me bore you with chemistry and for the beerfests, rage cage, and duffys.

Hannah I owe you the biggest thanks of all. Thank you for being with me through the hard times that grad school presents, even when I was not very pleasant to be around. You have a special gift of inspiring me to do better and be better in everything I do. Thank you for loving food as much as I do, we have done so much dining and cooking that are true bright points in my life. I'm not sure I could have done this without you

To my mom and dad, thank you for everything you have done for me. You have always supported me in everything I do and have encouraged me to learn as much about the world as I possibly can. Thank you for letting me be me. I owe you both more than I can ever express, but know that I would not be here without you.

CURRICULUM VITAE

Samuel I. Mann

Education:

- **California Polytechnic State University, San Luis Obispo**
  B.S., *cum laude*, Chemistry, June 2012

- **University of California, Irvine**
  Ph.D. in Chemistry, July 2017
  Research Advisor: A. S. Borovik

Awards Received:

- Outstanding First Year Chemistry Student, Cal Poly 2009
- Dissertation Fellowship, University of California, Irvine 2017

Presentations:

- **Mann, S.I.;** Grau, W.; Mackenzie, M.; McMahon, M.; Immoos, C.E.; Costanzo, P.J. Utilizing "click chemistry" to incorporate MnSOD mimics into polymer scaffolds. Abstracts of Papers, 243rd ACS National Meeting, San Diego, CA, March 25-29, 2012.

- **Mann, S.I.;** Grau, W.; Immoos, C.E.; Costanzo, P.J. Utilizing "click chemistry" to incorporate MnSOD mimics into polymer scaffolds. Cal. State University Undergraduate Research Competition, Long Beach, CA, 2012 (Runner-Up)

- **Mann, S.I.**; Heinisch, T.; Ward, T.R.; Borovik, A.S. Engineered Artificial Metalloproteins: Investigating the effects of the local environment on the function of biologically relevant Cu(II) centers. Bioinorganic Gorodon Research Seminar, Ventura, CA, January 29-February 1, 2015.

- **Mann, S.I.**; Heinisch, T.; Ward, T.R.; Borovik, A.S. Artificial Metalloproteins: Development of a Blue Copper Center. Bioinorganic Gorodon Research Seminar, Ventura, CA, January 29-February 1, 2016.

- **Mann, S.I.**; Heinisch, T.; Weitz, A.; Hendrich, M.P.; Ward, T.R.; Borovik, A.S. Artificial metalloproteins: Towards a blue copper center. Abstracts of Papers, 251st ACS National Meeting, San Diego, CA, March 25-29, 2016.

- **Mann, S.I.**; Heinisch, T.; Weitz, A.C.; Hendrich, M.P.; Ward, T.R.; Borovik, A.S. Building Copper Active Sites in Artificial Metalloproteins. Bioinorganic Gorodon Research Seminar, Ventura, CA, January 29-February 1, 2017.

Publications:

- **Mann, S.I.;** Heinisch, T.; Weitz, A.C.; Hendrich, M.P.; Ward, T.R.; Borovik, A.S. "Modular Artificial Cupredoxins" *J. Am. Chem. Soc.* **2016**, *138*, 9073-9076.
    - **Commentary:**
        - Perkel, J.M. "Metalloprotein Mimicry with Biotin-Streptavidin" *J. Am. Chem. Soc.* **2016**, *138,* 8984.

- **Mann, S.I**.; Heinisch, T.; Ward, T.R.; Borovik, A.S. "Coordination Chemistry within a Protein Host: Regulation of the Secondary Coordination Sphere" *In preparation*.

- **Mann, S.I.**; Heinisch, T.; Ward, T.R.; Borovik, A.S. "Hydrogen Bond Regulation of Peroxide Activation in Artificial Cu Proteins" *In preparation*.

Activities:

- Member of American Chemical Society 2011 – Present

- Alpha Chi Sigma – Professional Chemistry Fraternity 2010 -Present

- Outreach – San Diego Festival of Science and Engineering 2016 – 2017

ABSTRACT OF THE DISSERTATION

Engineered Artificial Cu Proteins: Investigating the Effects of the Local Environment

By

Samuel I. Mann

Doctor of Philosophy in Chemistry

University of California, Irvine, 2017

Professor A. S. Borovik, Chair

The function of metalloproteins can be directly linked to the local environment around the metallo-cofactor. This environment includes direct covalent interactions of amino acid residues and the metal ion, as well as non-covalent interactions proximal to the metal center. The non-covalent interactions include hydrogen bonds (H-bonds) from amino acid residues, as well as extended H-bonding networks that include structural water molecules. Synthetic systems have been designed that include non-covalent interactions within their secondary coordination sphere, however it is often difficult to control and predict these interactions. In this dissertation, an approach has been employed to model the active sites of metalloproteins that utilizes bio-conjugates of metal complexes immobilized within a protein host. Using biotin-streptavidin (Sav) technology, artificial metalloproteins (ArMs) have been prepared that leverage the attributes of protein chemistry with the versatility of synthetic chemistry. Using this approach, control over the primary coordination sphere was demonstrated by developing artificial metalloproteins containing Type I Cu centers like those found in cupredoxins. These ArMs utilize a series of biotinylated Cu^{II} complexes with spacers between the biotin and the metal complex of

variable length that controlled the location of the metal ion within Sav. Anchoring these Cu^{II} complexes within Sav S112C allowed for the study of a series of 4-coordinate Cu complexes with a coordinated thiolate ligand. In addition to controlling the primary coordination sphere, the secondary coordination sphere can be controlled by altering the H-bonding interactions to ligands bound to the Cu center. This control was initially shown through equilibrium binding studies of Cu^{II}-azido complexes. X-ray diffraction (XRD) measurements showed the azido ligand H-bonded to residues and/or structural water molecules within Sav WT. These H-bonds were further employed to stabilize reactive Cu^{II}–OOH species. Cu^{II}–OOH species are known to be highly unstable at room temperature but confinement within Sav WT rendered stable complexes with a half-life of over 1 day. The Cu^{II}–OOH species was also generated *in crystallo* and the structure revealed an O–O ligand coordinated to the Cu center. In addition, the Cu^{II}–OOH unit is involved in an H-bonding network: the proximal O-atom is H-bonded to a structural water molecule and the distal O-atom is H-bonded to the N49 residue. This is the only example of a structurally characterized Cu-peroxido species that has an H-bond to the distal and proximal oxygen atoms. A series of Sav variants were used to systematically delete H-bonding interactions to the hydroperoxido ligand. Removal of the H-bond to the distal O-atom of the hydroperoxido ligand did not affect solution stability, while removal of the H-bond to the proximal O-atom drastically reduced the stability of the Cu^{II}–OOH and elicited reactivity with an external substrate. For Cu-proteins such as LPMOs, these findings support the premise that H-bonds to the distal O-atom are necessary to produce reactive species.

CHAPTER 1

Introduction

Nature utilizes metalloproteins to perform chemical transformations with selectivities and activities that have long been the source of inspiration for synthetic chemists.[1–3] These proteins contain metal ion(s) within their active sites where the reactivity and selectivity are imbued by the microenvironment surrounding the metal ion. In addition to the direct covalent interactions of the protein or substrate with the metal center (the primary coordination sphere), it has been shown that the non-covalent interactions that comprise the secondary coordination sphere of the active sites, are vital in regulating electronic and structural properties.[4–6] The amino acids residues and water molecules neighboring the metal cofactor provide many of these interactions, including hydrogen bonding (H-bonding) networks, steric interactions, and electrostatic/hydrophobic interactions. These non-covalent interactions aid in regulating substrate access to the active site, restricting aggregation with other metal ions, and preventing reactive species from performing unwanted reactions, such as oxidation of the protein.

One family of metalloproteins where the primary coordination sphere plays an important role are cupredoxins. These proteins contain a mononuclear Cu center (referred to as a Type I Cu center) and play a central role in biological electron-transfer.[7] The Cu active sites are best described as trigonal monopyramidal where the trigonal plane contains two N-atom donors from histidine residues and one S-atom donor from a cysteine thiolate; the weakly coordinated axial ligand can vary but is often an S-atom from a methionine (Fig. 1-1). The $Cu^{II}–S_{cys}$ bond is highly covalent, leading to intense ligand-to-metal charge transfer (LMCT) bands which give these proteins the colloquial name, blue copper proteins. The

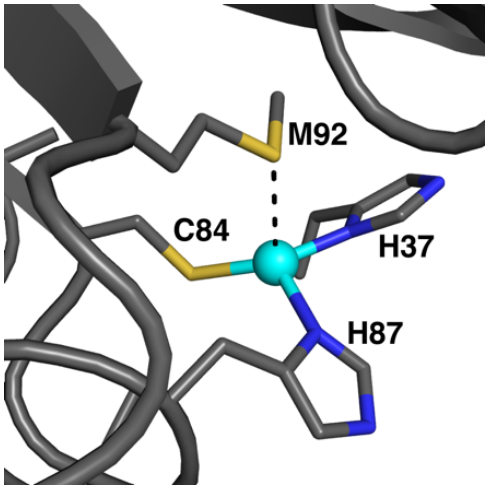

Figure 1-1. Crystal structure showing the Type 1 Cu site in plastocyanin (PDB: 1PLC).

unique primary coordination sphere also tunes the relatively high redox potential of the copper centers (180-800 mV vs. NHE)[7] and, further allows for rapid electron transfer. Unlike other Cu^{II} sites, the trigonal monopyramidal geometry enforced by the protein promotes rapid conversion between the Cu^{I} and Cu^{II} oxidation states. The large range in reduction potential is also derived from changes within the primary coordination sphere of the Cu centers: "perturbed" cupredoxins exists that employ different ligands leading to distorted geometries.[8–10]

In conjunction with the primary coordination sphere, the non-covalent interactions surrounding active sites are also vital in metalloproteins, the most prevalent of which are H-bonds. These interactions arise from H-bond acceptors/donors within the microenvironment of the active site, such as amino acid residues and water molecules, that can often interact with substrates and ligands coordinated to the metal ion. Many metalloproteins utilize H-bonds to regulate the activation of small molecules such as O_2, in which key dioxygen-derived species are stabilized by H-bonds within their active sites.

The interplay of the primary coordination sphere with regulatory H-bonds is striking

in heme proteins, such as hemoglobin (Hb) and cytochrome P450s (P450s). Hb is an oxygen transport protein in which dioxygen reversibly binds to an open coordination site on an Fe^{II}-heme cofactor. A number of features in the active site of Hb have been identified as contributors to the reversible binding of O_2. First, the primary coordination sphere includes an axially coordinated histidine residue that donates enough electron density to the Fe^{II} center to bind dioxygen without cleaving the O–O bond. In addition, the Fe-O_2 unit is stabilized by a bifurcated H-bond from a neighboring histidine residue which interacts with both the proximal (coordinated to the metal center) and distal O-atoms (Fig. 1-2A).[11,12] The importance of these interactions is further evident when compared to the active sites in P450s which have Fe-heme active sites axially coordinated by a cysteine residue. The strong thiolate donor promotes activation of dioxygen and subsequent oxidation of strong C–H bonds.[13] The secondary coordination sphere also plays a vital role where, unlike in Hb, P450s have H-bonds to only the distal O-atom of the hydroperoxido ligand, which promotes O–O bond cleavage (Fig. 1-2B).[1,14–18] In fact, mutation of the threonine, which H-bonds to the Fe–OOH unit, to an alanine disrupts hydroxylation activity and instead hydrogen peroxide is released.[16]

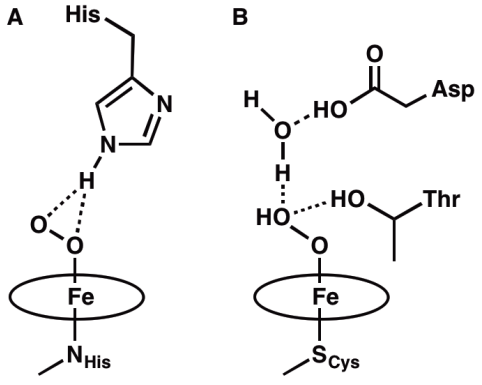

Figure 1-2. ChemDraw representation illustrating the H-bonding interactions in the active sites of (**A**) oxy-Hb (PDB: 1GZX)[12] and (**B**) P450s.[15,16] Circles represent protoporphyrin IX.

Similar to the heme proteins described above, H-bond regulated M-O_2 units are thought to be an important component of the catalytic cycles in Cu metalloenzymes. For instance, a Cu^{II}-OOH species is a hypothesized active intermediate in the Cu-containing dopamine β–monoxygenase (DβH). There has been no structural data collected for the dioxygen bound form of the protein; however, mechanistic studies have suggested that, similar to P450s, the hydroperoxido ligand is activated via a H-bonding interaction to the distal oxygen of the proposed Cu^{II}-OOH species by a nearby tyrosine residue.[19,20]

The examples discussed thus far have focused on the H-bonding interactions close to the active sites, however long-range H-bonding networks are important as well. The outer sphere H-bonding network present in cytochrome *c* oxidase (C*c*O) is one example. The protein's extensive H-bond network helps shuttle protons and electrons between the solvent and the active site buried deep within the protein matrix (> 30 Å, Fig. 1-3).[21] The primary, secondary, and outer coordination spheres in CcO, as well as the previously mentioned

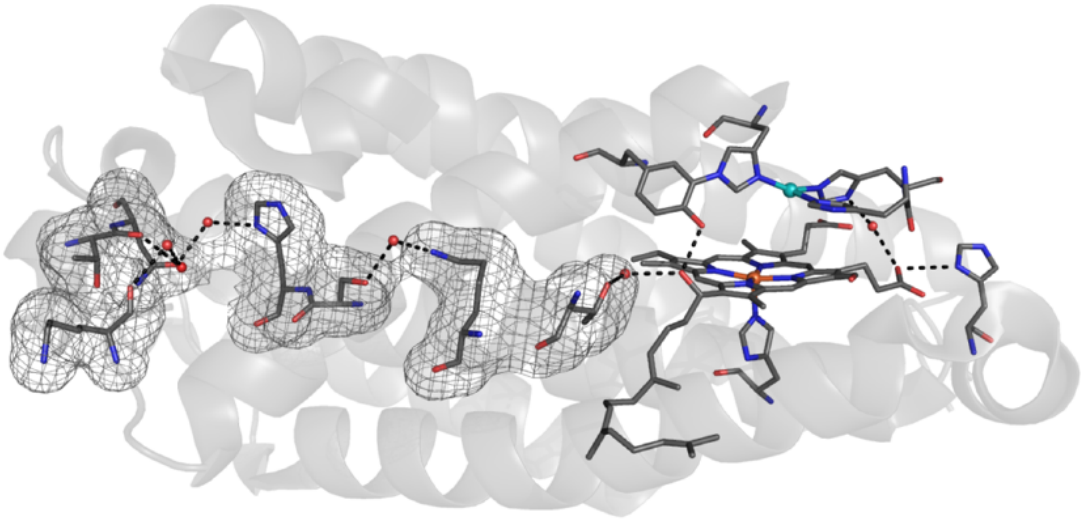

Figure 1-3. Crystal structure of C*c*O with the H-bonding channel spanning > 30 Å from the protein surface to the active site indicated by the grey mesh (PDB: 1V54).

metalloproteins, have inspired the creativity of synthetic inorganic chemists and helped to evolve molecular design.

Lessons from Nature: Molecular Design

Inspired by the active sites of metalloproteins, synthetic inorganic chemists have strived to develop systems that can access the types of reactivity and selectivity that has evolved in nature. After over 100 years of study on coordination compounds,[22] synthetic inorganic chemists have developed the ability to precisely control the primary coordination sphere of metal complexes. However, regulation of the weaker, non-covalent interactions found in metalloproteins has proven more difficult within synthetic compounds. In an effort to understand how to effectively control the secondary coordination sphere around metal complexes, a few key design principles have been established. Often, these designs include the use of rigid organic ligand scaffolds which can be functionalized with sterically bulky and/or H-bonding groups to prevent reactive species from performing unwanted chemistry, much like the protein matrix does for metal cofactors.

One of the earliest examples of a molecular system incorporating H-bonding groups was reported by Collman who developed the picket fence porphyrin to mimic the chemistry of hemoglobin and myoglobin (Fig. 1-4). Generally, free Fe^{II}-heme compounds (i.e., outside of a protein) form Fe^{III}–O–Fe^{III} dimeric species upon reaction with dioxygen.[23,24] To prevent this, Collmann installed pendant pivalamide functional groups to "fence off" one face of the porphyrin. These bulky groups, along with an axially coordinated methylated imidazole, accurately reproduced the primary coordination sphere and hydrophobic environment of Hb/Mb and allowed for reversible binding of dioxygen. In addition, the Fe-O_2 adduct was stable enough for structural characterization by X-ray diffraction (XRD) methods.[25,26]

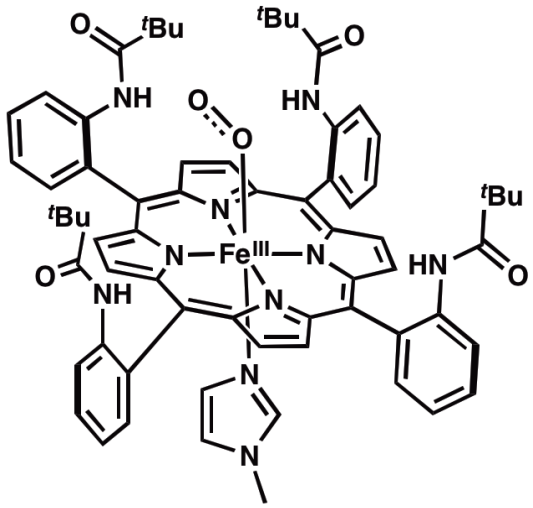

Figure 1-4. ChemDraw representation of the Fe-O_2 adduct stabilized by Collman's picket-fence porphyrin.

Despite the success of this design, the pivalamide groups were originally designed to donate H-bonds to the coordinated O_2 ligand but, based on the structure, these groups were >5 Å from the O_2 ligand, making H-bonding interactions impossible. In light of this, new derivatives were synthesized to place the H-bond donors closer to the Fe-O_2 species. One of these new ligands was functionalized with a phenylurea moiety in place of one of the amides and led to an enhancement of O_2 affinity attributed to the H-bond donor groups (Fig. 1-5).[27] From these design principles, more advancements have been made in ligand designs, beyond porphyrins, that incorporate pendant functional groups for H-bonding interactions as well as to assist in substrate binding.

One lesson learned from the work by Collman and others on picket fence porphyrins was that a rigid ligand is key to properly positioning H-bonding donors/acceptors in close proximity to the metal center for the non-covalent interaction to occur within the secondary coordination sphere. There are many reported examples of ligand scaffolds containing H-bond donating/accepting groups,[5,28–30] but one popular approach utilizes a tripodal ligand

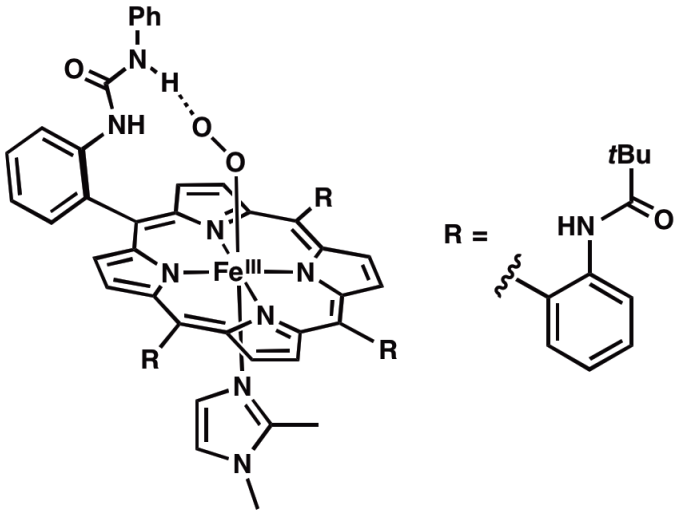

Figure 1-5. Picket fence porphyrin bearing a phenyl-urea moiety that can donate H-bonds to the Fe-O_2 unit (H-bond indicated by a dashed line).

framework. One excellent example relevant to the work presented in the following chapters is that of Masuda. Building off the success of Collman's use of the pivalamide functional group, Masuda and coworkers prepared a tripodal, tetradenate pyridine based ligand (bppa, bis(6-pivalamide-2-2pyridylmethyl)-(2-pyridylmethyl)amine) that was able to stabilize a Cu^{II}–OOH species (Fig. 1-6). These species are usually unstable at room temperature, with the H-bonds forming between the proximal O-atom of the hydroperoxido ligand and the amide N–H groups – these interactions provided enough thermal stability to acquire the first crystal structure of a Cu^{II}-OOH species.[31] To probe the effects of H-bonding interactions on the electronic structure of Cu^{II} complexes, Masuda also developed a series of tripodal ligands that had three, two, one, or zero H-bond donor groups (in the form of amino substituted pyridines) (Fig. 1-7) around a Cu center. These ligands were used to study the electronic and structural effects of increasing number of H-bond donors on a series of Cu^{II}-N_3 and μ-1,2-peroxo dinuclear Cu^{II} complexes. They found that having more H-bond donors resulted in a lengthening of the Cu–N_{azido} or Cu–$O_{peroxido}$ bond lengths and a decrease in the intensity of

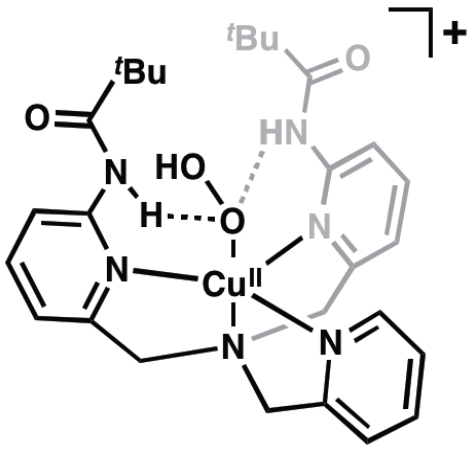

Figure 1-6. $[Cu^{II}(bppa)(OOH)]^{+}$ species stabilized by H-bonds (indicated by dashed lines) from pivalamide functionalized pyridines.

the N_3–Cu^{II} or peroxide–Cu^{II} LMCT band.[32]

Synthetic Chemistry and Beyond

The success of Masuda and others provided a strong foundation for the importance of incorporating control of the secondary coordination sphere into the designs of metal complexes. These compounds, however, did not incorporate the more complex interactions found in metalloproteins that help transport substrates to the active site. The next logical step was to merge synthetic chemistry and biology to develop more complex ligand scaffolds that incorporate longer range interactions capable of eliciting faster or more selective catalysis.

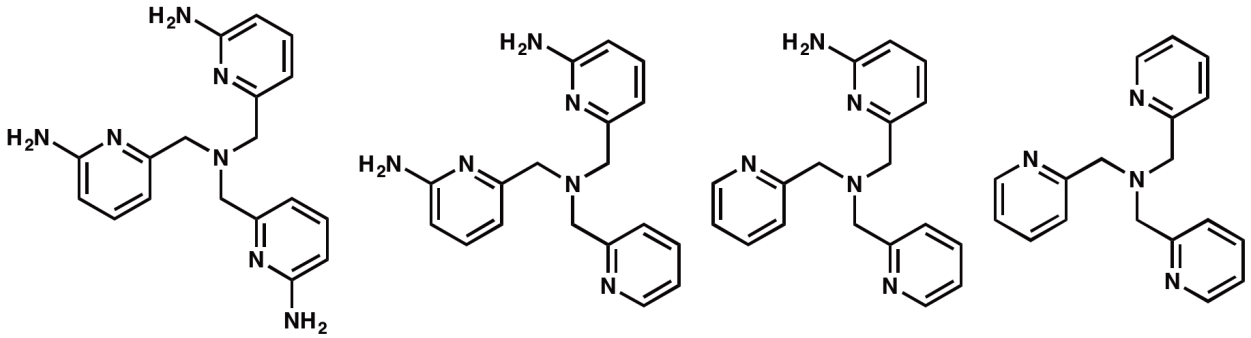

Figure 1-7. Tripodal pyridylamine ligands with three, two, one, or zero H-bond donor groups.

One example that integrated these design principles into synthetic metal complexes was the development of a family of Ni complexes for electrocatalytic H_2 production and oxidation. DuBois first reported a mononuclear Ni complex with two diphosphine ligands ($P^R_2N^{R'}_2$) that contain pendant amine moieties that are necessary for function: their role is to assist in proton-transfer to and from the Ni center (Fig. 1-8A).[33,34] Recently, this system was elaborated on by Shaw to include amino acid residues or short peptides that assist in controlling the microenvironment around the catalyst. Many different amino acid residues were incorporated into the ligand scaffold, but the most active catalyst utilized the ligand $P^{Cy}_2N^{Arg}_2$ which places the guanidiunium groups of arginine in the secondary coordination sphere of the complex (Fig. 1-8B).[35,36] These groups were thought to not only provide an additional proton relay along the pseudo-proton channel (highlighted in red in Figure 1-8B) but also have a structural role. The authors provided evidence that the arginine-arginine interactions could assist in maintaining a shorter Ni···N distance which is important for rapid turnover.[35] With this is mind, Shaw and coworkers also prepared a series of complexes functionalized with larger peptides in the hopes of adding a more stable secondary sphere structure, much like metalloproteins. This approach proved relatively successful, increasing

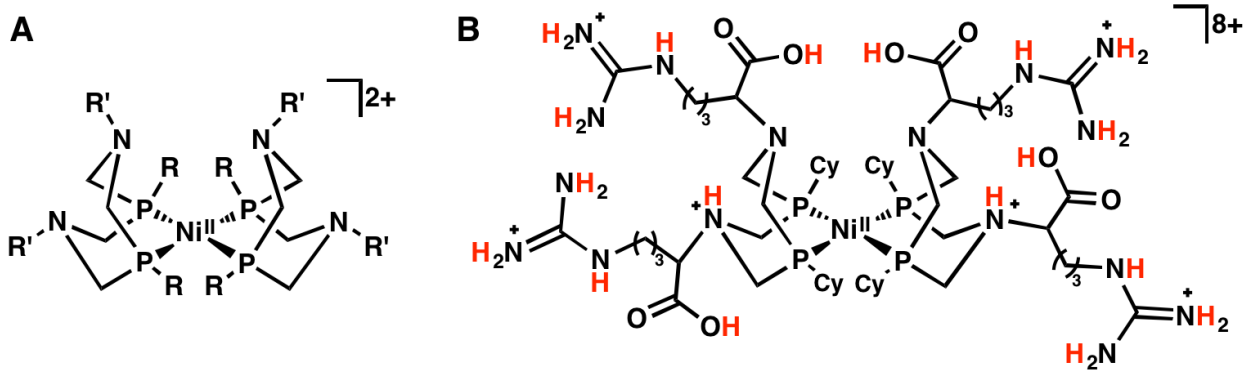

Figure 1-8. Schematic of Ni^{II} complexes (**A**) $[Ni^{II}(P^R_2N^{R'}_2)]^{2+}$ and (**B**) $[Ni^{II}(P^{Cy}_2N^{Arg}_2)]^{8+}$ with pendant amines in the secondary coordination sphere. In **B**, the pseudo-proton channel is highlighted in red.

the catalytic activity two-fold relative to the peptide-free complex. They owed this enhancement to the peptide hairpin structure that is maintained in solution. Despite the structural stability of the hairpin in solution, they found significant "hinge-like" flexibility around the linker limiting the desired enzyme-inspired positioning and making it difficult to attribute enhanced rates to any particular functional group.[36,37]

Best of Both Worlds: Artificial Metalloproteins

One of the lessons learned from the examples discussed above, is that inclusion of more complex networks of non-covalent interactions can drastically affect the rates of catalysis as well as allow for the stabilization of reactive intermediates. A new field of bioinorganic chemistry has emerged, which takes advantage of the structural matrix provided by proteins to prepare artificial metalloproteins (ArMs). There are many approaches to the development of ArMs, a few of which are discussed below.[38–47]

One approach is the combination of metal ions with longer peptides, much like the work by Shaw, however the primary coordination sphere is provided by amino acid residues within the protein matrix. The most studied methods utilizes *de novo* designed single-chain peptides that fold into three- or four-helix bundles where the metal binds to residues within the interior of the artificial protein.[48] DeGrado has developed a series of *de novo* designed *due ferri* proteins that contain a di-iron active site within a four-helix bundle. These di-iron proteins have primary coordination spheres matching native proteins with either a 2-His/4-carboxylate[49] or 3-His/4-carboxylate[50] motif (Fig. 1-9) and have O_2 reaction rates similar to natural di-iron proteins. By altering the primary coordination sphere the reactivity can be altered to either selectively oxidize 4-aminophenol to the benzoquinone monoimine or N-

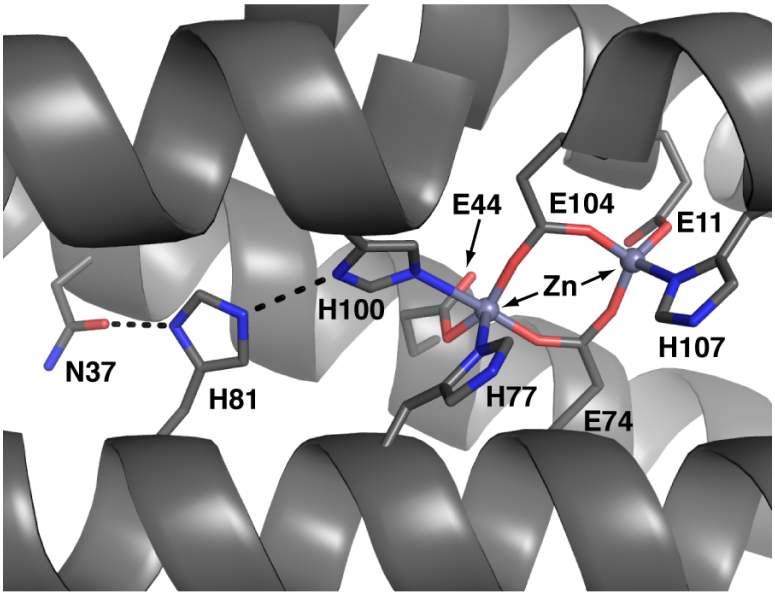

Figure 1-9. NMR structure of the di-Zn^{II} adduct of *de novo* designed four-helix bundle with a 3-His/4-carboxylate motif capable of N-hyroxylation of *p*-anisidine (PDB: 2LFD). The H-bonding network shown (indicated by dashed black lines) helps position H100 to coordinate to the metal center.

hydroxylate *p*-anisidine. Additionally, the secondary coordination sphere of these helix bundles can be altered to allow for increased access by solvent and substrate.[51,52]

ArMs have also been created by merging synthetic inorganic chemistry with natural proteins. This approach has been utilized in a variety of ways, including incorporation of unnatural metal porphyrin and salen complexes into myoglobin[39,53–55] or semi-synthetic construction of [Fe,Fe]-hydrogenase.[56] In another example, Ménage and coworkers showed that inclusion of the synthetic metal complex FeL (L = *N*-benzyl-*N*'-(2-hydroxybenzyl)-*N*,*N*'-ethylenediaminediacetic acid) into the apo form of the Ni-binding protein NikA produced an artificial metalloenzyme capable of intramolecular arene hydroxylation. The Fe complex was held in place via H-bonding and hydrophobic interactions with the protein host (Fig. 1-10). This system also provided a means of probing the hydroxylation mechanism via XRD methods. Single crystals of NikA could be soaked in a solution of FeL before being anaerobically reduced. The iron-containing crystals were then exposed to dioxygen before

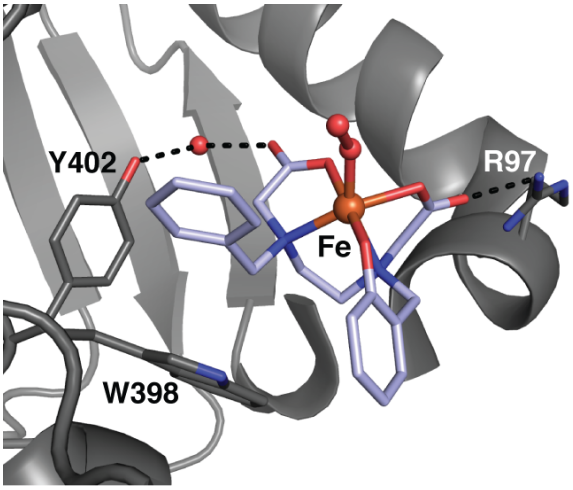

Figure 1-10. Structure of the Fe–O_2 adduct of FeL in NikA (L is shown in pale blue). H-bonds are shown as dashed lines (PDB: 3MVY).

being frozen at different time intervals. This study allowed for the determination of the structure of four intermediates in the catalytic cycle, including a rare Fe-O_2 adduct (Fig. 1-10).[57] The crystallographic component of this ArM illustrates a major advantage of studying an artificial system to understand native metalloproteins; metalloenzymes often do not crystallize well and their reaction rates can be too rapid to be trapped crystallographically. One limitation of this approach, however, is the inability to expand on the primary coordination sphere beyond the basic EDTA framework.

Biotin-streptavidin (Sav) technology offers a different approach to ArMs. Taking advantage of Sav's affinity for biotin ($K_a \sim 10^{13}$ M^{-1}), synthetic metal complexes can be functionalized with biotin (biotinylated) and reproducibly anchored in Sav. This method was introduced by Whitesides, who developed an artificial metalloenzyme with Sav containing a Rh complex that was capable of catalyzing asymmetric hydrogenation.[58] Further expanding on this approach, Ward has prepared a large number of artificial metalloenzymes with various biotinylated organometallic complexes that have impressive catalytic function (Fig. 1-11).[40,41] In addition to the synthetic freedom allowed by biotin-Sav, site-directed

mutagenesis opens the door for studying the effect of amino acid residues in the secondary coordination sphere on catalysis. This approach offers a range of variables to manipulate the activity and selectivity of a particular ArM. For instance, one study focused on a series of Ir, Ru, and Rh piano stool complexes for transfer hydrogenase reactivity, where initial screening elucidated the Ru-based complex as the most active catalyst in Sav wild-type (WT). Sav mutants were then screened to determine the ideal makeup of the secondary coordination sphere for reactivity. When a nearby serine residue was mutated to an aromatic residue, one enantiomer was produced, while mutation to cationic residues produced the opposite enantiomer. It was postulated that these different residues assisted in orienting one face of the substrate or the other with respect to the Ru cofactor.[59]

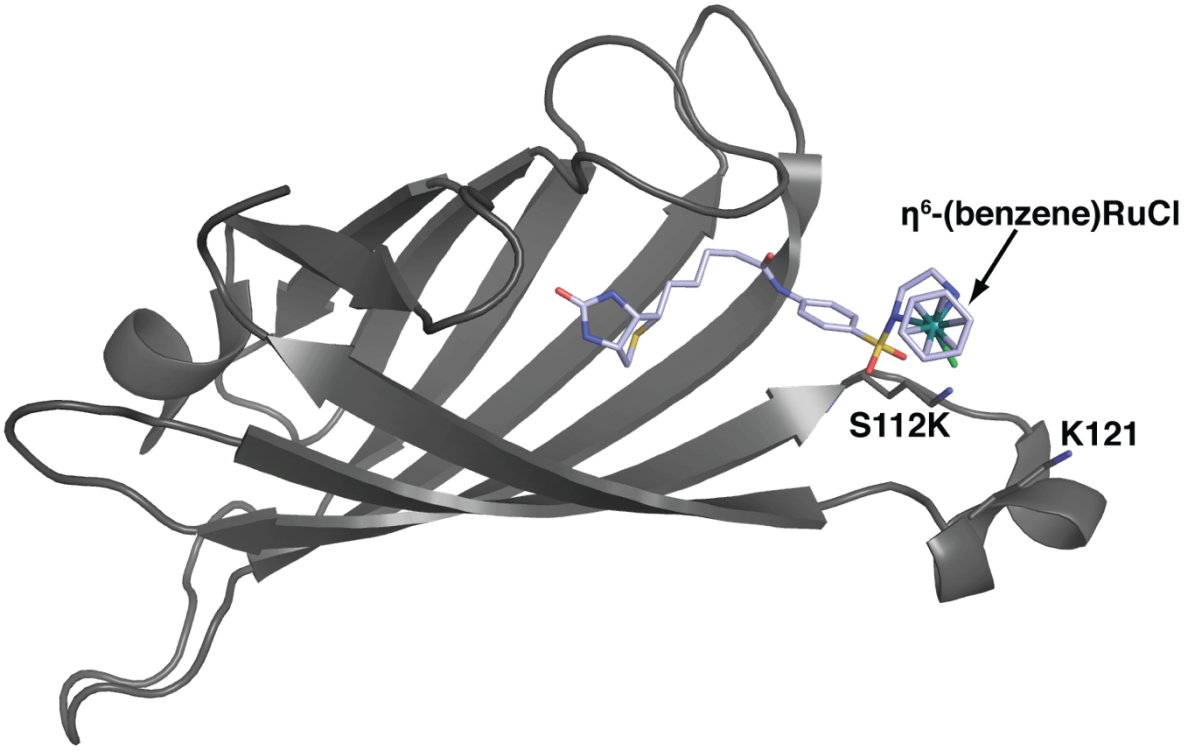

Figure 1-11. Structure of a Sav ArM with an anchored biotinylated Ru complex (PDB 2QCB) used by Ward with the nearby residues that were mutated in the study. The biotinylated Ru complex is in light gray.

Previous Work in the Borovik Lab

The Borovik lab has worked for nearly 25 years to understand how the incorporation of well-defined, intramolecular H-bonds can be used to stabilize reactive species and control their reactivity. A large library of rigid organic ligand scaffolds has been developed to position H-bond donors and/or acceptors in close proximity to the metal.[60–62] These ligands are generally tripodal, tetradenate chelators with N-atom donors containing H-bond donors/acceptors, which surround an open coordination site on a transition metal center. The group has shown the power of this approach through the stabilization of reactive species important to bioinorganic chemistry. For instance, the ligand scaffold $[H_3buea]^{3-}$ (Fig. 1-12), which has ureido groups in the secondary coordination sphere capable of donating intramolecular H-bonds, has been used to stabilize a variety of M-oxido and M-hydroxido complexes. These include the first crystallographically characterized Mn^{III}– and Fe^{III}–oxido complexes.[63–65] The bulky *tert*-butyl groups and rigid H-bonding cavity are responsible for the thermal stability of these complexes.

After having prepared and stabilized these reactive species with static H-bonds in the

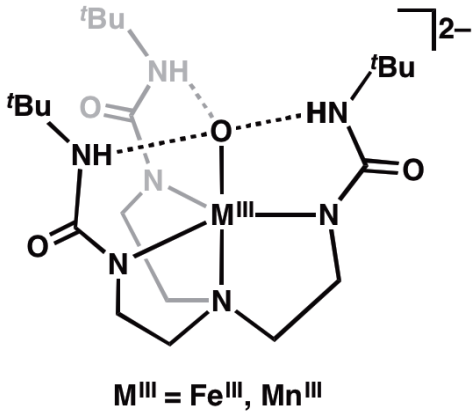

Figure 1-12. Structure of Fe^{III}– and Mn^{III}–oxido complexes with $[H_3buea]^{3-}$ showing intramolecular H-bonds as dashed lines.

secondary coordination sphere, a modified ligand scaffold was prepared to create a more dynamic secondary coordination sphere. This ligand, $[H_2bupa]^{2-}$, maintained two urea arms but replaced the third with a pivalamide-functionalized pyridine. The anionic amidate group could serve as a proton shuttle (much like the pendant amine in the work of DuBois and Shaw discussed earlier). In addition, this anionic group could serve as a strong H-bond acceptor. Mn^{II} complexes with this ligand were shown to catalytically reduce dioxygen to water in the presence of an H-atom source via a detectable Mn^{III}-peroxo intermediate. The amidate group was thought to play two important roles: the first was to shuttle protons to the Mn^{III}-peroxo intermediate and the second was to displace coordinated water molecules to close the catalytic cycle. This system shows the power of molecular design by modifying a known ligand framework to elicit reactivity (Fig. 1-13).[66,67]

These small molecules, however, cannot accurately mimic the long-range interactions found within metalloproteins, such as the ones discussed in C*c*O. Therefore, the challenge remains to develop systems based on inorganic complexes in which a more complex structure can be used to tune the secondary and outer coordination spheres.

Initial efforts towards this goal in the Borovik lab relied on the confinement of metal complexes in porous polymer scaffolds.[68–70] This was accomplished by imprinting a metal binding site using template copolymerization of cross-linking agents with metal complexes bearing polymerizable function groups. The general procedure used a six-coordinate, substitutionally inert Co^{III}salen complex, which served as the template site within the polymer scaffold (Scheme 1-1).[69] Immobilization of the complex was accomplished through three-points of attachments to the polymer host: two from the functionalized salen ligand and one from an axially coordinated ligand. The sixth coordination site was occupied by a

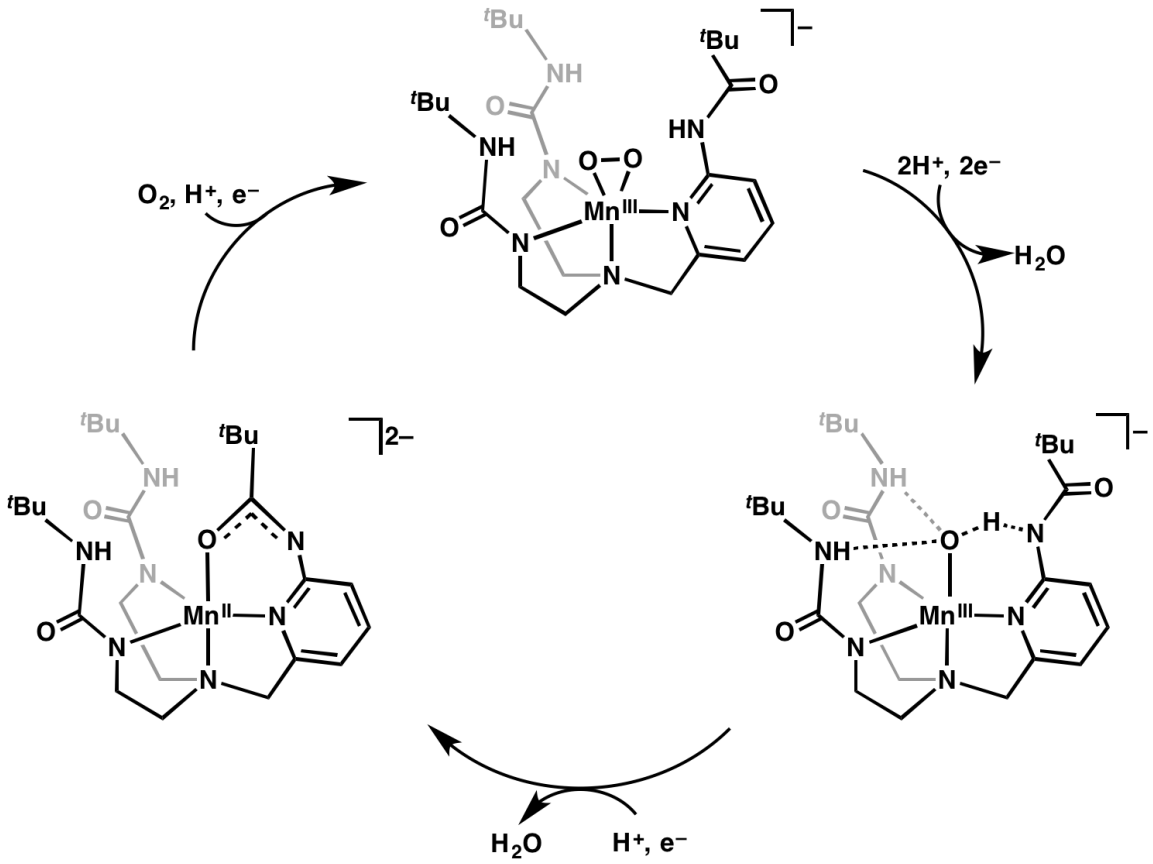

Figure 1-13. Characterized species in the catalytic cycle for O_2 reduction by $[Mn^{II}(H_2bupa)]^-$ showing the multiple roles played by the secondary coordination sphere amidate group.

ligand without a polymerizable functional group, which can be removed post-polymerization to create a void space around the complex for substrates to bind. The metal ion and non-anchored ligand can be removed via chemical modification of the active site. Co^{II} ions can then be reintroduced to create unsaturated four-coordinate complexes embedded within the polymer that can have an additional endogenous ligand from the polymer. This approach led to the preparation of porous materials that reversibly bound O_2. Because only five-coordinate Co^{II}salen could efficiently bind dioxygen, spectroscopic techniques were used to probe the relative amounts of four- vs. five-coordinate sites. It was discovered that there was adequate room around the templated site to result in a dynamic structure giving rise to a distribution of four- and five-coordinate sites in the absence of dioxygen.[69]

Scheme 1-1. The General Procedure for Preparing Metal-Templated Polymer Scaffolds

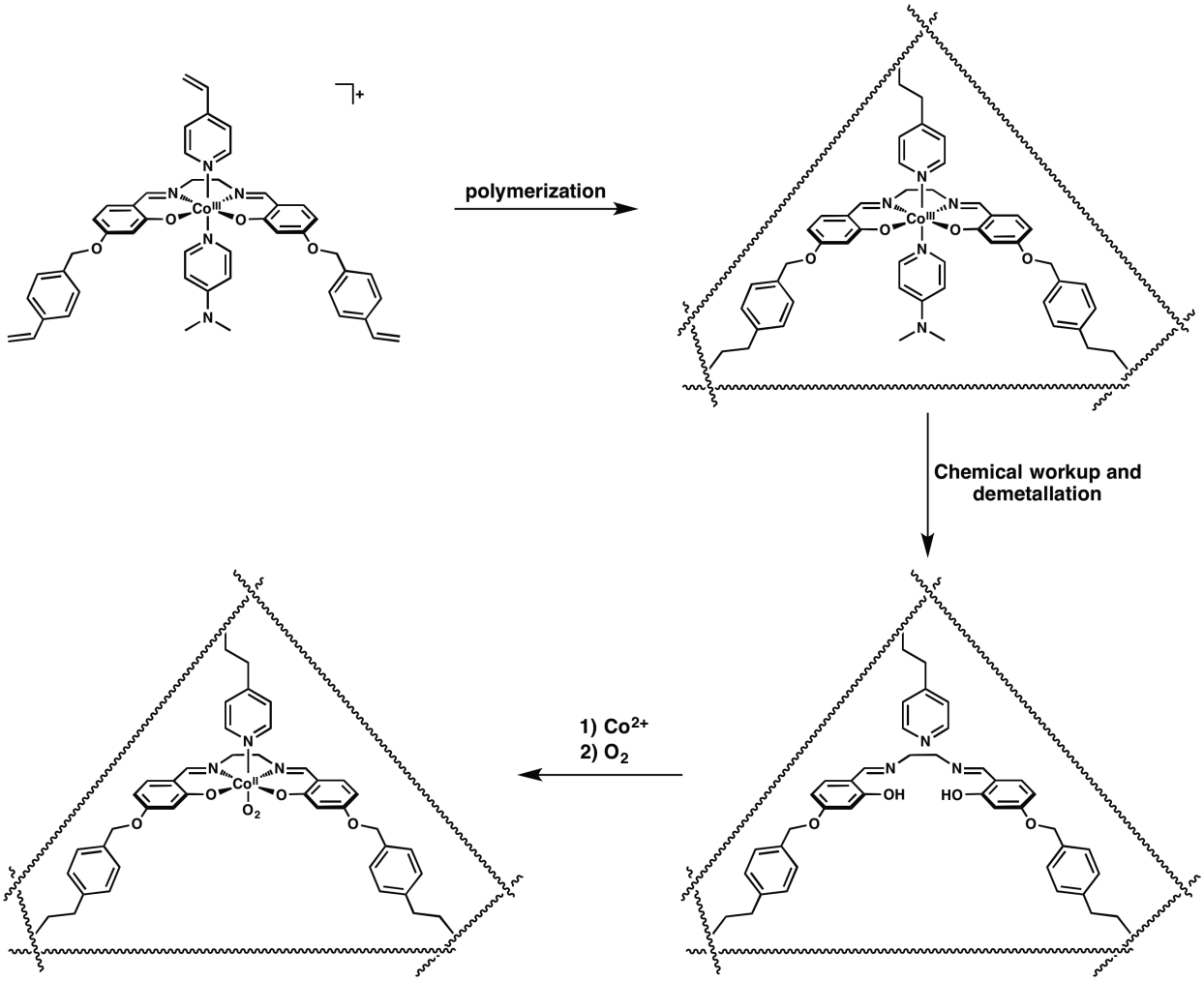

Recent advances in the use of more structurally complex scaffolding to control the secondary coordination sphere around synthetic inorganic complexes led us to explore the development of artificial metalloproteins. Leveraging synthetic chemistry with protein chemistry would allow for the development of structure-function relationships that can be more closely compared to native metalloproteins. The approach that best suited our requirements is that of biotin-Sav technology. In collaboration with the Ward lab, we aimed to apply this approach to the development of biologically relevant active sites. The primary

and secondary coordination spheres could be readily modified via combining biotinylation of ligand scaffolds with protein mutagenesis. We anticipated that this combined usage of synthetic and protein chemistry would be especially advantageous for the development of structure-function relationships in metalloproteins. An additional benefit is the relative ease with which apo-Sav crystallizes, providing the possibility of comparing structural data with spectroscopic studies done *in situ*.

Initial studies of artificial metalloproteins were done by Dr. Jon Paretsky with the Ward lab, and molecular structures of [Cu(Biot-propyl-dpa)]$^{2+}$⊂Sav WT, [Cu(Biot-propyl-dpa)]$^{2+}$⊂Sav S112K, and [Cu(Biot-propyl-dpa)]$^{2+}$⊂Sav S112D (Fig. 1-14) were obtained. These structures demonstrated the efficacy of this approach to insert synthetic Cu complexes into Sav. H-bonding networks were also observed that show the possibility of forming long-range non-covalent interactions between residues and water molecules. These results laid the foundation for me to further develop Cu ArMs to probe the effects of the primary and secondary coordination spheres on confined copper complexes with protein hosts.

Overview of Remaining Chapters

Chapter 2. This chapter reports the synthesis of the biot-n-dpea (n = 2 (et), 3 (pr), or 4 (bu))

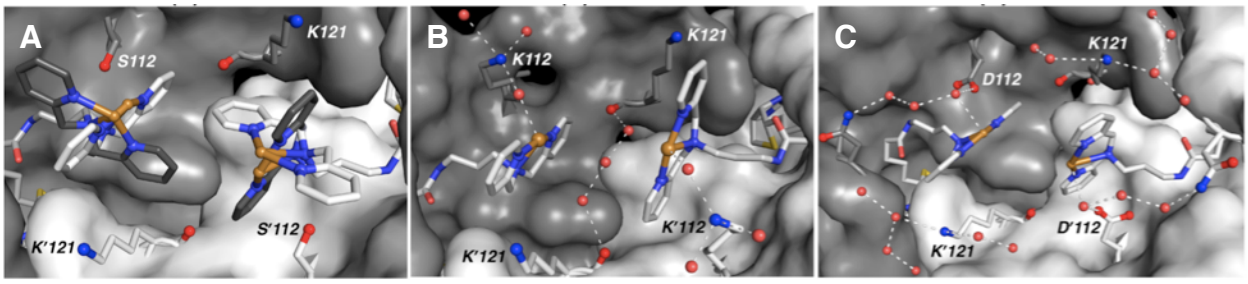

Figure 1-14. X-ray structures of (**A**) [Cu^{II}(biot-propyl-dpa)]$^{2+}$⊂WT Sav, (**B**) [Cu^{II}(biot- propyl-dpa)]$^{2+}$⊂S112K Sav, and (**C**) [Cu^{II}(biot-propyl-dpa)]$^{2+}$⊂S112D Sav. The dashed lines represent H-bonds and red spheres are water molecules. The Cu•••Cu' distances are 7.2 Å (WT), 7.0 Å (S112K), and 6.2 Å (S112D). (A) shows two different orientation of the copper complex in gray and white.

ligand system and the analogous Cu^{II} complexes (Fig. 1-15). The structure of $[Cu^{II}(biot\text{-}et\text{-}dpea)(H_2O)_2]^{2+}\subset$Sav WT was solved and revealed the placement of the Cu center within Sav. In an effort to demonstrate the utility of this approach, I first sought to control the primary coordination sphere of these Cu ArMs by using Sav S112C, a variant that positions a cysteine thiolate near the Cu^{II} center. The series of Cu ArMs $[Cu^{II}(biot\text{-}n\text{-}dpea)S_{cys112}]^{+}\subset$Sav S112C showed new spectroscopic and electronic properties by UV-visible (UV-vis) and electron paramagnetic resonance (EPR) spectroscopies and cyclic voltammetry (CV) relative to their Sav WT counterparts. These spectroscopic properties were dependent on the length of the ligand spacer between the Cu complex and the biotin, and were comparable to the spectroscopic properties of cupredoxins. Finally, these artificial cupredoxins were structurally characterized to correlate the structure to the observed spectroscopic properties.

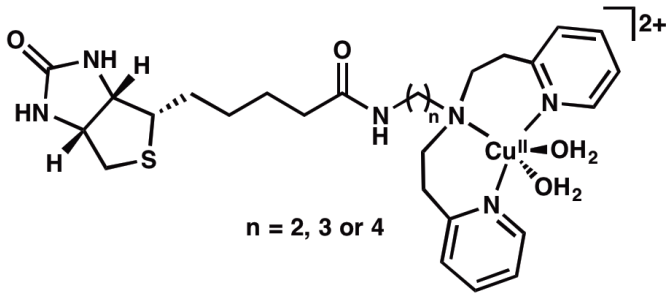

Figure 1-15. Three Cu^{II} complexes used in Chapter 2.

Chapter 3. Having established control over the primary coordination sphere of Cu ArMs using an endogenous donor from Sav, I next wanted to show the coordination of exogenous ligands (besides water from the solvent). Addition of excess NaN_3 to $[Cu^{II}(biot\text{-}n\text{-}dpea)(H_2O)_2]^{2+}\subset$Sav WT (n = et or pr) in solution showed changes in the absorption spectra that were consistent with the coordination of an azido ligand. The azido adducts of these

ArMs were also structurally characterized giving the first example of spectroscopic and structural correlation of exogenous ligands in Sav (Fig. 1-16). The structures of both ArMs revealed that the Cu–N_3 units were involved in H-bonding networks with neighboring amino acid residues and/or water molecules. Removing these interactions via mutagenesis resulted in as much as a two-fold decrease in equilibrium binding constant.

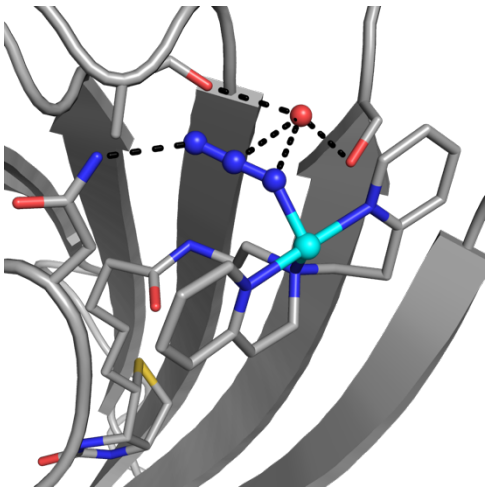

Figure 1-16. Structure of a Cu^{II}–azido ArM studied in Chapter 3.

Chapter 4. Identification of the conserved H-bonding interactions to coordinated water molecules in $[Cu^{II}(biot\text{-}et\text{-}dpea)(H_2O)_2]^{2+}\subset$Sav WT or to the coordinated azido ligand in $[Cu^{II}(biot\text{-}et\text{-}dpea)N_3]^{+}\subset$Sav WT suggested this could be exploited to stabilize more reactive species. Initial studies focused on the reaction of Cu^{II} ArMs with H_2O_2 (Scheme 1-2). Addition of excess H_2O_2 to $[Cu^{II}(biot\text{-}et\text{-}dpea)(H_2O)_2]^{2+}$ (without Sav) resulted in the growth of a new absorption by UV-vis assigned to a hydroperoxido–Cu^{II} LMCT. This species was unstable at room temperature, however formation of this species within Sav WT resulted in a stable Cu^{II}–OOH species. Structural characterization showed two H-bonding interactions to the

Scheme 1-2. Example of the Reaction Studied in Chapter 4

$$[Cu^{II}(biot\text{-}et\text{-}dpea)(OH_2)_2]^{2+}\subset \text{Sav WT} \xrightarrow[\text{50 mM MES, pH 6}]{\text{100 } H_2O_2} [Cu^{II}(biot\text{-}et\text{-}dpea)(OOH)]^{+}\subset \text{Sav WT}$$

coordinated hydroperoxido ligand: one between a structural water molecule and the proximal O-atom and another between a neighboring asparagine residue and the distal O-atom. Studies were undertaken to determine the effects that changing these H-bonds had on the stability and reactivity of the Cu^{II}–OOH species.

References

(1) Poulos, T. L. Heme Enzyme Structure and Function. *Chem. Rev.* **2014**, *114* (7), 3919–3962.
(2) Tommos, C.; Babcock, G. T. Oxygen Production in Nature: A Light-Driven Metalloradical Enzyme Process. *Acc. Chem. Res.* **1998**, *31* (1), 18–25.
(3) Stone, K. L.; Borovik, A. Lessons from Nature: Unraveling Biological CH Bond Activation. *Curr. Opin. Chem. Biol.* **2009**, *13* (1), 114–118.
(4) Dawson, J. H. Probing Structure-Function Relations in Heme-Containing Oxygenases and Peroxidases. *Science* **1988**, *240* (4851), 433–439.
(5) Cook, S. A.; Hill, E. A.; Borovik, A. S. Lessons from Nature: A Bio-Inspired Approach to Molecular Design. *Biochemistry* **2015**, *54* (27), 4167–4180.
(6) Capaldi, R. A. Structure and Function of Cytochrome c Oxidase. *Annu. Rev. Biochem.* **1990**, *59* (1), 569–596.
(7) Liu, J.; Chakraborty, S.; Hosseinzadeh, P.; Yu, Y.; Tian, S.; Petrik, I.; Bhagi, A.; Lu, Y. Metalloproteins Containing Cytochrome, Iron–Sulfur, or Copper Redox Centers. *Chem. Rev.* **2014**, *114* (8), 4366–4469.
(8) Solomon, E. I.; Hadt, R. G. Recent Advances in Understanding Blue Copper Proteins. *Coord. Chem. Rev.* **2011**, *255*, 774–789.
(9) LaCroix, L. B.; Randall, D. W.; Nersissian, A. M.; Hoitink, C. W. G.; Canters, G. W.; Valentine, J. S.; Solomon, E. I. Spectroscopic and Geometric Variations in Perturbed Blue Copper Centers: Electronic Structures of Stellacyanin and Cucumber Basic Protein. *J. Am. Chem. Soc.* **1998**, *120* (37), 9621–9631.
(10) Olesen, K.; Veselov, A.; Zhao, Y.; Wang, Y.; Danner, B.; Scholes, C. P.; Shapleigh, J. P. Spectroscopic, Kinetic, and Electrochemical Characterization of Heterologously Expressed Wild-Type and Mutant Forms of Copper-Containing Nitrite Reductase from Rhodobacter Sphaeroides 2.4.3. *Biochemistry* **1998**, *37* (17), 6086–6094.
(11) Perutz, M. F.; Rossmann, M. G.; Cullis, A. N. N. F.; Muirhead, H.; Will, G.; North, A. C. T. Structure of Hæmoglobin: A Three-Dimensional Fourier Synthesis at 5.5-Å. Resolution, Obtained by X-Ray Analysis. *Nature* **1960**, *185* (4711), 416–422.
(12) Paoli, M.; Liddington, R.; Tame, J.; Wilkinson, a; Dodson, G. Crystal Structure of T State Haemoglobin with Oxygen Bound at All Four Haems. *J. Mol. Biol.* **1996**, *256* (4), 775–792.
(13) Green, M. T. CH Bond Activation in Heme Proteins: The Role of Thiolate Ligation in Cytochrome P450. *Curr. Opin. Chem. Biol.* **2009**, *13* (1), 84–88.
(14) Poulos, T. L. Heme Enzyme Crystal-Structures. *Adv. Inorg. Biochem.* **1988**, *7*, 1–36.
(15) Martinis, S. A.; Atkins, W. M.; Stayton, P. S.; Sligar, S. G. A Conserved Residue of

Cytochrome-P-450 Is Involved in Heme-Oxygen Stability and Activation. *J. Am. Chem. Soc.* **1989**, *111* (26), 9252–9253.
(16) Nagano, S.; Poulos, T. L. Crystallographic Study on the Dioxygen Complex of Wild-Type and Mutant Cytochrome P450cam - Implications for the Dioxygen Activation Mechanism. *J. Biol. Chem.* **2005**, *280* (36), 31659–31663.
(17) Schlichting, I. The Catalytic Pathway of Cytochrome P450cam at Atomic Resolution. *Science* **2000**, *287* (5458), 1615–1622.
(18) Gerber, N. C.; Sligar, S. G. Catalytic Mechanism of Cytochrome P-450: Evidence for a Distal Charge Relay. *J. Am. Chem. Soc.* **1992**, *114* (22), 8742–8743.
(19) Tian, G.; Berry, J. A.; Klinman, J. P. Oxygen-18 Kinetic Isotope Effects in the Dopamine Beta-Monooxygenase Reaction: Evidence for a New Chemical Mechanism in Non-Heme Metallomonooxygenases. *Biochemistry* **1994**, *33* (1), 226–234.
(20) Yamaguchi, S.; Nagatomo, S.; Kitagawa, T.; Funahashi, Y.; Ozawa, T.; Jitsukawa, K.; Masuda, H. Copper Hydroperoxo Species Activated by Hydrogen-Bonding Interaction with Its Distal Oxygen. *Inorg. Chem.* **2003**, *42* (22), 6968–6970.
(21) Tsukihara, T.; Shimokata, K.; Katayama, Y.; Shimada, H.; Muramoto, K.; Aoyama, H.; Mochizuki, M.; Shinzawa-Itoh, K.; Yamashita, E.; Yao, M.; Ishimura, Y.; Yoshikawa, S. The Low-Spin Heme of Cytochrome c Oxidase as the Driving Element of the Proton-Pumping Process. *Proc. Natl. Acad. Sci.* **2003**, *100* (26), 15304–15309.
(22) Werner, A. Über Die Raumisomeren Kobaltverbindungen. *Justus Liebig's Ann. der Chemie* **1912**, *386* (1–2), 1–272.
(23) Fleischer, E. B.; Srivastava, T. S. Structure and Properties of μ-oxobis(tetraphenylporphineiron(III)). *J. Am. Chem. Soc.* **1969**, *91* (9), 2403–2405.
(24) Collman, J. P.; Reed, C. A. Syntheses of Ferrous-Porphyrin Complexes. Hypothetical Model for Deoxymyoglobin. *J. Am. Chem. Soc.* **1973**, *95* (6), 2048–2049.
(25) Collman, J. P.; Gagne, R. T.; Reed, C. A. Paramagnetic Dioxygen Complex of iron(II) Derived from a Picket Fence Porphyrin. Further Models for Hemoproteins. *J. Am. Chem. Soc.* **1974**, *96* (8), 2629–2631.
(26) Collman, J. P.; Gagne, R. R.; Reed, C. A.; Robinson, W. T.; Rodley, G. A. Structure of an iron(II) Dioxygen Complex; a Model for Oxygen Carrying Hemeproteins. *Proc. Natl. Acad. Sci. U.S.A.* **1974**, *71* (4), 1326–1329.
(27) Wuenschell, G. E.; Tetreau, C.; Lavalette, D.; Reed, C. A. H-Bonded Oxyhemoglobin Models with Substituted Picket-Fence Porphyrins - the Model-Compound Equivalent of Site-Directed Mutagenesis. *J. Am. Chem. Soc.* **1992**, *114* (9), 3346–3355.
(28) Natale, D.; Mareque-Rivas, J. C. The Combination of Transition Metal Ions and Hydrogen-Bonding Interactions. *Chem. Commun.* **2008**, No. 4, 425–437.
(29) Shook, R. L.; Borovik, A. S. The Effects of Hydrogen Bonds on Metal-Mediated O_2 Activation and Related Processes. *Chem. Commun.* **2008**, No. 46, 6095.
(30) Shook, R. L.; Borovik, A. S. Role of the Secondary Coordination Sphere in Metal-Mediated Dioxygen Activation. *Inorg. Chem.* **2010**, *49* (8), 3646–3660.
(31) Wada, A.; Harata, M.; Hasegawa, K.; Jitsukawa, K.; Masuda, H.; Mukai, M.; Kitagawa, T.; Einaga, H. Structural and Spectroscopic Characterization of a Mononuclear Hydroperoxo-Copper(II) Complex with Tripodal Pyridylamine Ligands. *Angew. Chemie Int. Ed.* **1998**, *37* (6), 798–799.
(32) Wada, A.; Honda, Y.; Yamaguchi, S.; Nagatomo, S.; Kitagawa, T.; Jitsukawa, K.; Masuda, H. Steric and Hydrogen-Bonding Effects on the Stability of Copper Complexes with

Small Molecules. *Inorg. Chem.* **2004**, *43* (18), 5725–5735.
(33) Helm, M. L.; Stewart, M. P.; Bullock, R. M.; DuBois, M. R.; DuBois, D. L. A Synthetic Nickel Electrocatalyst with a Turnover Frequency above 100,000 S^{-1} for H_2 Production. *Science* **2011**, *333* (6044), 863–866.
(34) DuBois, D. L. Development of Molecular Electrocatalysts for Energy Storage. *Inorg. Chem.* **2014**, *53* (8), 3935–3960.
(35) Dutta, A.; Roberts, J. A. S.; Shaw, W. J. Arginine-Containing Ligands Enhance H_2 Oxidation Catalyst Performance. *Angew. Chemie Int. Ed.* **2014**, *53* (25), 6487–6491.
(36) Ginovska-Pangovska, B.; Dutta, A.; Reback, M. L.; Linehan, J. C.; Shaw, W. J. Beyond the Active Site: The Impact of the Outer Coordination Sphere on Electrocatalysts for Hydrogen Production and Oxidation. *Acc. Chem. Res.* **2014**, *47* (8), 2621–2630.
(37) Reback, M. L.; Buchko, G. W.; Kier, B. L.; Ginovska-Pangovska, B.; Xiong, Y.; Lense, S.; Hou, J.; Roberts, J. A. S.; Sorensen, C. M.; Raugei, S.; Squier, T. C.; Shaw, W. J. Enzyme Design from the Bottom Up: An Active Nickel Electrocatalyst with a Structured Peptide Outer Coordination Sphere. *Chem. Eur. J.* **2014**, *20* (6), 1510–1514.
(38) Ueno, T.; Abe, S.; Yokoi, N.; Watanabe, Y. Coordination Design of Artificial Metalloproteins Utilizing Protein Vacant Space. *Coord. Chem. Rev.* **2007**, *251* (21–24), 2717–2731.
(39) Lu, Y.; Yeung, N.; Sieracki, N.; Marshall, N. M. Design of Functional Metalloproteins. *Nature* **2009**, *460* (7257), 855–862.
(40) Ward, T. R. Artificial Metalloenzymes Based on the Biotin–Avidin Technology: Enantioselective Catalysis and Beyond. *Acc. Chem. Res.* **2011**, *44* (1), 47–57.
(41) Dürrenberger, M.; Ward, T. R. Recent Achievments in the Design and Engineering of Artificial Metalloenzymes. *Curr. Opin. Chem. Biol.* **2014**, *19*, 99–106.
(42) Heinisch, T.; Ward, T. R. Design Strategies for the Creation of Artificial Metalloenzymes. *Curr. Opin. Chem. Biol.* **2010**, *14* (2), 184–199.
(43) Lewis, J. C. Artificial Metalloenzymes and Metallopeptide Catalysts for Organic Synthesis. *ACS Catal.* **2013**, *3* (12), 2954–2975.
(44) McIntosh, J. A.; Farwell, C. C.; Arnold, F. H. Expanding P450 Catalytic Reaction Space through Evolution and Engineering. *Curr. Opin. Chem. Biol.* **2014**, *19*, 126–134.
(45) Maglio, O.; Nastri, F.; Calhoun, J. R.; Lahr, S.; Wade, H.; Pavone, V.; DeGrado, W. F.; Lombardi, A. Artificial Di-Iron Proteins: Solution Characterization of Four Helix Bundles Containing Two Distinct Types of Inter-Helical Loops. *J. Biol. Inorg. Chem.* **2005**, *10* (5), 539–549.
(46) DeGrado, W. F.; Summa, C. M.; Pavone, V.; Nastri, F.; Lombardi, A. De Novo Design and Structural Characterization of Proteins and Metalloproteins. *Annu. Rev. Biochem.* **1999**, *68* (1), 779–819.
(47) Summa, C. M.; Lombardi, A.; Lewis, M.; DeGrado, W. F. Tertiary Templates for the Design of Diiron Proteins. *Curr. Opin. Struct. Biol.* **1999**, *9* (4), 500–508.
(48) Yu, F.; Cangelosi, V. M.; Zastrow, M. L.; Tegoni, M.; Plegaria, J. S.; Tebo, A. G.; Mocny, C. S.; Ruckthong, L.; Qayyum, H.; Pecoraro, V. L. Protein Design: Toward Functional Metalloenzymes. *Chem. Rev.* **2014**, *114* (7), 3495–3578.
(49) Calhoun, J. R.; Bell, C. B.; Smith, T. J.; Thamann, T. J.; DeGrado, W. F.; Solomon, E. I. Oxygen Reactivity of the Biferrous Site in the de Novo Designed Four Helix Bundle Peptide DFsc: Nature of the "Intermediate" and Reaction Mechanism. *J. Am. Chem. Soc.* **2008**, *130* (29), 9188–9189.

(50) Reig, A. J.; Pires, M. M.; Snyder, R. A.; Wu, Y.; Jo, H.; Kulp, D. W.; Butch, S. E.; Calhoun, J. R.; Szyperski, T.; Szyperski, T. G.; Solomon, E. I.; DeGrado, W. F. Alteration of the Oxygen-Dependent Reactivity of de Novo Due Ferri Proteins. *Nat. Chem.* **2012**, *4* (11), 900–906.
(51) Snyder, R. A.; Butch, S. E.; Reig, A. J.; DeGrado, W. F.; Solomon, E. I. Molecular-Level Insight into the Differential Oxidase and Oxygenase Reactivities of de Novo Due Ferri Proteins. *J. Am. Chem. Soc.* **2015**, *137* (29), 9302–9314.
(52) Snyder, R. A.; Betzu, J.; Butch, S. E.; Reig, A. J.; DeGrado, W. F.; Solomon, E. I. Systematic Perturbations of Binuclear Non-Heme Iron Sites: Structure and Dioxygen Reactivity of de Novo Due Ferri Proteins. *Biochemistry* **2015**, *54* (30), 4637–4651.
(53) Ueno, T.; Ohashi, M.; Kono, M.; Kondo, K.; Suzuki, A.; Yamane, T.; Watanabe, Y. Crystal Structures of Artificial Metalloproteins: Tight Binding of Fe(III)(Schiff-Base) by Mutation of Ala71 to Gly in Apo-Myoglobin. *Inorg. Chem.* **2004**, *43* (9), 2852–2858.
(54) Lu, Y. Metalloprotein and Metallo-DNA/RNAzyme Design: Current Approaches, Success Measures, and Future Challenges. *Inorg. Chem.* **2006**, *45* (25), 9930–9940.
(55) Lu, Y. Biosynthetic Inorganic Chemistry. *Angew. Chem., Int. Ed. Engl.* **2006**, *45* (34), 5588–5601.
(56) Berggren, G.; Adamska, A.; Lambertz, C.; Simmons, T. R.; Esselborn, J.; Atta, M.; Gambarelli, S.; Mouesca, J. M.; Reijerse, E.; Lubitz, W.; Happe, T.; Artero, V.; Fontecave, M. Biomimetic Assembly and Activation of [FeFe]-Hydrogenases. *Nature* **2013**, *498* (7456), 66–69.
(57) Cavazza, C.; Bochot, C.; Rousselot-Pailley, P.; Carpentier, P.; Cherrier, M. V; Martin, L.; Marchi-Delapierre, C.; Fontecilla-Camps, J. C.; Ménage, S. Crystallographic Snapshots of the Reaction of Aromatic C-H with O_2 Catalysed by a Protein-Bound Iron Complex. *Nat. Chem.* **2010**, *2* (12), 1069–1076.
(58) Wilson, M. E.; Whitesides, G. M. Conversion of a Protein to a Homogeneous Asymmetric Hydrogenation Catalyst by Site-Specific Modification with a diphosphinerhodium(I) Moiety. *J. Am. Chem. Soc.* **1978**, *100* (1), 306–307.
(59) Letondor, C.; Pordea, A.; Humbert, N.; Ivanova, A.; Mazurek, S.; Novic, M.; Ward, T. R. Artificial Transfer Hydrogenases Based on the Biotin−(Strept)avidin Technology: Fine Tuning the Selectivity by Saturation Mutagenesis of the Host Protein. *J. Am. Chem. Soc.* **2006**, *128* (25), 8320–8328.
(60) Shook, R. L.; Borovik, A. S. Role of the Secondary Coordination Sphere in Metal-Mediated Dioxygen Activation. *Inorg. Chem.* **2010**, *49* (8), 3646–3660.
(61) Lucas, R. L.; Zart, M. K.; Murkerjee, J.; Sorrell, T. N.; Powell, D. R.; Borovik, A. S. A Modular Approach toward Regulating the Secondary Coordination Sphere of Metal Ions: Differential Dioxygen Activation Assisted by Intramolecular Hydrogen Bonds. *J. Am. Chem. Soc.* **2006**, *128* (48), 15476–15489.
(62) Cook, S. A.; Borovik, A. S. Molecular Designs for Controlling the Local Environments around Metal Ions. *Acc. Chem. Res.* **2015**, *48* (8), 2407–2414.
(63) Shirin, Z.; Hammes, B. S.; Young, V. G.; Borovik, A. S. Hydrogen Bonding in Metal Oxo Complexes: Synthesis and Structure of a Monomeric Manganese(III)−Oxo Complex and Its Hydroxo Analogue. *J. Am. Chem. Soc.* **2000**, *122* (8), 1836–1837.
(64) Gupta, R.; Borovik, A. S. Monomeric MnIII/II and FeIII/II Complexes with Terminal Hydroxo and Oxo Ligands: Probing Reactivity via O−H Bond Dissociation Energies. *J. Am. Chem. Soc.* **2003**, *125* (43), 13234–13242.

(65) MacBeth, C. E.; Golombek, A. P.; Young Jr., V. G.; Yang, C.; Kuczera, K.; Hendrich, M. P.; Borovik, A. S. O2 Activation by Nonheme Iron Complexes: A Monomeric Fe(III)-Oxo Complex Derived from O2. *Science* **2000**, *289* (5481), 938–941.
(66) Shook, R. L.; Gunderson, W. A.; Greaves, J.; Ziller, J. W.; Hendrich, M. P.; Borovik, A. S. A Monomeric Mn^{III}–Peroxo Complex Derived Directly from Dioxygen. *J. Am. Chem. Soc.* **2008**, *130* (28), 8888–8889.
(67) Shook, R. L.; Peterson, S. M.; Greaves, J.; Moore, C.; Rheingold, A. L.; Borovik, A. S. Catalytic Reduction of Dioxygen to Water with a Monomeric Manganese Complex at Room Temperature. *J. Am. Chem. Soc.* **2011**, *133* (15), 5810–5817.
(68) Krebs, J. F.; Borovik, A. S. Metallo-Network Polymers: Reversible CO Binding to an Immobilized Copper(I) Complex. *J. Am. Chem. Soc.* **1995**, *117* (42), 10593–10594.
(69) Sharma, A. C.; Borovik, A. S. Design, Synthesis, and Characterization of Templated Metal Sites in Porous Organic Hosts: Application to Reversible Dioxygen Binding. *J. Am. Chem. Soc.* **2000**, *122* (37), 8946–8955.
(70) Welbes, L. L.; Borovik, A. S. Confinement of Metal Complexes within Porous Hosts: Development of Functional Materials for Gas Binding and Catalysis. *Acc. Chem. Res.* **2005**, *38* (10), 765–774.

CHAPTER 2

Modular Artificial Cupredoxins

Introduction

Cupredoxins are copper-containing metalloproteins that are highly optimized for electron-transfer processes. They contain mononuclear copper active sites known as Type 1 Cu centers with unusual primary coordination sphere geometries and relatively high redox potentials (180-800 mV vs. NHE).[1,2] The source of this large range in redox potentials is derived from perturbations within the primary coordination sphere throughout the family of cupredoxins. Structure-function studies have determined that "classic" Type 1 Cu sites, such as *Alcaligenes dentrificans* azurin, have distorted trigonal monopyramidal geometries with a S-atom donor from a cysteine thiolate, along with two N-atom donors from histidine residues, in the trigonal plane. The fourth, axial ligand can vary but is classically a weakly coordinating (> 2.8 Å) S-atom from a methionine residue (Fig. 2-1A).[3] Type 1 Cu proteins are also referred to as blue copper proteins, originating from the highly covalent Cu^{II}–S_{cys} bond that results in an intense S_{π}–Cu ligand-to-metal charge transfer (LMCT) band at $\lambda_{max} \sim 600$ nm ($\varepsilon_M \sim 3000\text{-}6000\ M^{-1}cm^{-1}$). The high covalency also gives rise to a small Cu hyperfine coupling of $A_z \sim 180$ MHz observable by electron paramagnetic resonance (EPR) spectroscopy.[4]

Within the family of cupredoxins, there exist "perturbed" Type 1 Cu sites where the primary coordination sphere is restructured to elicit changes in the redox potential and spectroscopic features. For instance, stellacyanin from *Rhus vernicifera* has a more strongly coordinating axial ligand, glutamine, which causes small changes in the absorption spectrum (Fig. 2-1C).[4,5] Another, more extreme example, is a variant of azurin where the native

methionine is mutated to a histidine residue. This mutation causes significant distortion away from trigonal monopyramidal and large changes in the spectroscopic features (Fig. 2-1B).[6,7] Both of these perturbed Type 1 Cu sites maintain an intense absorption band at λ_{max} ~ 600 nm, but have an additional band at λ_{max} ~ 450 nm.[4,8] These absorption features can be used to determine the relative amount of perturbation in a Type 1 Cu site. Solomon has defined the parameter $R_\varepsilon = \varepsilon_{450}/\varepsilon_{600}$ that compares the relative intensities of each absorption band as a way of quantifying the perturbation within the active site. An R_ε of ≤ 0.15 is considered a classical site, while larger values suggest perturbed sites.[2] It should be noted that while the primary coordination sphere plays an important role, there are also contributions from the secondary coordination sphere that effect electronic and structural properties of Type 1 Cu sites. Lu and coworkers have shown, via mutagenesis, that re-engineering the azurin active site with non-covalent interactions can vary the redox potential by almost 2 V.[9]

Type 1 Cu sites are of interest because of their importance in electron transfer processes and furthering our understanding of the electronic structure of Cu centers; however, it is challenging to reproduce their structural and spectroscopic features in

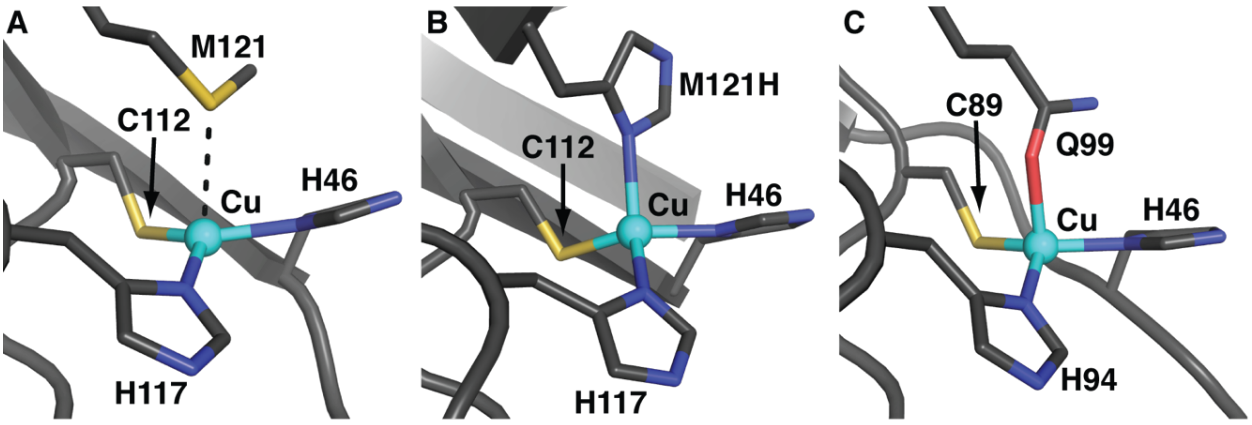

Figure 2-1. Crystal structures showing the Type 1 Cu sites in azurin (**A**, PDB: 2AZA), azurin M121H (**B**, PDB: 1A4A), and stellacyanin (**C**, PDB: 1JER).

artificial systems. There have been attempts to model these Cu active sites, including metallopeptides with sequences that contain the loop found in cupredoxins[10] and three-helix bundles[11] that assemble to form a Cu binding site. In addition, synthetic inorganic chemists have used ligand design to develop complexes modeling the active site geometry and spectroscopic features of Type 1 Cu proteins. These purely synthetic compounds, however, do not use an S-donor from cysteine and require bulky ligands to stabilize these Cu–thiolate species (Fig. 2-2).[12,13]

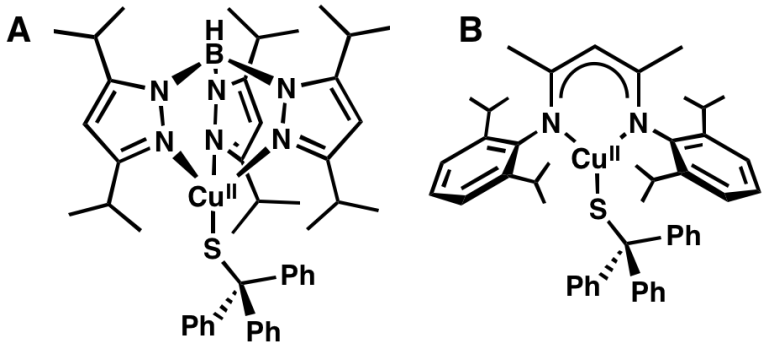

Figure 2-2. ChemDraw structures of Type 1 Cu model complexes with bulky thiolates from Kitajima[12] (**A**) and Tolman[13] (**B**).

As described in Chapter 1, biotin-streptavidin (Sav) technology has been used to develop artificial metalloenzymes for organic transformations using biotinylated second and third row transition metal complexes.[14,15] This approach has been shown to be an effective method of placing metal complexes in specific, reproducible locations within a protein owing to Sav's high affinity for biotin ($K_b \sim 10^{14}$ M^{-1}).[16] We wanted to utilize this system to build active sites that are similar to those found in native metalloproteins. Building a Type 1 Cu site within Sav provided a system to show that we can anchor a synthetic Cu complex within Sav and control the primary coordination sphere using the protein host. The work in this chapter will focus on the use of biotin-Sav technology to develop artificial metalloproteins (ArMs) that allow for modular control over the position of the metal cofactor within the

protein host and how changes in the positioning affect the primary coordination sphere around the metal center.

Design Concepts. Sav is a homotetrameric protein that assembles as a dimer of dimers, where each subunit binds one biotin molecule (Fig. 2-3). A key structural aspect of each Sav dimer is the formation of a volume of space between the biotin binding sites (referred to as the "vestibule") where the metal cofactor will sit (Fig. 2-4). Residues within the vestibule can be mutated and used as ligands to a metal center or to provide non-covalent interactions within the secondary coordination sphere (e.g. H-bonds, steric effects, electrostatic/hydrophobic). To examine how to position metal complexes within the vestibule, a series of biotinylated ligands were designed that have a variable linker length between the chelator and the biotin moieties (Fig. 2-4). The premise was that different linkers could be employed to readily change the position of the metal complexes within Sav, which in turn could be tracked by changes in spectroscopic properties.

For the studies described in the remaining chapters, three biotinylated di[2-(2-pyridyl)ethyl]amine (dpea) ligands with different linker lengths between the biotin and dpea moieties were used to prepare Cu^{II} complexes ($[Cu^{II}(biot\text{-}n\text{-}dpea)Cl_2]H_2O$; n = et, pr, or bu).

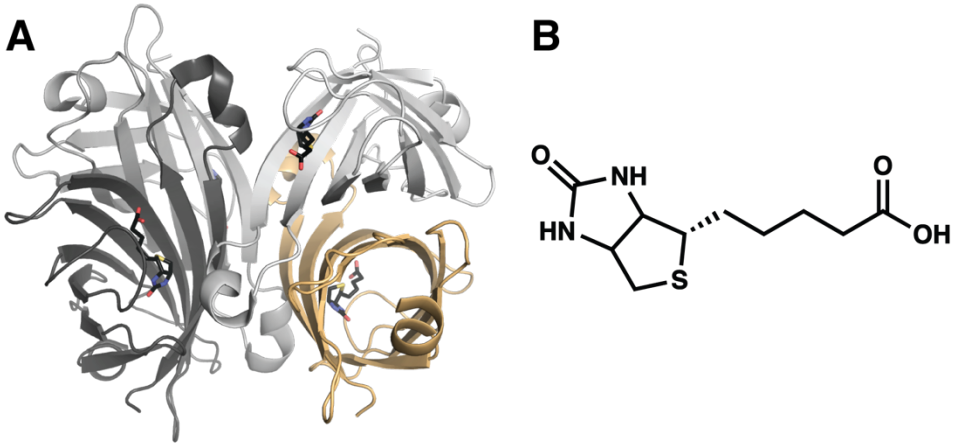

Figure 2-3. Structure of Sav illustrating the tetrameric structure (**A**) with a biotin molecule (black) bound in each subunit and a ChemDraw of biotin (**B**).

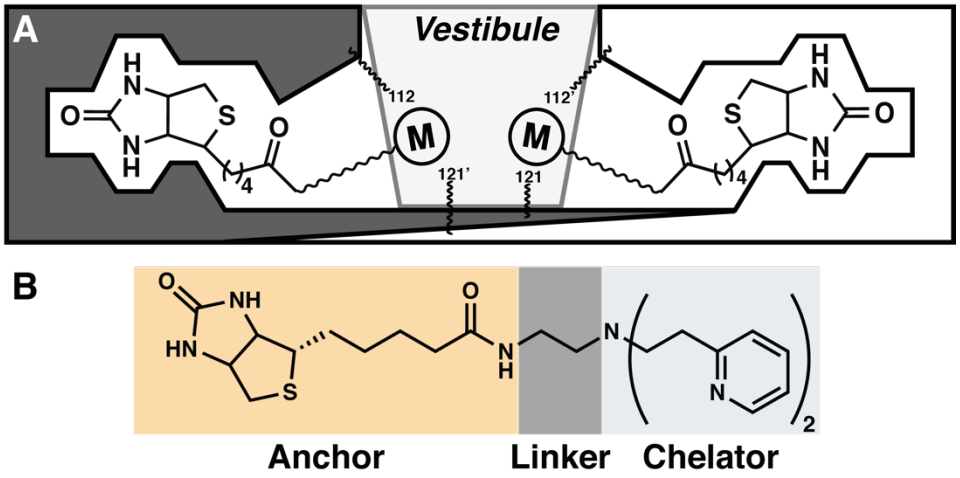

Figure 2-4. Representation of one Sav dimer showing a metal complex anchored in the vestibule with nearby amino acid residues (**A**) and a ChemDraw representation of a biotinylated ligand used in this chapter, highlighting the three important components (**B**).

The dpea ligand was chosen initially because Karlin has shown that it tightly binds Cu^{II} ions.[17]

Results and Discussion

Synthesis and Characterization of Biotinylated Compounds. The series of biot-n-dpea ligands was prepared via a 3-step route starting from dpea (Scheme 1). First, to install the linker group, dpea was alkylated with the appropriate bromo-alkyl phthalimide in the presence of potassium carbonate and potassium iodide in refluxing acetonitrile (CH_3CN). The N-phthalimide protected dpea derivative was then deprotected using excess hydrazine monohydrate to reveal the primary amine, which was reacted with biotin pentafluorophenol (biot-OPFP) to give the biotinylated ligands biot-n-dpea. These ligands were hygroscopic and stored in the desiccator. They were metallated using $CuCl_2$ in CH_3CN under an inert atmosphere and precipitated with diethyl ether to afford green solids. These complexes were analyzed by ESI-MS giving molecular ion peaks corresponding to $[Cu^{II}(\text{biot-n-dpea})Cl]^+$. Elemental analysis showed that the copper complexes were monohydrates of the form $[Cu^{II}(\text{biot-n-dpea})Cl_2]H_2O$. The perpendicular-mode EPR spectra were similar for all three complexes in 50 mM MES pH 6 and showed a signal centered around g = 2.07 consistent with

Scheme 2-1. Synthesis of Biotinylated Ligands

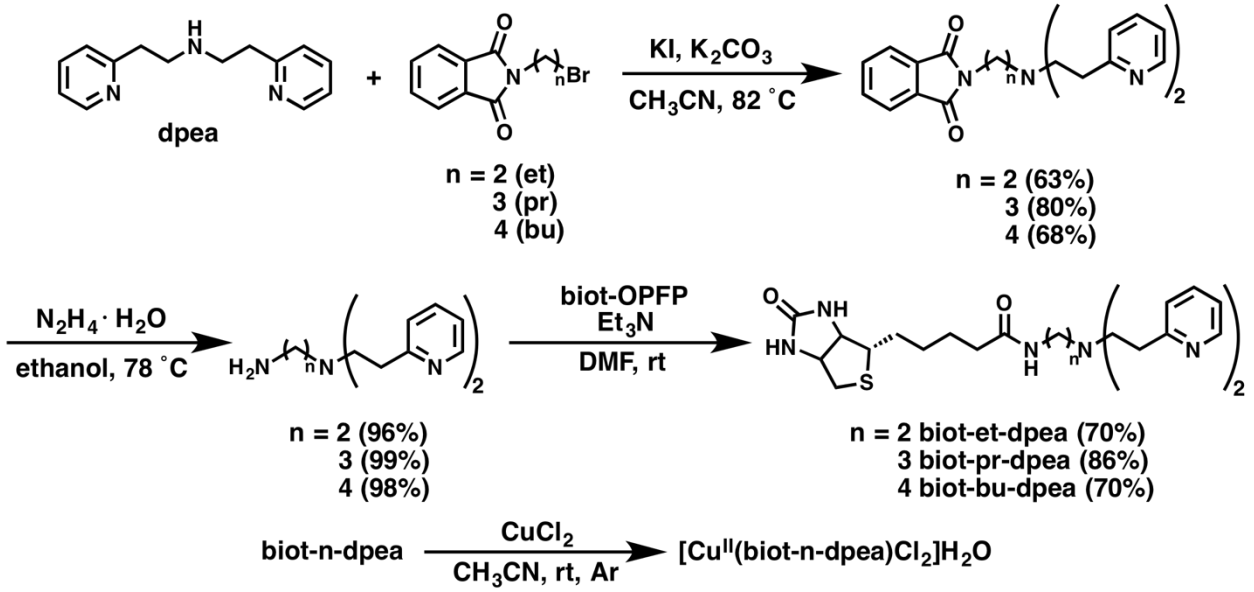

an S = ½ mononuclear copper(II) center (Fig. A-1). The absorption spectra were also similar; each with a broad absorbance band at $\lambda_{max} \sim 670$ nm (Fig. A-2).

Titration experiments were done using -(4'-hydroxyazobenzene)benzoic acid (HABA) to determine the binding stoichiometry of the $[Cu^{II}(biot\text{-}n\text{-}dpea)Cl_2]H_2O$ complexes to Sav. Because Sav can bind one biotin per subunit, it is necessary to determine the binding ratio of the complexes. For these titrations, a solution of Sav is loaded with 150 equivalents of HABA to ensure saturation of the biotin binding sites ($K_b \sim 10^4\ M^{-1}$).[18] In order to quantify complex binding to Sav, the decay of the absorbance band at $\lambda_{max} = 506$ nm corresponding to HABA⊂Sav (⊂ indicates inclusion within Sav) was monitored as a function of increasing concentration of the copper complex. After four equivalents of complex were added, no further spectroscopic changes were observed. This indicates full occupancy of the complex within Sav in the 4:1 ratio predicted by the tetrameric structure (Fig. 2-5).

Spectroscopic Characterization of ArMs with Sav WT. Initial studies were done on ArMs prepared with Sav wild-type (WT) by incubating a solution of Sav WT in 50 mM MES

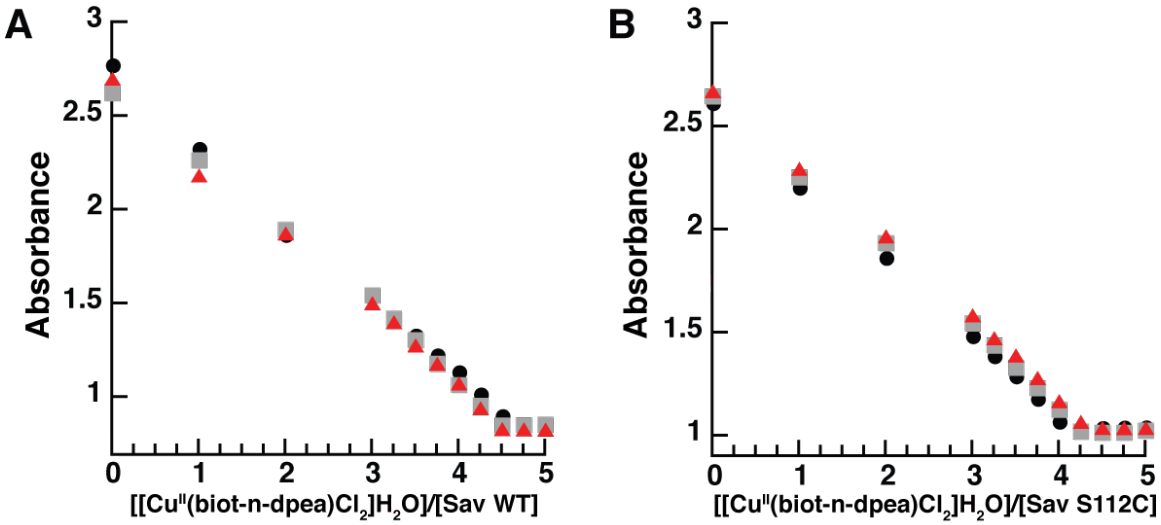

Figure 2-5. HABA titrations of **1a-c** (**A**) and **2a-c** (**B**). Black circles, et; grey squares, pr; red triangle, bu.

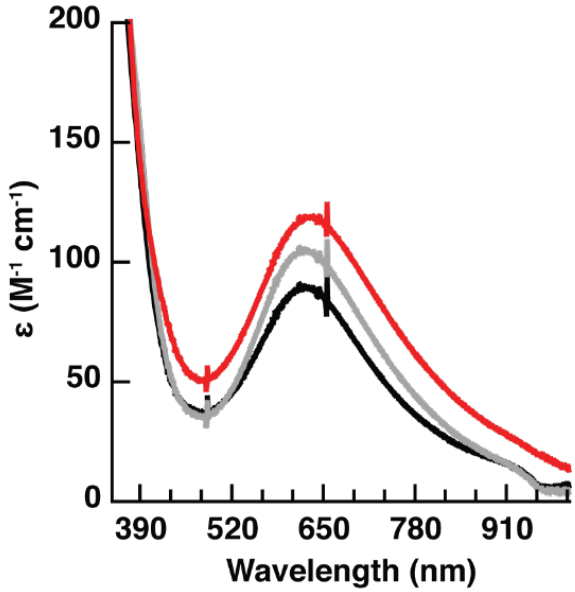

Figure 2-6. UV-vis spectra of **1a** (black), **1b** (grey), and **1c** (red).

pH 6 with a DMF solution of [Cu^{II}(biot-n-dpea)Cl$_2$]H$_2$O. The spectroscopic properties of [Cu^{II}(biot-n-dpea)(H$_2$O)$_2$]⊂Sav WT (n = et (**1a**); pr (**1b**); bu (**1c**)) support the formation of the artificial Cu proteins with λ_{max} ~ 625 nm (ε = 90-120 M^{-1} cm^{-1}) assigned to d–d transitions for the immobilized Cu^{II} centers (Fig. 2-6 and Table 2-1). The EPR spectra for **1a-c** are nearly identical and were consistent with S = ½ Cu^{II} centers (Table 2-1). Each spectrum contained

Table 2-1. Spectroscopic and Electrochemical Properties for ArMs **1a-c**

Host	WT		
n	et (**1a**)	pr (**1b**)	bu (**1c**)
λ_{max},nm (ε_M)	625 (90)	625 (100)	626 (120)
g	2.22 2.26	2.22 2.26	2.22 2.26
A, MHz	511 535	511 535	511 535
$E_{1/2}$, mV[a]	140	124[b]	167[b]

[a] vs. NHE, [b] E_a (anodic potential)

two sets of signals that we suggest are caused by the Cu^{II} complex adopting two different coordination geometries within Sav WT.

Structural Characterization of [Cu^{II}(biot-n-dpea)(H_2O)$_2$] ⊂Sav WT. Single crystals of **1a** were prepared by soaking crystals of apo-Sav WT in an aqueous solution of [Cu^{II}(biot-et-dpea)(H_2O)$_2$]$^{2+}$. Its structure was solved to 1.72 Å and showed a single Cu complex in a trigonal bipyramidal geometry within each subunit of Sav (PDB: 5K49). The primary coordination sphere consisted of three N-atom donors from the meridionally coordinated dpea ligand and two O-atom donors from aqua ligands. The trigonal plane is comprised of the apical N-atom from dpea and both aqua ligands, while the two pyridines are in the axial positions (Fig. 2-7). The average Cu–N bond length of 1.98(1) Å is similar to what has been reported in the literature (Table 2-2).[19] It is important to note that one aqua ligand (O2) is involved in a H-bonding network with a structural water molecule (O1) that is held in place by H-bonds with the carbonyl O-atom of A86 and the hydroxyl group of S112.

Active Site Re-Design: Artificial Cupredoxins. This structure showed that the cofactor sits near

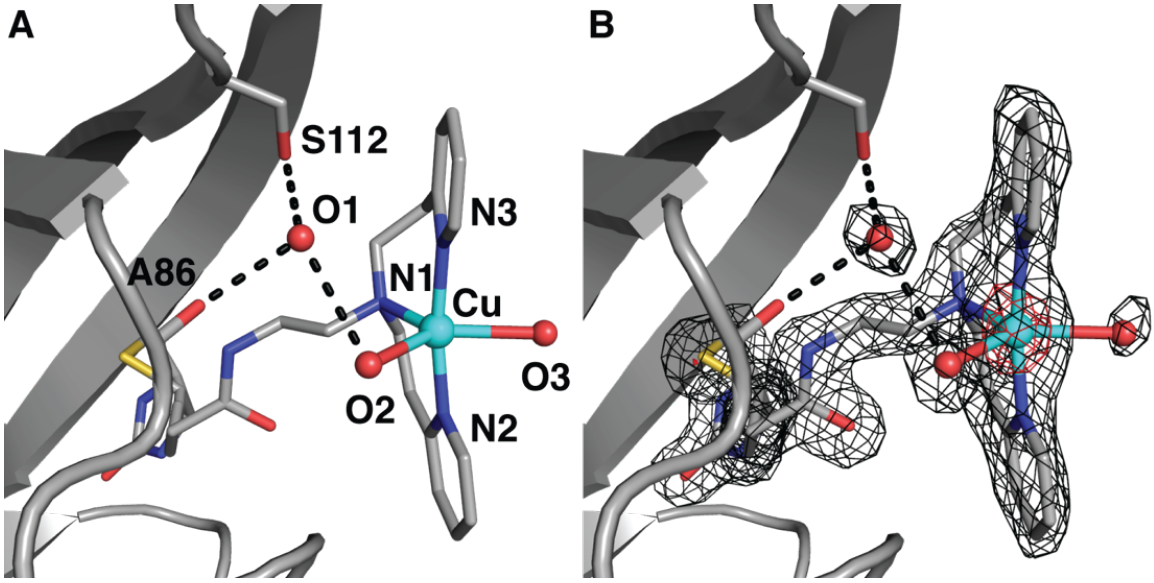

Figure 2-7. Crystal structure of **1a** (PDB: 5K49). In **B**, the cofactor and water positions are indicated by the $2F_o$-F_c electron density (black mesh, contoured at 1σ) and anomalous difference density (red mesh, contoured at 4σ). O-atoms/water molecules are in red, N-atoms are in blue, and Cu ions are in cyan.

Table 2-2. Selected Bond Lengths (Å) and Angles (°) for **1a**

Host n	WT et (**1a**)
Cu–N1	2.08(3)
Cu–N2	2.02(3)
Cu–N3	2.09(3)
Cu–O1	2.52(3)
Cu–O2	2.46(3)
N1-Cu-N2	102(3)
N1-Cu-N3	88(3)
N2-Cu-N3	170(3)
N1-Cu-O1	104(3)
N1-Cu-O2	127(3)
N2-Cu-O1	86(3)
N2-Cu-O2	84(3)
N3-Cu-O1	94(3)
N3-Cu-O2	88(3)

residue S112 which could offer a suitable site to install an endogenous ligand to bind to the Cu center. The Ward lab has shown previously that the histidine residue in Sav S112H can coordinate to a biotinylated Rh complex.[20] Instead of using Sav S112H as a host, new Cu ArMs were prepared with Sav S112C. This variant places a cysteine thiolate in close proximity to the Cu center with the hopes of designing a Cu site similar to the Type 1 Cu sites found in cupredoxins. Confining the complexes within each Sav subunit should prevent intermolecular reactions that often thwart the formation of discreet Cu^{II}–thiolate complexes in synthetic systems. For instance, reactions of free $[Cu^{II}$(biot-pr-dpea)$Cl_2]H_2O$ with a variety of thiols, including the cysteine derivative N-(*tert*-butoxycarbonyl)-L-cysteine methyl ester and triphenylmethylthiol, in DMF lead to loss of the Cu^{II} complex presumably through reduction of the Cu^{II} center and formation of a disulfide species (Scheme 2-2). Therefore, to form discreet Cu–S_{cys} species, the S112C variant of Sav was incubated with $[Cu^{II}$(biot-n-dpea)$Cl_2]H_2O$, using the same method as described for Sav WT, to produce $[Cu^{II}$(biot-n-dpea)$S_{cys112}]^+$⊂Sav S112C (n = et (**2a**); pr (**2b**); bu (**2c**)).

Scheme 2-2. General Reaction Showing Reaction of a Cu^{II} Complex with an Exogenous Thiolate

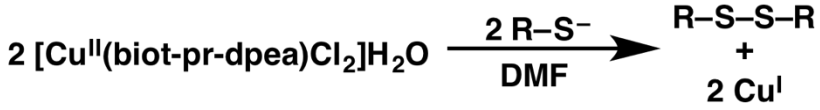

Properties of Artificial Cupredoxins. The ArM **2a** exhibited optical features significantly different than those for **1a,** with an electronic absorption spectrum showing intense bands at λ_{max} ($\varepsilon_{M,}$ M^{-1} cm^{-1}) = 445 nm (1020), 570 nm (1010), and 770 nm (700) (Fig. 2-8). Using the metric described above, these data produced an Rε = 0.95 (Table 2-3), which is similar to the value of 0.82 reported for the perturbed purple cupredoxin Nmar1307.[21] XRD studies were performed on single crystals that were refined to 1.70 Å resolution, revealing formation

of a mononuclear Cu complex with an N_3S primary coordination sphere. Unlike in **1a**, the dpea ligand adopts a facial coordination around the Cu center giving an average Cu–N bond length of 2.10(2) Å and a Cu–S1 bond length of 2.18(2) Å (Table 2-3 and Figure 2-9). The immobilized Cu complex has N1–Cu–N2, S1–Cu–N1, and S1–Cu–N2 bond angles of 92(3)˚, 129(3)˚, and 113(2)˚, respectively, that form a distorted trigonal plane with the Cu sitting 0.62 Å above the plane. Additionally, a relatively long N2–Cu–N3 bond angle of 127(3)˚ was observed. These data show that a perturbed Type 1 Cu site can be prepared in Sav S112C using the shortest linker (ethyl). However, the ethyl linker tethered the Cu center too far from the cysteine residue to allow for formation of a trigonal monopyramidal complex. Therefore, we hypothesized that using a longer linker would allow the complex flexibility to adopt a geometry more closely comparable to classic Type 1 Cu sites.

The UV-vis spectra of **2b** and **2c** showed more intense bands at $\lambda_{max} \sim 600$ nm and weaker higher energy bands at $\lambda_{max} \sim 445$ nm relative to **2a** (Fig. 2-8). This optical data gave R_ε values of 0.29 for **2b** and 0.44 for **2c**, both of which are significantly lower than **2a** and are

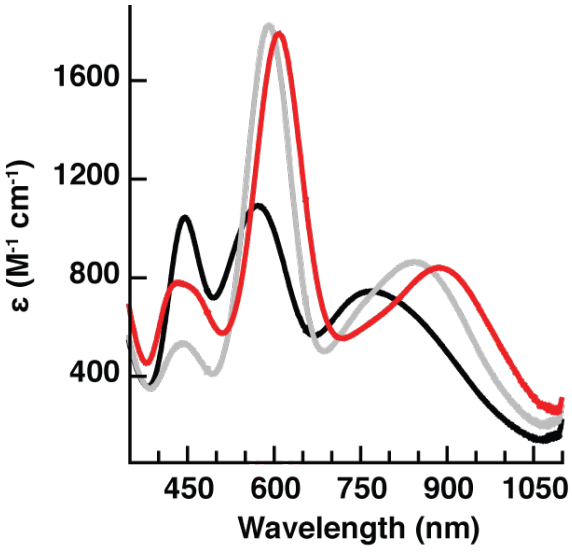

Figure 2-8. UV-vis spectra of **2a** (black), **2b** (grey), and **2c** (red).

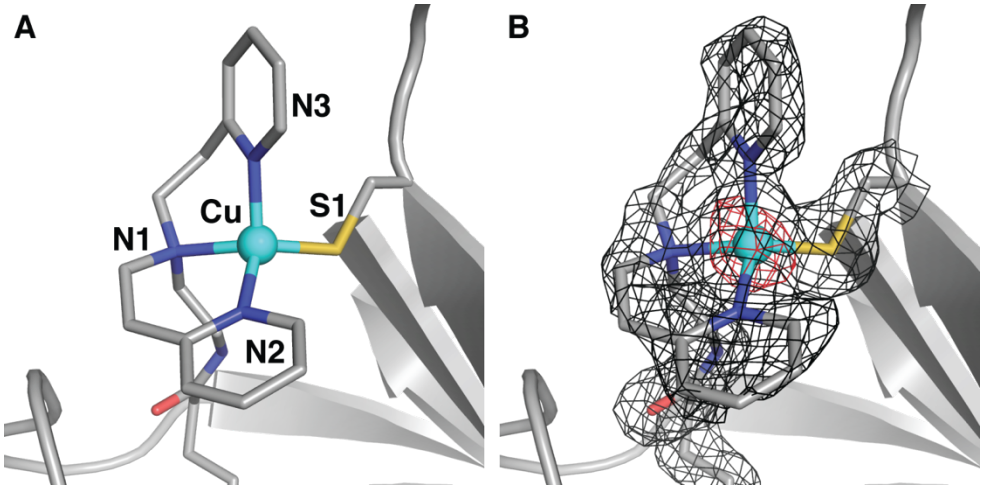

Figure 2-9. Crystal structure of **2a** (PDB: 5L3Y). In **B**, the cofactor and water positions are indicated by the $2F_o$-F_c electron density (black mesh, contoured at 1σ) and anomalous difference density (red mesh, contoured at 4σ). O-atoms/water molecules are in red, N-atoms are in blue, S-atoms are in yellow, and Cu ions are in cyan.

similar to values associated with classical Type 1 Cu sites (Table 2-3). Structural analysis of **2b** showed that the anchored Cu complex is distinct from **2a** and comparable to classical Type 1 Cu sites. The structure was solved to 1.70 Å and showed an immobilized Cu complex with an N_3S primary coordination sphere (Fig 2-10A-B). There were some important differences observed between the structure of **2b** compared to **2a**. The Cu center is placed 1.3 Å further from the biotin binding site, due to the use of a longer linker (Fig. 2-10C). This adjustment places the pyridine ring containing N2 in close proximity to L124 and places N3 closer to T114 (Fig. 2-10D). Due to this steric clashing, there is a significant contraction of the N2–Cu–N3 bond angle from 127° **2a** to 96° in **2b** (Fig. 2-10C-D). These changes result in the formation of a trigonal monopyramidal Cu complex with metrical parameters similar to classical Type 1 Cu centers. For example, the N1–Cu–N2, S1–Cu–N1, and S1–Cu–N2 bond angles of 92(3)°, 124(3)°, and 132(3)° are nearly equivalent to the analogous angles found in azurin M121H[7] and stellacyanin (Table 2-4).[24] Additionally, the Cu–S1 bond length has contracted (compared to **2a**) to 2.11(2) Å, and the Cu center is displaced only 0.41 Å from

Table 2-3. Spectroscopic and Electrochemical Properties for **2a-c** and Selected Cupredoxins

Host	S112C			Stellacyanin[a]	Azurin
n	et (**2a**)	pr (**2b**)	bu (**2c**)		$M_{121}H$[b,c]
	448 (1040)	443 (530)	437 (780)	440 (1090)	439
λ_{max},nm (ε_M)	574 (1090)	593 (1820)	611 (1790)	595 (4970)	(NR) 593
	771 (740)	846 (860)	891 (840)	781(690) 893(580)	(NR)
R_ε	0.95	0.29	0.44	0.22	1.8
g	2.02 2.07 2.19	2.05 2.06 2.18	2.06 2.08 2.19	2.02 2.08 2.29	2.05 2.05 2.25
A, MHz	nd nd 353	17 264 71	4 225 79	171 87 105	27 27 305
$E_{1/2}$ mV[d]	140	110	95	184	<200

[a]refs.[4,22,23], [b]ref.[6], [c]pH 6, [d]vs. NHE, rt, 100 mM MES pH 6

Table 2-4. Selected Bond Lengths (Å) and Angles (°) for **2a-c** and Selected Cupredoxins

Host	$S_{112}C$			Stellacyanin[b]	Azurin
n	et (**2a**)	pr (**2b**)	bu (**2c**)		M121H[c,d]
Cu–N1	2.19(2)	2.24(2)	2.28(2)	2.04(2)	2.02(1)
Cu–N2	2.03(2)	2.05(2)	2.10(2)	1.96(2)	2.06(1)
Cu–N3	2.09(2)	2.20(2)	2.12(2)	–	2.24(1)
Cu–S	2.18(2)	2.11(2)	2.09(2)	2.18(2)	2.25(1)
d[Cu-$(N/S)_t$][a]	0.62	0.41	0.66	0.32	0.58
N1-Cu-N2	92(3)	92(3)	89(3)	101(3)	98(3)
N1-Cu-S	129(3)	124(3)	124(3)	118(3)	109(3)
N2-Cu-S	113(3)	132(3)	118(3)	134(3)	130(3)
N1-Cu-N3	97(3)	94(3)	87(3)	–	126(3)
N2-Cu-N3	127(3)	96(3)	105(3)	–	89(3)
N3-Cu-S	100(3)	110(3)	124(3)	–	106(3)

[a]Distance of Cu from trigonal plane, [b]ref.[24], [c]ref.[7], [d]pH 6

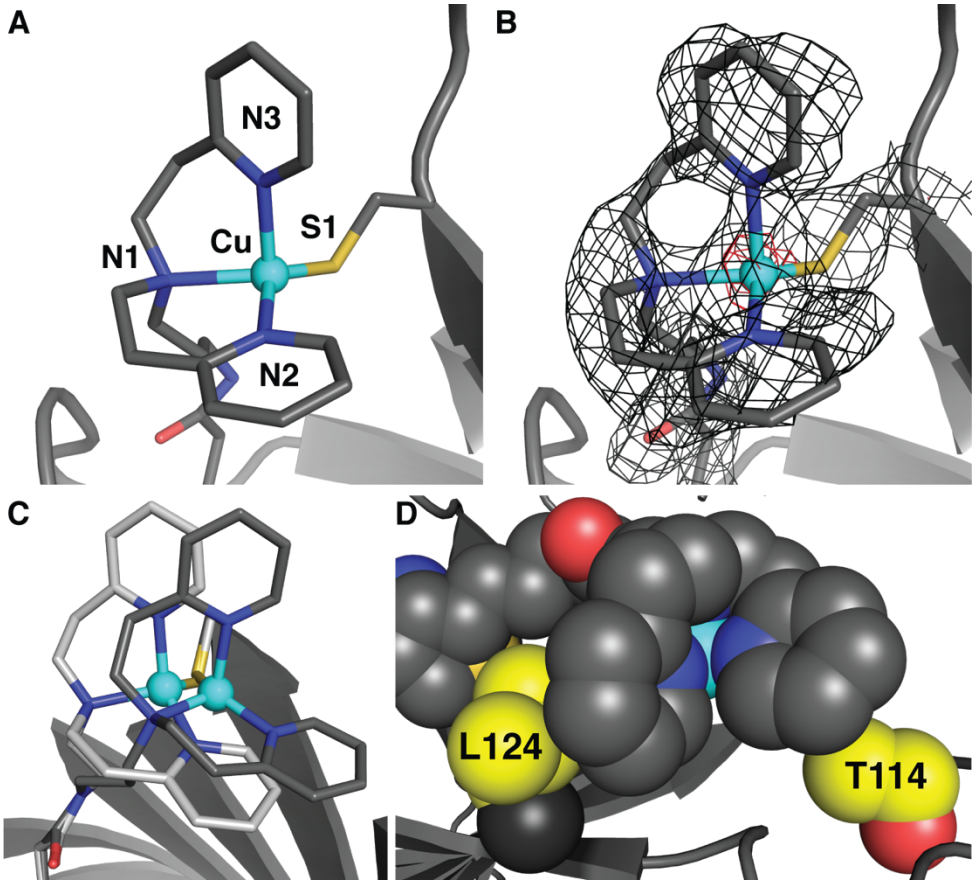

Figure 2-10. The crystal structure of **2b** (**A,B,D**; PDB: 5K67) with cofactor position indicated by the $2F_o$-F_c electron density (black mesh, contoured at 1σ) and anomalous difference density (red mesh, contoured at 4σ) (**B**), structural overlay of **2a** (white) and **2b** (grey) (**C**), and space filling representation illustrating the steric interaction with residues (yellow) (**D**). O-atoms/water molecules are in red, N-atoms are in blue, S-atoms are in yellow and Cu ions are in cyan.

the trigonal plane, which is also closer to the values found for Type 1 Cu sites.

The molecular structure of **2c** was solved to 1.40 Å resolution. The structure of the Cu complex is similar, although not identical, to **2b** and the Cu center is moved 0.82 Å further from the biotin binding site (Fig. 2-11). Now, the trigonal plane is composed of N2, N3, and S1 and N1 is bound in the axial position with the Cu distorted out of the trigonal plane by 0.66 Å. It has N1–Cu–N2, S1–Cu–N1, and S1–Cu–N2 bond angles of 89(3)˚, 124(3)˚, and 118(3)˚ and a Cu–S1 bond length of 2.09(2) Å (Table 2-4). The pyridines have similar steric interactions with L124 and T114 as was seen in **2b** causing a small N2–Cu–N3 bond angle of 89(3)˚.

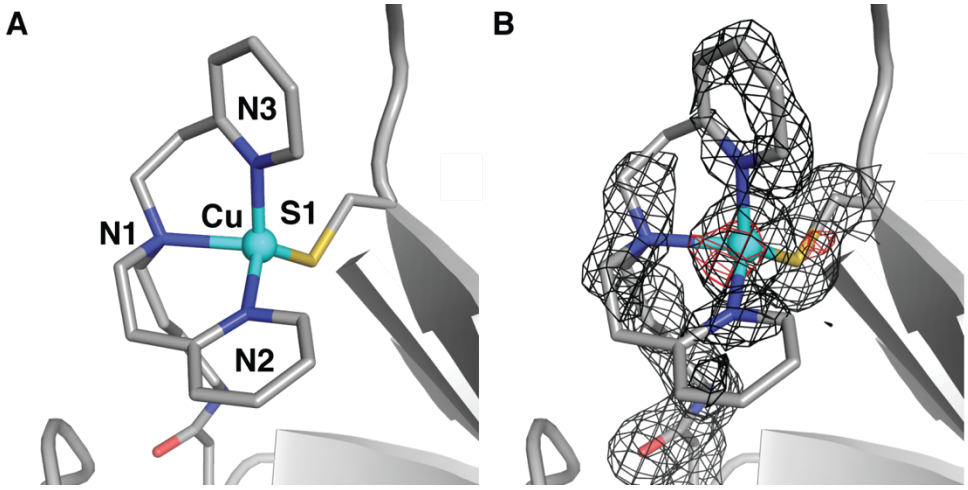

Figure 2-11. Crystal structure of **2c** (**A**, PDB: 5K68) with cofactor indicated by the $2F_o$-F_c electron density (black mesh, contoured at 1σ) and anomalous difference density (red mesh, contoured at 4σ) (**B**). O-atoms/water molecules are in red, N-atoms are in blue, and Cu ions are in cyan.

EPR Properties. The ArMs prepared with Sav S112C exhibited significant differences by S- and X-band EPR spectroscopy when compared to ArMs prepared with Sav WT. In collaboration with the Hendrich lab at Carnegie Mellon University, EPR spectra at two different microwave frequencies were used to determine the hyperfine coupling constants (A) due to the absence of well-defined patterns by X-band EPR.[25] The EPR spectra for **1a** showed an average A_z of 523 MHz (similar values were found for **1b** and **1c**), while the A_z for **2a** was significantly reduced to 353 MHz (Fig. 2-12 and Table 2-3). This reduction in A_z is consistent with a strong covalent Cu–S_{cys} interaction as the unpaired electron is delocalized onto the thiolate ligand. The EPR spectra for **2b** and **2c** were significantly different than that of **2a** (Fig. 2-12). Generally, Cu^{II} complexes have large hyperfine splitting for $A_z = A_{||}$ which are associated with $g_z = g_{||}$. However, for **2b** and **2c** the g_z values are 2.18 and 2.19 and have small A_z values (71 and 79 MHz, respectively). In fact, the largest hyperfine splitting values were found in the perpendicular direction. **2b** and **2c** had A_y values of 264 and 225 MHz and A_x values close to zero (Table 2-3). These data indicated a rhombic A-tensor that differs greatly from axial symmetry. This combination of low A_z values and rhombic A-tensors for

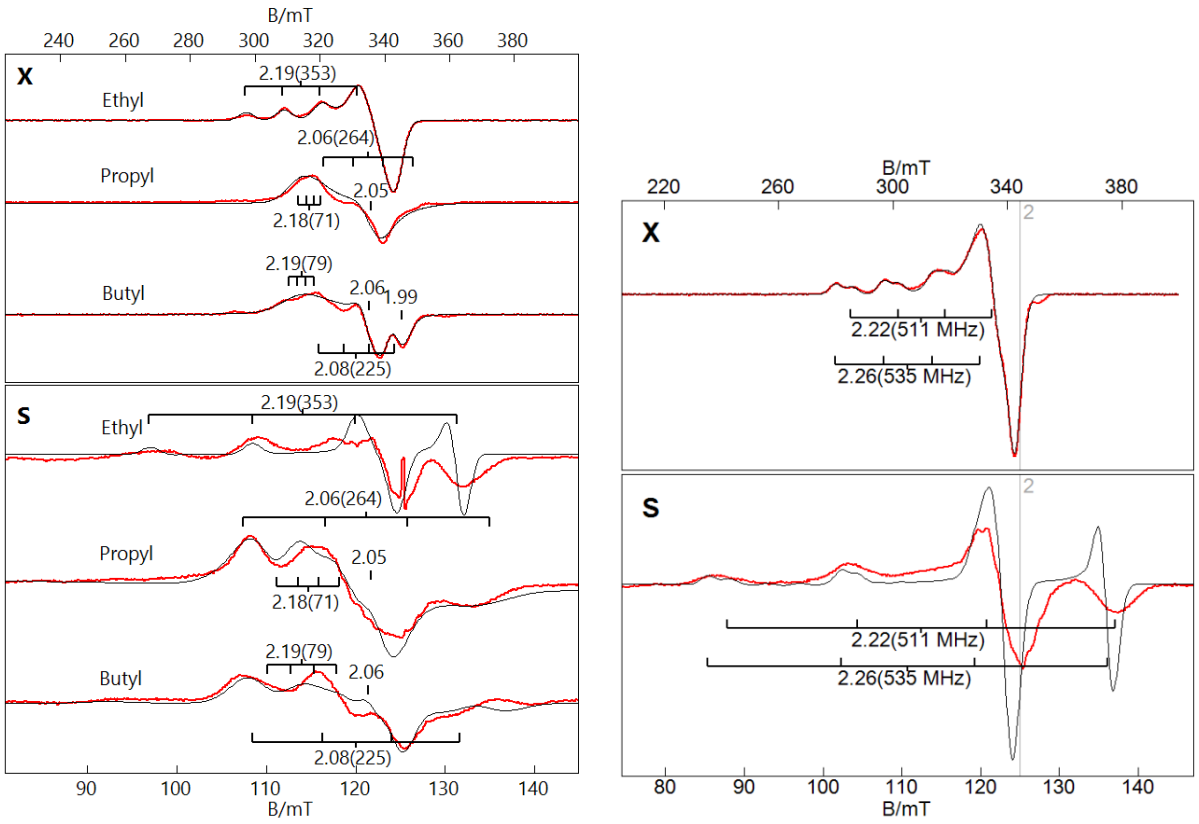

Figure 2-12. X- and S-band EPR spectra for ArMs **2a-c** (left) and **1a** (right). The EPR spectra for **1a** are representative of ArMs **1b-c**. Simulations are shown in black` and A-values are reported in MHz.

2b and **2c** is rare and is linked directly to the primary coordination sphere induced by the protein host. The small A_z values are indicative of large covalency in the Cu–S bond, reinforcing the short Cu–S_{cys} bond lengths seen in the XRD studies.[26] These findings are similar to those reported for stellacyanin[22] and azurin M121H (Table 2-3).[6]

Redox Properties. To probe the redox properties of the Cu ArMs, cyclic voltammetry (CV) experiments were performed. **1a** was found to undergo a reversible one-electron process assigned to the Cu^{II}/Cu^{I} couple at 70 mV vs. NHE that is shifted to 140 mV in **2a** (Fig. 2-13). This positive shift with the Sav S112C variant was expected for a thiolate-ligated Cu center and the potential approaches reported values for Type 1 Cu proteins.[6,23] The CVs of **1b-c** and

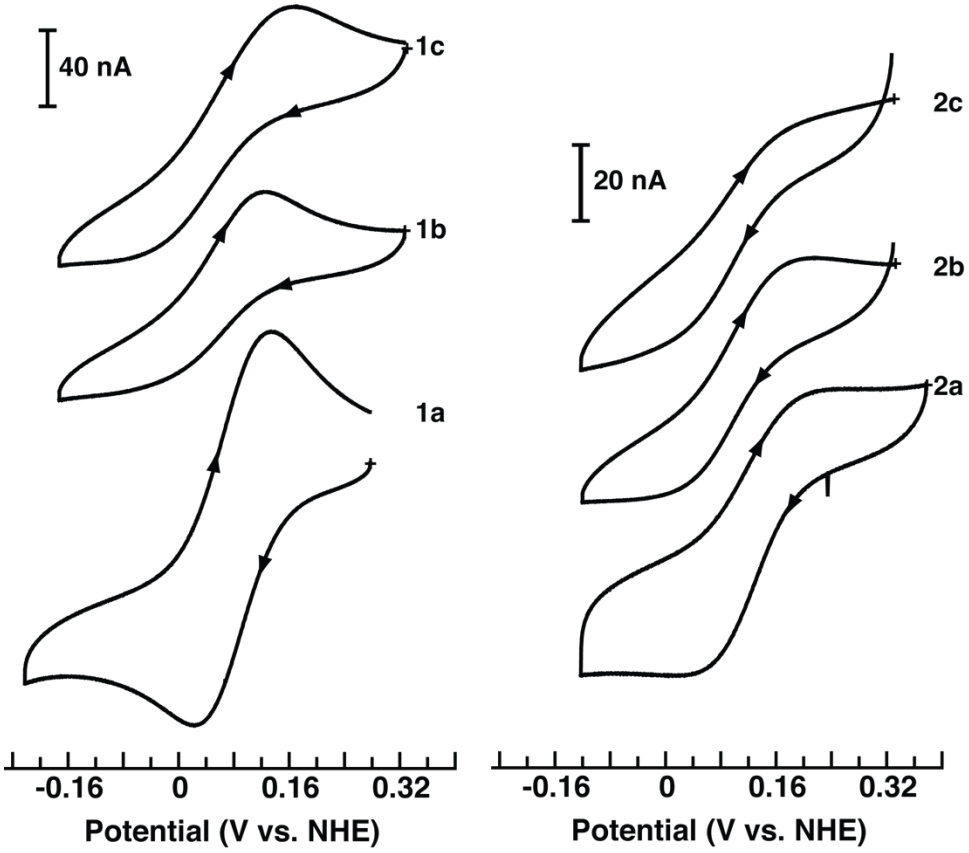

Figure 2-13. CVs of ArMs **1a-c** and **2a-c** collected at 5 mV/s in 100 mM MES pH 6.

2b-c are less reversible than **1a** and **2a** but display similar trends: a ~70 mV increase was measured for **2b** versus **1b** and ~35 mV for **2c** versus **1c** (Table 2-3).

Summary and Conclusions

The Cu ArMs discussed in this chapter helped elucidate key design features for using Sav to house synthetic metal complexes. The structure of **1a** showed that the immobilized Cu complexes resides near S112 that could be used as a site to install an endogenous ligand. This premise was realized using the variant Sav S112C in which the serine at position 112 was replaced with a cysteine. Therefore, using the S112C variant of Sav produced ArMs **2a-c**, which had considerably different spectroscopic and structural properties than **1a-c**, but similar properties to cupredoxins. Spectroscopic and structural studies confirmed that these

differences were caused by a structural change in the primary coordination spheres of the Cu complexes caused by the coordination of an endogenous thiolate ligand from a cysteine. In addition, this worked demonstrated the advantage of using ligands of variable linker length to control the placement of the Cu center within Sav. These modular linker lengths coupled with two-pointing binding in Sav S112C (through biotin and the cysteine residue) afforded us control of the placement and geometry of the immobilized Cu center to produce excellent artificial models for the Type I Cu sites found in cupredoxins. The properties of **2a-c** illustrate the efficacy of this approach to model active sites of metalloproteins and prepare Cu complexes that are generally not stable in synthetic systems. Finally, the molecular structure of **1a** illustrated that H-bonds are prevalent within the Sav vestibule that can interact with ligands bound to the Cu center. This provides an opportunity to utilize the existing H-bonding network to assist in binding and stabilizing other exogenous ligands, which will be the subject of the remaining two chapters.

Experimental Details

General Methods. All commercially available reagents were obtained of the highest purity and used as received. Dimethylsulfoxide, *N,N*-dimethylformamide, and diethy lether were degassed with argon and dried by vacuum filtration through activated alumina according to the procedure by Grubbs.[27] Triethylamine and ethylenediamine were distilled from KOH. Thin-layer chromatography (TLC) was performed on Whatman 250 μm layer 6 Å glass-backed silica gel plates. Eluted plates were visualized using UV light. Silica gel chromatography was performed with the indicated solvent system using Fisher reagent silica gel 60 (230-400 mesh). Biotin pentafluorophenol ester[28] and di[2-(2-pyridyl)ethyl]amine (dpea)[29] were prepared according to literature procedures.

Preparative Methods

2-(2-(bis(2-(pyridin-2-yl)ethyl)amino)ethyl)isoindoline-1,3-dione (phthalimide-et). This compound was prepared following a modified literature procedure.[30] Dpea (1.01 g, 4.44 mmol), bromoethylphthalimide (1.24 g, 4.88 mmol), KI (0.147 g, 0.890 mmol), and K_2CO_3 (2.45 g, 17.7 mmol) were mixed in 40 mL CH_3CN and refluxed for 24 hours. The solution was cooled to room temperature, filtered and the solvent was removed under vacuum. The red-brown residue was dissolved in dichloromethane and washed with 3 x 25 mL aqueous $NaHCO_3$ and 1 x 25 mL H_2O. The red-brown oil was dissolved in 15 mL conc. HCl and washed with 2 x 20 mL dichloromethane. The aqueous layer was carefully neutralized with solid $NaHCO_3$ and extracted in 3 x 20 mL dichloromethane. The solvent was dried over $MgSO_4$ and removed under vacuum to yield crude product. The crude product was purified via column chromatography with silica gel (methanol:acetone (1:4)) to yield **phthalimide-et** as a pure yellow oil (1.11 g, 63%). ^{1}H NMR (600 MHz, DMSO-d_6) δ 8.45 (d, J = 4.2 Hz, 2H), 7.82 (q, J = 3.7 Hz, 2H), 7.71 (q, J = 3.6 Hz, 2H), 7.45 (td, J = 9.2, 1.9 Hz, 2H), 7.08 (d, J = 8.5 Hz, 2H), 7.02 (t, J = 7.0 Hz, 2H), 3.75 (t, J = 8.0 Hz, 1H), 2.98 (t, J = 9.8 Hz, 4H), 2.86 (t, J = 9.7 Hz, 6H); ^{13}C NMR (125 MHz, DMSO-d_6) δ 168.3, 160.5, 149.2, 136.1, 133.8, 132.3, 123.4, 123.2, 121.0, 77.4, 77.1, 53.9, 53.5, 51.2, 36.2, 36.1; HRMS (ESI, MeOH) *m / z* calcd for $C_{24}H_{24}N_4O_2$ $[M + H]^+$ 401.2, found 401.1; ATR-IR (neat, cm^{-1}, selected bands): 3060, 3005, 2947, 2810, 1771, 1701, 1590, 1568, 1473, 1434, 1395, 1355, 1322, 1184, 1102, 1085, 992, 749, 718, 625.

2-(3-(bis(2-(pyridin-2-yl)ethyl)amino)propyl)isoindoline-1,3-dione (phthalimide-pr) was prepared following the same procedure as described above for **phthalimide-et** and isolated analogously as a yellow oil in 80% yield (1.22 g). ^{1}H NMR (500 MHz, DMSO-d_6)

δ 8.49 (d, J = 5.1 Hz, 2H), 7.84 (q, J = 3.6 Hz, 2H), 7.71 (q, J = 3.7 Hz, 2H), 7.56 (td, J = 9.2, 1.6 Hz, 2H), 7.15 (d, J = 9.2 Hz, 2H), 7.09 (t, J = 6.8 Hz, 2H), 3.66 (t, J = 8.6 Hz, 2H), 2.99 (br s, 8H), 2.71 (br s, 2H), 1.89 (br s, 2H); ^{13}C NMR (125 MHz, DMSO-d_6) δ 168.4, 149.3, 136.4, 134.0, 133.9, 132.2, 123.6, 123.3, 121.3, 53.7, 51.6, 36.3, 35.6, 26.3; HRMS (ESI, MeOH) *m/z* calcd for $C_{25}H_{26}N_4O_2$ $[M + H]^+$ 415.2134, found 415.2132; ATR-IR (neat, cm^{-1}, selected bands): 2941, 2810, 1769, 1705, 1589, 1568, 1473, 1434, 1394, 1365, 1188, 1148, 1122, 1088, 1038, 992, 889, 746, 719, 603.

2-(4-(bis(2-(pyridin-2-yl)ethyl)amino)butyl)isoindoline-1,3-dione (phthalimide-bu) was prepared with the analogous procedure as **phthalimide-et** to yield **phthalimide-bu** as a yellow oil (0.99 g, 68%). ^{1}H NMR (600 MHz, DMSO-d_6) δ 8.48 (d, J = 3.6 Hz, 2H), 7.84 (q, J = 3.0 Hz, 2H), 7.71 (q, J = 3.0 Hz, 2H), 7.56 (t, J = 7.8 Hz, 2H), 7.13 (br, 2H), 7.09 (t, J = 5.4 Hz, 2H), 3.65 (t, J = 6.6 Hz, 2H), 2.97 (br s, 8H), 2.63 (br s, 2H), 1.61 (br s, 3H), 1.51 (br s, 2H); ^{13}C NMR (125 MHz, DMSO-d_6) δ 168.5, 160.1, 149.2, 136.4, 134.0, 132.2, 123.6, 123.3, 121.3, 53.8, 53.3, 37.8, 35.3, 26.4, 24.1; HRMS (ESI, MeOH) *m/z* calcd for $C_{26}H_{28}N_4O_2$ $[M + H]^+$ 429.23, found 429.19.

N,N-bis(2-(pyridin-2-yl)ethyl)ethane-1,2-diamine (amine-et). This compound was prepared following a modified literature procedure.[30] Hydrazine monohydrate (0.795 mL, 16.3 mmol) and **phthalimide-et** (1.40 g, 3.27 mmol) were dissolved in 30 mL of absolute ethanol and the solution was refluxed for 3 hours. The phthalhydrazide precipitated as a white solid and was removed via filtration. The ethanol was removed under vacuum and the residue was dissolved in $CHCl_3$ and washed with 2 x 10 mL 1 M NaOH to remove any remaining phthalhydrazide. The organic layer was dried over $MgSO_4$, volatiles were removed under reduced pressure, and the product was isolated as a brown oil (0.957 g,

98%). ^{1}H NMR (500 MHz, $CDCl_3$) δ 8.53 (d, J = 4.2 Hz, 2H), 7.54 (td, J = 7.8, 1.6 Hz, 2H), 7.10 (app. t, J= 5.3 Hz, 2H), 7.05 (app. d, J = 7.8 Hz, 2H), 2.92 (m, 8H), 2.64 (t, J = 5.0 Hz, 2H), 2.58 (t, J = 5.0 Hz, 2H); ^{13}C NMR (125 MHz, $CDCl_3$) δ 160.9, 149.4, 136.2, 123.6, 121.2, 56.8, 54.2, 39.8, 36.3; HRMS (ESI, MeOH) *m/z* calcd for $C_{16}H_{22}N_4$ $[M + H]^+$ 271.1923, found 271.1445; ATR-IR (neat ,cm^{-1}, selected bands): 3358, 3273, 2957, 2821, 1596, 1568, 1476, 1435, 1360, 1306, 1149, 1114, 1079, 1074, 999, 758, 632.

N,N-bis(2-(pyridin-2-yl)ethyl)propane-1,3-diamine (amine-pr) was prepared analogously to the above procedure for **amine-et** to yield **amine-pr** as a yellow oil (0.989 g, 99%). ^{1}H NMR (600 MHz, $CDCl_3$) δ 8.52 (d, J = 4.2 Hz, 2H), 7.56 (td, J = 7.8, 1.2 Hz, 2H), 7.10 (m, 4H), 2.92 (s, 8H), 2.61 (q, J = 6.6 Hz, 4H), 1.56 (quin, J = 7.2 Hz, 2H); ^{13}C NMR (125 MHz, $CDCl_3$) δ 160.7, 149.3, 136.3, 123.5, 121.2, 54.1, 51.8, 40.4, 35.9, 30.1; HRMS (ESI, MeOH) *m/z* calcd for $C_{17}H_{24}N_4$ $[M + H]^+$ 285.2001, found 285.1690; ATR-IR (neat, cm-1, selected bands): 3356, 2935, 2812, 1642, 1591, 1568, 1475, 1434, 1355, 1309, 1150, 1120, 1089, 1052, 993, 751, 631, 606.

N,N-bis(2-(pyridin-2-yl)ethyl)butane-1,4-diamine (amine-bu) was prepared following an analogous procedure for **amine-et** to afford **amine-bu** as a yellow oil in (0.935 g,98% yield). ^{1}H NMR (500 MHz, $CDCl_3$) δ 8.52 (d, J = 4.1 Hz, 2H), 7.56 (t, J = 8.6 Hz, 2H), 7.11 (t, J = 7.8 Hz, 4H), 2.93 (s, 8H), 2.65 (t, J = 6.8 Hz, 2H), 2.56 (t, J = 7.3 Hz, 2H), 2.36 (br, 2H), 1.46 (quin, J = 6.8 Hz, 2H), 1.37 (quin, J = 6.9 Hz, 2H); ^{13}C NMR (125 MHz, $CDCl_3$) δ 160.8, 149.3, 136.3, 1123.5, 121.2, 54.1, 53.9, 42.1, 36.1, 31.5, 24.8; HRMS (ESI, MeOH) *m/z* calcd for $C_{18}H_{26}N_4$ $[M + Na]^+$ 321.2055, found 321.2048.

biot-et-dpea. A solution of biotin-pentafluorophenol ester (1.24 g, 3.03 mmol), **amine-et** (0.860 g, 3.18 mmol), and triethylamine (1.11 mL, 7.95 mmol) in 40 mL DMF was allowed

to stir overnight at room temperature. The DMF was removed under vacuum and the sticky tan residue was washed with diethy lether until a free-flowing white solid formed. The white solid was filtered, washed with diethyl ether, and dried under vacuum to yield white solid (1.05 g, 70%). The solid was stored in a desiccator. ^{1}H NMR (600 MHz, DMSO-d_6) δ 8.45 (d, J = 3.6 Hz, 2H), 7.65 (t, J = 7.2 Hz, 2H), 7.51 (t, J = 4.8 Hz, 1H), 7.18 (t, J = 7.8 Hz, 4H), 6.42 (s, 1H), 6.35 (s, 1H), 4.29 (t, J = 6.0 Hz, 1H), 4.11 (t, J = 5.4 Hz, 1H), 3.07 (m, 3H), 2.56 (m, 3H), 2.20 (t, J = 7.8 Hz, 2H), 1.60 (m, 1H), 1.47 (m, 4H), 1.29 (m, 2H); ^{13}C NMR (125 MHz, DMSO-d_6) δ 171.8, 162.7, 160.3, 148.9, 136.3, 123.2, 121.2, 61.0, 59.2, 55.4, 53.7, 52.4, 36.8, 35.3, 28.3, 28.1, 25.3; HRMS (ESI, MeOH) *m/z* calcd for $C_{26}H_{36}N_6O_2S$ $[M + Na]^+$ 519.2518, found 519.2504. ATR-IR (cm^{-1}, selected bands): 3223, 3072, 2928, 2856, 2817, 2359, 1698, 1641, 1591, 1567, 1548, 1473, 1433, 1324, 1264, 1148, 1121, 1051, 993, 861, 749, 596.

biot-pr-dpea was prepared analogously to the above procedure for **biot-et-dpea** and isolated as a tan solid (1.25 g, 86%) that was stored in a desiccator. ^{1}H NMR (600 MHz, DMSO-d_6) δ 8.46 (d, J = 4.8 Hz, 2H), 7.71 (t, J = 5.4 Hz, 2H), 7.66 (td, J = 7.8, 1.8 Hz, 2H), 7.22 (d, J = 7.8 Hz, 2H), 7.18 (t, J = 5.4 Hz, 2H), 6.41 (s, 1H), 6.35 (s, 1H), 4.29 (t, J = 6.0 Hz, 1H), 4.11 (t, J = 6.0 Hz, 1H), 3.08 (quin, J = 3.0 Hz, 1H), 2.98 (q, J = 6.0 Hz, 2H), 2.84 (s, 8H), 2.80 (m, 1H), 2.57 (d, J = 12.6 Hz, 1H), 2.04 (t, J = 7.8 Hz, 2H), 1.60 (m, 1H), 1.47 (m, 4H), 1.31 (m, 7H); ^{13}C NMR (125 MHz, DMSO-d_6) δ 171.8, 162.7, 160.3, 148.9, 136.3, 123.2, 121.2, 61.0, 59.2, 55.4, 53.4, 50.6, 36.6, 35.3, 34.9, 28.3, 28.1, 26.7, 25.4; HRMS (ESI, MeOH) *m/z* calcd for $C_{27}H_{38}N_6O_2S$ $[M + Na]^+$ 533.2675, found 533.2673.

biot-bu-dpea was prepared analogously to the above procedure for **biot-et-dpea** and the tan solid (1.12 g, 70%) was stored in a desiccator. ^{1}H NMR (600 MHz, DMSO-d_6) δ 8.46 (d, J

= 4.7 Hz, 2H), 7.71 (br t, 2H), 7.66 (t, J = 7.7 Hz, 2H), 7.22 (d, J = 7.7 Hz, 2H), 7.18 (t, J = 5.1 Hz, 2H), 6.41 (s, 1H), 6.34 (s, 1H), 4.29 (t, J = 6.2 Hz, 1H), 4.11 (t, J = 3.9 Hz, 1H), 3.08 (q, J = 6.4 Hz, 1H), 2.98 (q, J = 5.9 Hz, 2H), 2.83 (br s, 8H), 2.80 (m, 1H), 2.57 (d, J = 12.5 Hz, 1H), 2.04 (t, J = 7.4 Hz, 2H), 1.60 (m, 1H), 1.47 (m, 4H), 1.32 (m, 6H); ^{13}C NMR (125 MHz, DMSO-d_6) δ 171.8, 162.7, 160.2, 148.9, 136.3, 123.2, 121.1, 61.0, 59.2, 55.5, 53.3, 52.7, 38.2, 35.3, 34.9, 28.3, 28.1, 27.0, 25.4; HRMS (ESI, MeOH) *m/z* calcd for $C_{28}H_{40}N_6O_2S$ $[M + Na]^+$ 547.2831, found 547.2824.

Preparation of Metal Complexes

$[Cu^{II}$(biot-et-dpea)$Cl_2]H_2O$ was prepared by addition of solid $CuCl_2$ (0.026 g, 0.193 mmol) to a solution of biot-et-dpea (0.094 g, 0.189 mmol) in 10 mL acetonitrile. The green solution was allowed to stir for 4 h before concentrating the solution to ~ 1 mL and precipitating the complex with diethyl ether. The green solid was collected via filtration, which was then washed with diethyl ether, and dried under vacuum (0.097 g, 82%). ATR-IR (solid,cm^{-1}, selected bands): 3256, 3076, 2927, 1694, 1651, 1540, 1435, 1362, 1328, 1260, 1150, 1112, 1062, 1024, 761; HRMS (ESI, MeOH) *m/z* calcd for $C_{26}H_{36}Cl_2CuN_6O_2S$ $[M-Cl]^+$ 594.1611, found 594.1615. Elem. Anal. Calcd for ($C_{27}H_{40}Cl_2CuN_6O_3S$): C: 48.9; H, 6.08; N, 12.67. Found: C, 48.85; H, 6.06: N, 12.36.

$[Cu^{II}$(biot-pr-dpea)$Cl_2]H_2O$ was prepared following the same procedure as for Cu^{II}(biot-et-dpea)$Cl_2]$ H_2O and isolated as a green solid in 69% yield (0.085 g). ATR-IR (solid, cm^{-1}, selected bands): 3257, 3076, 2927, 1695, 1651, 1543, 1435, 1362, 1330, 1260, 1150, 1114, 1062, 1024, 760; HRMS (ESI, MeOH) *m/z* calcd for $C_{27}H_{38}Cl_2CuN_6O_2S$ $[M-Cl]^+$ 608.1761, found 607.1746. Elem. Anal. Calcd for ($C_{27}H_{40}Cl_2CuN_6O_3S$): C, 48.90; H, 6.08; N, 12.67. Found: C, 48.78; H, 6.04; N, 12.49.

[Cu^{II}(biot-bu-dpea)Cl_2] H_2O was prepared following the same procedure as for Cu^{II}(biot-et-dpea)Cl_2] H_2O and isolated as a green solid in 81% yield (0.090 g). ATR-IR (solid, cm^{-1}, selected bands): 3252, 3075, 2927, 1696, 1651, 1540, 1435, 1360, 1330, 1260, 1153, 1112, 1062, 1024, 760; HRMS (ESI, MeOH) *m/z* calcd for $C_{28}H_{40}Cl_2CuN_6O_2S$ $[M]^+$ 622.1918, found 622.1918. Elem. Anal. Calcd for ($C_{28}H_{42}Cl_2CuN_6O_3S$): C, 49.66; H, 6.25; N, 12.41. Found: C, 49.49; H, 6.49: N, 12.01.

Physical Methods

Instrumentation. Fourier Transform infrared spectra were collected on a Varian 800 Scimitar Series FTIR spectrometer. ^1H, ^{13}C, and ^{19}F NMR spectra were recorded at 500/600, 125, and 500 MHz, respectively. ^1H NMR spectra were reported in ppm on the δ scale and referenced to tetramethylsilane or solvent residual. The data are presented as follows: chemical shift, multiplicity (s = singlet, d = doublet, t = triplet, q = quartet, quin = quintet, m = multiplet, br = broad), coupling constant(s) in Hertz (Hz), and integration. ^{13}C NMR spectra were reported in ppm relative to $CDCl_3$ (77.23 ppm) or DMSO-d_6 (39.52 ppm). Mass spectra were measured on a MicroMass AutoSpec E, a MicroMass Analytical 7070E, or a MicroMass LCT Electrospray instrument. Electronic absorbance spectra were recorded with a Cary 50 or 8453 Agilent UV-vis spectrophotometer. X-band (9.64 GHz) and S-band (3.50 GHz) EPR spectra were recorded on a Bruker spectrometer equipped with Oxford liquid helium cryostats. The quantification of all signals is relative to a CuEDTA spin standard. The concentration of the standard was derived from an atomic absorption standard (Aldrich). For all instruments, the microwave frequency was calibrated with a frequency counter and the magnetic field with a NMR gaussmeter. A modulation frequency of 100 kHz was used for all EPR spectra. The EPR simulation software (*SpinCount*) was

used.[31] Cyclic voltammetry was performed on a Pine WaveDriver 10 potentiostat and the data was analyzed using AfterMath.

Electronic Absorption Studies. A solution of 150 μM Sav was prepared in 50 mM MES pH 6 and transferred to a low-volume 1 cm cuvette. 18 μL of a 10 mM solution of $[Cu^{II}$(biot-n-dpea)$Cl_2]H_2O$ in DMF was added and allowed to equilibrate for 5 minutes.

HABA Titrations. A 15 μM solution of Sav was prepared in 200 mM phosphate buffer (PB) at pH 7 and transferred to a 1 cm cuvette. 248 μL (150 equivalents) of a 20 mM solution of HABA in PB was added to ensure saturation of Sav. A solution of $[Cu^{II}$(biot-n-dpea)$Cl_2]H_2O$ in DMF was added in 2-8 μL portions until 5 equivalents had been added. The titration was monitored by UV-vis at λ_{max} = 506 nm.

EPR Experiments. To 250 μL of a 250 μM solution of Sav in 50 mM MES pH 6 was added 25 μL of a 10 mM solution of $[Cu^{II}$(biot-n-dpea)$Cl_2]H_2O$ in DMF. The solution was allowed to equilibrate for 5 minutes before being transferred to an EPR tube and flash-frozen in liquid nitrogen.

Electrochemical Measurements. The reduction potential of each ArM was determined by cyclic voltammetry using a Pine WaveDriver 10 potentiostat equipped with a Faraday cage. A solution containing 300 μL of 500 μM Sav in 100 mM MES pH 6 and 60 μL of 10 mM $[Cu^{II}$(biot-n-dpea)$Cl_2]H_2O$ in DMF was allowed to equilibrate for 5 minutes before data collection. Each metalloprotein was sampled between 2.5 and 50 mV/s. The reduction potentials were measured against a Ag/AgCl reference electrode using glassy carbon working and counter electrodes and converted to NHE.

Crystallization of $[Cu^{II}$(biot-et-dpea)$(OH_2)_2]^{2+}$⊂WT Sav. Apo-Sav protein crystals were obtained at 20°C within two days by hanging-drop vapor diffusion technique mixing 2.5 μL

crystallization buffer (2.6 M ammonium sulfate, 0.1 M sodium acetate, pH 4.0) and 7.5 µL protein solution (26 mg/mL lyophilized protein in water). The droplet was equilibrated against a reservoir solution of 500 µL crystallization buffer. Subsequently, single crystals of Sav were soaked for 1 day at 20 °C in a soaking buffer, which was prepared by mixing 1 µL of a 10 mM stock solution of complex $[Cu^{II}(biot\text{-}n\text{-}dpea)Cl_2]H_2O$ (in water with 100 mM $CuCl_2$), 9 µL crystallization buffer, and 0.5 µL of the original protein solution. After the soaking, crystals were transferred for 30 seconds into a cryo-protectant solution consisting of 30 % (v/v) glycerol in crystallization buffer. Next, crystals were shock-frozen in liquid nitrogen.

Crystallization of $[Cu^{II}(biot\text{-}n\text{-}dpea)(S_{Cys})]^+ \subset$ *S112C Sav.* Apo-Sav protein crystals were obtained at 20°C within two days by sitting-drop vapor diffusion technique mixing 1.5 µL crystallization buffer plus TCEP (2.0 M ammonium sulfate, 0.1 M sodium acetate, pH 4.0, 2 mM TCEP) and 3.5 µL protein solution (26 mg/mL lyophilized protein in water). The droplet was equilibrated against a reservoir solution of 100 µL crystallization buffer. Subsequently, single crystals of SAV were soaked for 1 day at 20 °C in a soaking buffer, which was prepared by mixing 1 µL of a 10 mM stock solution of $[Cu^{II}(biot\text{-}n\text{-}dpea)Cl_2]H_2O$ in water, 9 µL crystallization buffer, and 0.5 µL of the original protein solution. After soaking, crystals were transferred for 30 seconds into a cryo-protectant solution consisting of 30 % (v/v) glycerol in crystallization buffer. Next, crystals were shock-frozen in liquid nitrogen.

Data Processing. X-ray diffraction data were collected at the Swiss Light Source beam line X06DA and Advanced Light Source (BL8.2.1) at a wavelength of 1 Å and processed with software XDS[32] (**1a**) or iMOSFLM[33] (**2a-c**) and scaled with AIMLESS (CCP4 Suite).[33] The

structure was solved by molecular replacement using program PHASER (CCP4 Suite)[33] and the structure 2QCB from the PDB as input model with ligand and water molecules removed. For structure refinement REFMAC5 (CCP4 Suite)[34] and PHENIX.REFINE[35] were used. Ligand manipulation was carried out with program REEL using the small molecule crystal structures KAHGAB[36] (for **1a**) and CIFKOR[37] (for **2a-c**) from the Cambridge Structural Database as input models. For water picking, electron density, and structure visualization, the software COOT[38] was used. Figures were drawn with PyMOL (the PyMOL Molecular Graphics System, Version 1.5.0.5, Schrödinger, LLC). Crystallographic details, processing and refinement statistics are given in Tables 2-5 and 2-6.

Structural Results.

Crystal Color. All crystals of Sav soaked with complexes $[Cu^{II}(biot\text{-}n\text{-}dpea)Cl_2]H_2O$ changed from colorless to pale blue (**1a**), violet (**2a**), or dark blue (**2b-c**).

Structural Refinement.

Overall Structures. Apo-crystals of proteins WT Sav and S112C Sav soaked with Cu-complexes $[Cu^{II}(biot\text{-}n\text{-}dpea)Cl_2]H_2O$ constituted space group $I4_122$ with virtually identical unit cell parameters (Table 2-5). A single Sav monomer was obtained per asymmetric unit after molecular replacement. Protein residues 2-11 and 135-159 of the N- and C-terminus, respectively, were not resolved in the electron density, presumably due to disorder. Starting from the Sav monomer, the biological homotetramer is generated by application of crystallographic C2-symmetry axes along the x-, y- and z-axes of the unit cell. The overall protein structures are virtually identical to structure biotin⊂WT Sav (PDB 1STP, see Table 2-5).

General Complex Modeling. For all structures of apo-protein crystals soaked with the corresponding Cu complexes the following general observations were made: i) residual electron density in the F_o-F_c map was observed in the biotin binding pocket, ii) in the Sav vestibule which is formed by protein residues of loop-3,4^{A} (the superscript number indicates Sav monomer within tetramer) loop-4,5^{C}, loop-5,6^{A} loop-7,8^{A} and loop-7,8^{B}, and iii) an anomalous dispersion density map indicated a significant peak in the Sav vestibule superimposed with the electron density peak (Figs. 2-7B, 2-9B, 2-10B, and 2-11B). The residual electron density was fit with the corresponding Cu complexes which projected Cu to the position of the strong anomalous density peak.

Structure Refinement of 1a. The complex $[Cu^{II}(\text{biot-et-dpea}(OH_2)_2]^{2+}$ was modeled with 100% occupancy. The coordinating nitrogen atoms of the dpea ligand together with the Cu center were modeled within one plane (Fig. 2-7, Table 2-2). Additional electron density above and below this plane was observed that suggested modeling of two coordinating water molecules, resulting in a trigonal bipyramidal complex geometry around the Cu center. One of the two pyridine rings (containing N3, N3 hereafter) of dpea is nestled within loop-7,8^{A} residues S112^{A}, T114^{A}, K121^{A} , L124^{A} and two water molecules (w12 and w52) that form an H-bonding network. The second pyridine of dpea (containing N2, N2 hereafter) is in close proximity to loop-3,4^{A} and loop-7,8^{B} residues side chains N49^{A} and K121^{B}, and a glycerol molecule. One of the coordinated water molecules O3 is located close to carbonyl A83^{C} within loop-5,3^{C}. The Cu⋯Cu distance between two symmetry-related complexes is 11.3 Å (Fig. 2-14).

Structure Refinement of 2a. The $[Cu^{II}(\text{biot-et-dpea}(S_{Cys})]^{+}$ complex was modeled with 100% occupancy. Side chain S112C in Sav S112C is isosteric to the serine side chain and adopts the

same rotamer as in the corresponding Sav WT structure. However, in stark contrast to WT Sav, the dpea moiety of the complex is rotated in the linker position by about 120° around the C12–N3 bond (Figure 2-9, Table 2-4). This projects both pyridines N2 and N3 to loop-7,8^{A} and loop-7,8^{B}. N2 is tilted out of the plane and a bond is formed between Cu and S112C-Sγ (2.2 Å) to yield a pseudo-tetrahedral geometry at the Cu center (Figure 2-9). The Cu···Cu distance between the two Sav monomers is 12.1 Å (Fig. 2-15). A relatively high residual R_{free} value and a significantly elevated overall B-factor of this structure suggest increased flexibility (Table 2-6).

Structure Refinement of 2b. The [Cu^{II}(biot-pr-dpea(S_{Cys})]$^{+}$ complex was modeled with 100% occupancy. The Cu(DPEA) conformation is very similar to that of **2a** (Figure 2-10, Table 2-4). However, the longer propyl linker projects the Cu(DPEA) moiety away from the biotin anchor and decreases the Cu–Sγ_{112C} distance to 2.11Å (Figure 2-10). The N2–Cu–N3 angle is sharper compared to the corresponding structure of **2a** (96° vs. 127°, respectively) (Figure 2-10). The Cu···Cu distance between the two Sav monomers is 10.3 Å (Fig. 2-16). High flexibility of the DPEA moiety is reflected by increased atomic B-factors (Table 2-6).

Structure Refinement of 2c. The [Cu^{II}(biot-bu-dpea(S_{Cys})]$^{+}$ complex was modeled with 80 % occupancy. The Cu(DPEA) conformation is very similar to those of **2a-b** (Figure 2-11, Table 2-4). The longer butyl linker places the Cu center farther from the biotin anchor, although the Cu–Sγ_{112C} distance is similar to **2b** (2.09 Å). Additionally, the longer spacer causes movement of the S112C residue leading to a sharper $C_{\beta(S112C)}$–$S_{\gamma(S112C)}$–Cu angle of 103° vs. 110° for **2a-b**. The Cu···Cu distance between the two Sav monomers is 10.5 Å (Fig. 2-17). High flexibility of the dpea moiety is reflected by increased atomic B-factors and decreased

occupancy is attributed to steric clashing between the Cu complexes in adjacent Sav subunits (Table 2-6).

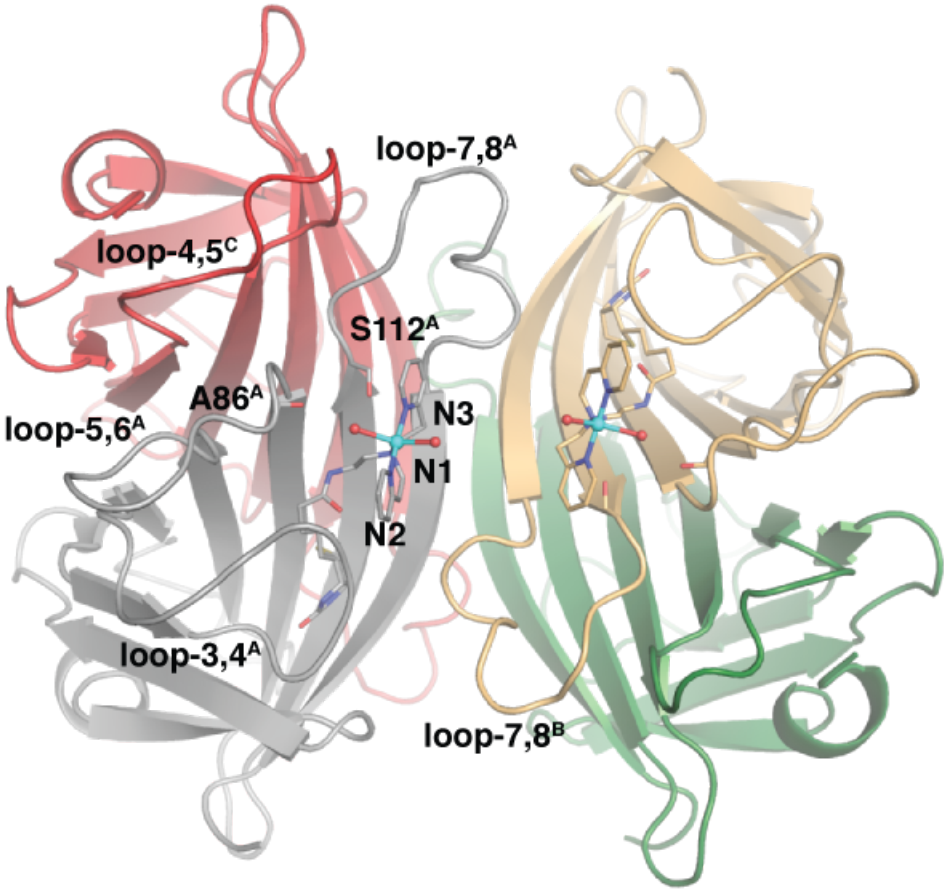

Figure 2-14. Tetrameric view of **1a** shown as a cartoon. Subunit A is in grey, subunit B is in tan, subunit C is in red, and subunit D is in green.

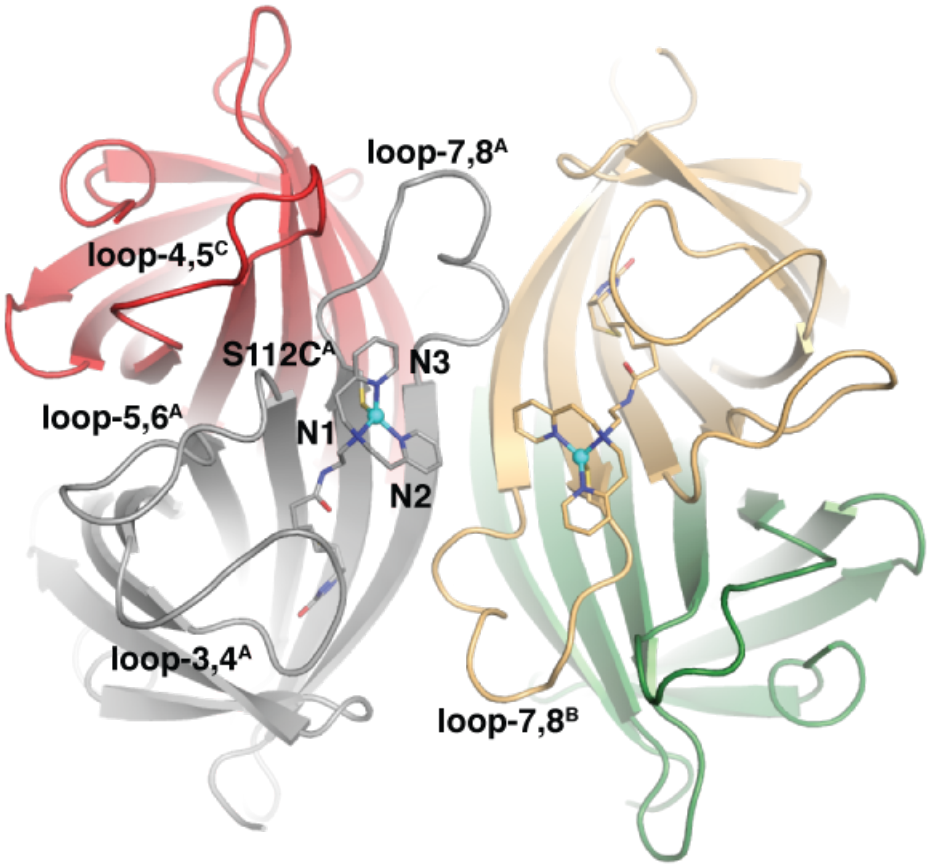

Figure 2-15. Tetrameric view of **2a** shown as a cartoon. Subunit A is in grey, subunit B is in tan, subunit C is in red, and subunit D is in green.

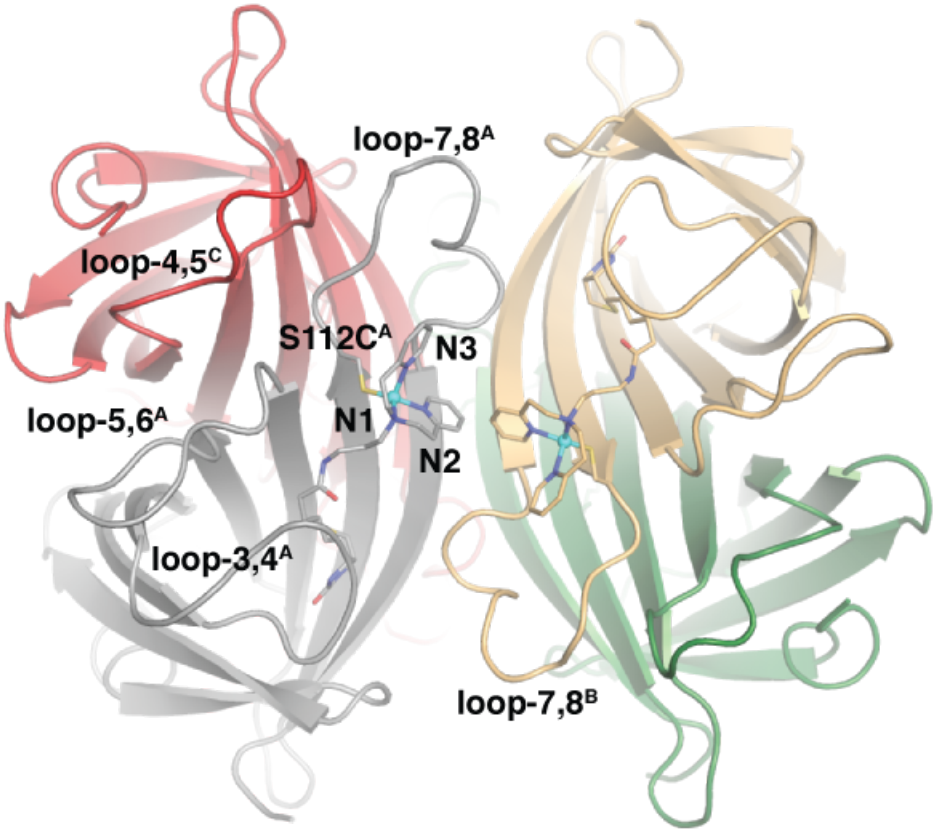

Figure 2-16. Tetrameric view of **2b** shown as a cartoon. Subunit A is in grey, subunit B is in tan, subunit C is in red, and subunit D is in green.

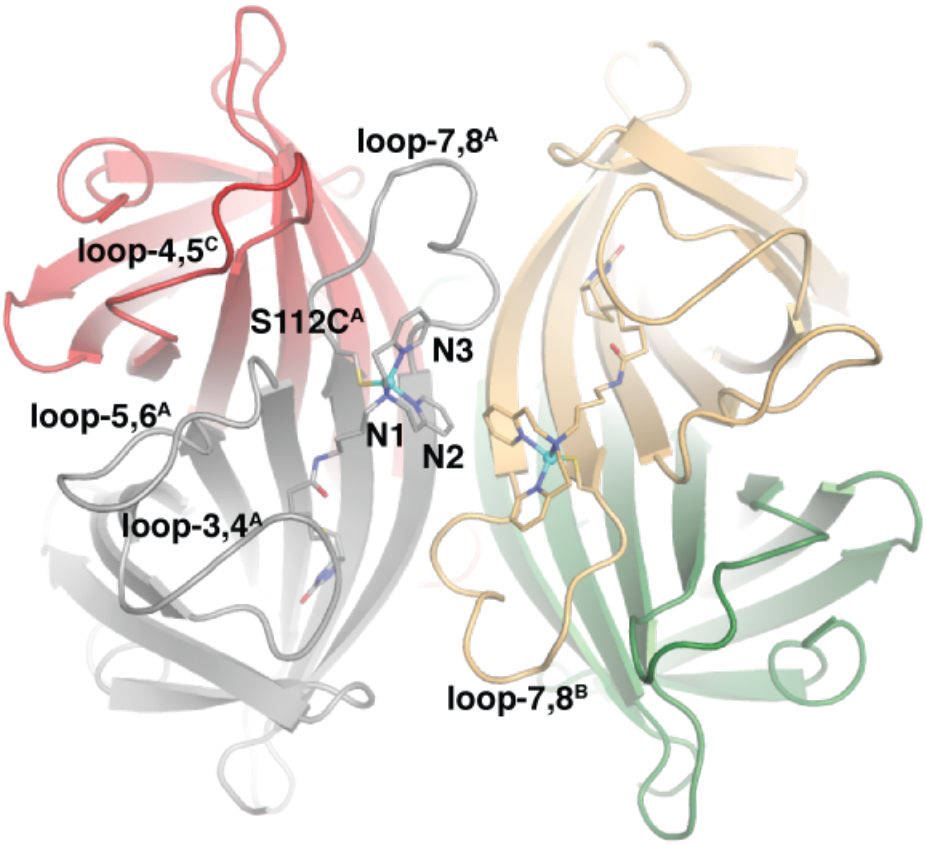

Figure 2-17. Tetrameric view of **2c** shown as a cartoon. Subunit A is in grey, subunit B is in tan, subunit C is in red, and subunit D is in green.

Table 2-5. X-ray Crystallographic Data Processing and Refinement Statistics

Sav Mutant	Wild type	S112C	S112C	S112C
Cu complex	$[Cu^{II}(biot\text{-}et\text{-}dpea)(OH_2)_2]^{2+}$ (**1a**)	$[Cu^{II}(biot\text{-}et\text{-}dpea)(S_{Cys})]^{2+}$ (**2a**)	$[Cu^{II}(biot\text{-}pr\text{-}dpea)(S_{Cys})]^{2+}$ (**2b**)	$[Cu^{II}(biot\text{-}bu\text{-}dpea)(S_{Cys})]^{2+}$ (**2c**)
PDB code	5K49	5L3Y	5K67	5K68
Cu complex PDB 3-letter code	SM6	CU6	SI4	SI9
Data Processing				
Unit Cell	a, b, c = 57.6 Å, 57.6 Å, 183.7 Å; α, β, γ = 90°	a, b, c = 57.8 Å, 57.8 Å, 183.3 Å; α, β, γ = 90°	a, b, c = 57.7 Å, 57.7 Å, 183.6 Å; α, β, γ = 90°	a, b, c = 57.7 Å, 57.7 Å, 183.6 Å; α, β, γ = 90°
Space group	$I4_122$	$I4_122$	$I4_122$	$I4_122$
Resolution (Å)	54.9 – 1.72	55.1 – 1.70	45.9 – 1.70	45.9 – 1.40
Highest resolution shell (Å)	1.75 - 1.72	1.73 – 1.70	1.73 – 1.70	1.42 – 1.40
R_{merge} (%)	10.8 (88.5)	11.1 (178.0)	9.2 (199.7)	6.9 (144.6)
No. of unique reflections	16931 (873)	17574 (885)	11863 (571)	31080 (1486)
Multiplicity	7.9 (7.6)	6.1 (6.5)	5.1 (4.3)	6.8 (6.6)
I/sig(I)	12.0 (1.9)	7.6 (0.9)	9.7 (0.7)	12.7 (1.0)
Completeness	99.7 (98.9)	99.8 (100)	66.9 (64.3)	99.8 (98.8)
CC(1/2)	1.00 (0.68)	1.00 (0.57)	1.00 (0.34)	1.00 (0.40)
Structure Refinement				
R_{work}	0.13	0.18	0.20	0.14
R_{free}	0.17	0.24	0.23	0.18
Rmsd bond length (Å)	0.0294	0.032	0.0192	0.0317
Rmsd bond angle (°)	2.5839	2.7865	2.1818	3.915
Rmsd compared to biotin-SAV WT (PDB 1STP) (Å)	0.78	0.71	0.70	0.76
No ligands Cu complex Water Glycerol acetate	 1 67 1 1	 1 45 - -	 1 32 1 -	 1 68 - -

Table 2-6. Summary of Structural Details

PDB code	5K49	5L3Y	5K67	5K68
ArM	**1a**	**2a**	**2b**	**2c**
Electron density at Cu in FoFc omit map (σ)	15	21	12	16
Anomalous dispersion density at Cu (σ)	12	11	5	7
Geometry of Cu complex	Trigonal bipyramidal	distorted tetrahedral	Trigonal monopyramidal	Trigonal monopyramidal
Coordination number of Cu complex	5	4	4	4
Conformation of Cu complex	parallel to loop 7,8	orthogonal to loop 7,8	orthogonal to loop 7,8	orthogonal to loop 7,8
Occupancy of Cu complex (%)	100	100	100	80
B-factor (Å^2) Overall protein S112X Loop-7,8 Cu complex DPEA Cu	 20 15 20 30 45 41	 26 22 25 35 51 40	 23 21 23 40 71 59	 20 16 19 39 63 44
Distance Cu···Cu (Å)	11	12	10	10

References

(1) Liu, J.; Chakraborty, S.; Hosseinzadeh, P.; Yu, Y.; Tian, S.; Petrik, I.; Bhagi, A.; Lu, Y. Metalloproteins Containing Cytochrome, Iron–Sulfur, or Copper Redox Centers. *Chem. Rev.* **2014**, *114* (8), 4366–4469.

(2) Solomon, E. I.; Hadt, R. G. Recent Advances in Understanding Blue Copper Proteins. *Coord. Chem. Rev.* **2011**, *255*, 774–789.

(3) Baker, E. N. Structure of Azurin from Alcaligenes Denitrificans Refinement at 1· 8 Å Resolution and Comparison of the Two Crystallographically Independent Molecules. *J. Mol. Biol.* **1988**, *203* (4), 1071–1095.

(4) LaCroix, L. B.; Randall, D. W.; Nersissian, A. M.; Hoitink, C. W. G.; Canters, G. W.; Valentine, J. S.; Solomon, E. I. Spectroscopic and Geometric Variations in Perturbed Blue Copper Centers: Electronic Structures of Stellacyanin and Cucumber Basic Protein. *J. Am. Chem. Soc.* **1998**, *120* (37), 9621–9631.

(5) Romero, A.; Hoitink, C. W.; Nar, H.; Huber, R.; Messerschmidt, A.; Canters, G. W. X-Ray Analysis and Spectroscopic Characterization of M121Q Azurin. A Copper Site Model for Stellacyanin. *J. Mol. Biol.* **1993**, *229* (4), 1007–1021.

(6) Kroes, S. J.; Salgado, J.; Parigi, G.; Luchinat, C.; Canters, G. W. Electron Relaxation and Solvent Accessibility of the Metal Site in Wild-Type and Mutated Azurins as

Determined from Nuclear Magnetic Relaxation Dispersion Experiments. *J. Biol. Inorg. Chem.* **1996**, *1* (6), 551–559.
(7) Messerschmidt, A.; Prade, L.; Kroes, S. J.; Sanders-Loehr, J.; Huber, R.; Canters, G. W. Rack-Induced Metal Binding vs. Flexibility: Met121His Azurin Crystal Structures at Different pH. *Proc. Natl. Acad. Sci. U. S. A.* **1998**, *95* (7), 3443–3448.
(8) Kroes, S. J.; Hoitink, C. W. G.; Andrew, C. R.; Ai, J.; Sanders-Loehr, J.; Messerschmidt, A.; Hagen, W. R.; Canters, G. W. The Mutation Met121His Creates a Type-1.5 Copper Site in Alcaligenes Denitrificans Azurin. *Eur. J. Biochem.* **1996**, *240* (2), 342–351.
(9) Hosseinzadeh, P.; Marshall, N. M.; Chacón, K. N.; Yu, Y.; Nilges, M. J.; New, S. Y.; Tashkov, S. A.; Blackburn, N. J.; Lu, Y. Design of a Single Protein That Spans the Entire 2-V Range of Physiological Redox Potentials. *Proc. Natl. Acad. Sci.* **2016**, *113* (2), 262–267.
(10) Daugherty, R. G.; Wasowicz, T.; Gibney, B. R.; DeRose, V. J. Design and Spectroscopic Characterization of Peptide Models for the Plastocyanin Copper-Binding Loop. *Inorg. Chem.* **2002**, *41* (10), 2623–2632.
(11) Plegaria, J. S.; Duca, M.; Tard, C.; Friedlander, T. J.; Deb, A.; Penner-Hahn, J. E.; Pecoraro, V. L. De Novo Design and Characterization of Copper Metallopeptides Inspired by Native Cupredoxins. *Inorg. Chem.* **2015**, *54* (19), 9470–9482.
(12) Kitajima, N.; Fujisawa, K.; Tanaka, M.; Morooka, Y. X-Ray Structure of thiolatocopper(II) Complexes Bearing Close Spectroscopic Similarities to Blue Copper Proteins. *J. Am. Chem. Soc.* **1992**, *114* (23), 9232–9233.
(13) Holland, P. L.; Tolman, W. B. Three-Coordinate Cu(II) Complexes: Structural Models of Trigonal-Planar Type 1 Copper Protein Active Sites. *J. Am. Chem. Soc.* **1999**, *121* (31), 7270–7271.
(14) Wilson, M. E.; Whitesides, G. M. Conversion of a Protein to a Homogeneous Asymmetric Hydrogenation Catalyst by Site-Specific Modification with a diphosphinerhodium(I) Moiety. *J. Am. Chem. Soc.* **1978**, *100* (1), 306–307.
(15) Heinisch, T.; Ward, T. R. Artificial Metalloenzymes Based on the Biotin-Streptavidin Technology: Challenges and Opportunities. *Acc. Chem. Res.* **2016**, *49* (9), 1711–1721.
(16) Weber, P. C.; Ohlendorf, D. H.; Wendoloski, J. J.; Salemme, F. R. Structural Origins of High-Affinity Biotin Binding to Streptavidin. *Science* **1989**, *243* (4887), 85–88.
(17) Karlin, K. D.; Kaderli, S.; Zuberbühler, A. D. Kinetics and Thermodynamics of Copper(I)/Dioxygen Interaction. *Acc. Chem. Res.* **1997**, *30* (3), 139–147.
(18) Skander, M.; Humbert, N.; Collot, J.; Gradinaru, J.; Klein, G.; Loosli, A.; Sauser, J.; Zocchi, A.; Gilardoni, F.; Ward, T. R. Artificial Metalloenzymes: (Strept)avidin as Host for Enantioselective Hydrogenation by Achiral Biotinylated Rhodium-Diphosphine Complexes. *J. Am. Chem. Soc.* **2004**, *126* (44), 14411–14418.
(19) Thyagarajan, S.; Murthy, N. N.; Narducci Sarjeant, A. A.; Karlin, K. D.; Rokita, S. E. Selective DNA Strand Scission with Binuclear Copper Complexes: Implications for an Active Cu2-O2 Species. *J. Am. Chem. Soc.* **2006**, *128* (21), 7003–7008.
(20) Zimbron, J. M.; Heinisch, T.; Schmid, M.; Hamels, D.; Nogueira, E. S.; Schirmer, T.; Ward, T. R. A Dual Anchoring Strategy for the Localization and Activation of Artificial Metalloenzymes Based on the Biotin–Streptavidin Technology. *J. Am. Chem. Soc.* **2013**, *135* (14), 5384–5388.
(21) Hosseinzadeh, P.; Tian, S.; Marshall, N. M.; Hemp, J.; Mullen, T.; Nilges, M. J.; Gao, Y.-G.; Robinson, H.; Stahl, D. A.; Gennis, R. B.; Lu, Y. A Purple Cupredoxin from Nitrosopumilus Maritimus Containing a Mononuclear Type 1 Copper Center with an

Open Binding Site. *J. Am. Chem. Soc.* **2016**, *138* (20), 6324–6327.
(22) Malmström, B. G.; Reinhammar, B.; Vänngård, T. The State of Copper in Stellacyanin and Laccase from the Lacquer Tree Rhus Vernicifera. *Biochim. Biophys. Acta* **1970**, *205* (1), 48–57.
(23) Reinhammar, B. R. Oxidation-Reduction Potentials of the Electron Acceptors in Laccases and Stellacyanin. *Biochim. Biophys. Acta* **1972**, *275* (2), 245–259.
(24) Hart, P. J.; Nersissian, A. M.; Herrmann, R. G.; Nalbandyan, R. M.; Valentine, J. S.; Eisenberg, D. A Missing Link in Cupredoxins: Crystal Structure of Cucumber Stellacyanin at 1.6 A Resolution. *Protein Sci.* **1996**, *5* (11), 2175–2183.
(25) Lancaster, K. M.; Zaballa, M.-E.; Sproules, S.; Sundararajan, M.; DeBeer, S.; Richards, J. H.; Vila, A. J.; Neese, F.; Gray, H. B. Outer-Sphere Contributions to the Electronic Structure of Type Zero Copper Proteins. *J. Am. Chem. Soc.* **2012**, *134* (19), 8241–8253.
(26) Randall, D. W.; George, S. D.; Hedman, B.; Hodgson, K. O.; Fujisawa, K.; Solomon, E. I. Spectroscopic and Electronic Structural Studies of Blue Copper Model Complexes. 1. Perturbation of the Thiolate−Cu Bond. *J. Am. Chem. Soc.* **2000**, *122* (47), 11620–11631.
(27) Pangborn, A. B.; Giardello, M. A.; Grubbs, R. H.; Rosen, R. K.; Timmers, F. J. Safe and Convenient Procedure for Solvent Purification. *Organometallics* **1996**, *15*, 1518–1520.
(28) Chambers, J. M.; Lindqvist, L. M.; Webb, A.; Huang, D. C. S.; Savage, G. P.; Rizzacasa, M. A. Synthesis of Biotinylated Episilvestrol: Highly Selective Targeting of the Translation Factors eIF4AI/II. *Org. Lett.* **2013**, *15* (6), 1–25.
(29) Leaver, S. A.; Palaniandavar, M.; Kilner, C. A.; Halcrow, M. A. A New Synthesis of bis(2-{pyrid-2-Yl}ethyl)amine (LH) from bis(2-{pyrid-2-Yl}ethyl)hydroxylamine (LOH), and the Copper-Dependent Reduction of LOH to LH. *Dalt. Trans.* **2003**, No. 22, 4224.
(30) Incarvito, C.; Lam, M.; Rhatigan, B.; Rheingold, A. L.; Qin, C. J.; Gavrilova, A. L.; Bosnich, B. Bimetallic Reactivity. Preparations, Properties and Structures of Complexes Formed by Unsymmetrical Binucleating Ligands Bearing 4- and 6-Coordinate Sites Supported by Alkoxide Bridges. *J. Chem. Soc. Dalt. Trans.* **2001**, No. 23, 3478–3488.
(31) Petasis, D. T.; Hendrich, M. P. Quantitative Interpretation of Multifrequency Multimode EPR Spectra of Metal Containing Proteins, Enzymes, and Biomimetic Complexes. *Methods Enzymol.* **2015**, *563*, 171–208.
(32) Kabsch, W. Integration, Scaling, Space-Group Assignment and Post-Refinement. *Acta Crystallogr. Sect. D Biol. Crystallogr.* **2010**, *66* (2), 133–144.
(33) Evans, P. R. An Introduction to Data Reduction: Space-Group Determination, Scaling and Intensity Statistics. *Acta Crystallogr. Sect. D Biol. Crystallogr.* **2011**, *67* (4), 282–292.
(34) Murshudov, G. N.; Vagin, A. A.; Dodson, E. J. Refinement of Macromolecular Structures by the Maximum-Likelihood Method. *Acta Crystallogr. D. Biol. Crystallogr.* **1997**, *53* (3), 240–255.
(35) Adams, P. D.; Afonine, P. V; Bunkóczi, G.; Chen, V. B.; Davis, I. W.; Echols, N.; Headd, J. J.; Hung, L.-W.; Kapral, G. J.; Grosse-Kunstleve, R. W.; McCoy, A. J.; Moriarty, N. W.; Oeffner, R.; Read, R. J.; Richardson, D. C.; Richardson, J. S.; Terwilliger, T. C.; Zwart, P. H. PHENIX: A Comprehensive Python-Based System for Macromolecular Structure Solution. *Acta Crystallogr. D. Biol. Crystallogr.* **2010**, *66* (2), 213–221.
(36) Blain, I.; Giorgi, M.; De Riggi, I.; Reglier, M. Substrate-Binding Ligand Approach in Chemical Modeling of Copper-Containing Monooxygenases, 1 Intramolecular Stereoselective Oxygen Atom Insertion into a Non-Activated C–H Bond. *Eur. J. Inorg.*

Chem. **2000**, *2000* (2), 393–398.
(37) Karlin, K. D.; Shi, J.; Hayes, J. C.; McKown, J. W.; Hutchinson, J. P.; Zubieta, J. Cu(I)—dioxygen Reactivity: Structural Characterization of a Bridged-Binuclear Cu(II) Complex Formed by Oxidation of a New Binuclear Cu(I) Compound. *Inorganica Chim. Acta* **1984**, *91* (1), L3–L7.
(38) Emsley, P.; Cowtan, K. Coot: Model-Building Tools for Molecular Graphics. *Acta Crystallogr. D. Biol. Crystallogr.* **2004**, *60* (Pt 12 Pt 1), 2126–2132.

CHAPTER 3

Coordination Chemistry within a Protein Host: Regulation of the Secondary Coordination Sphere

Introduction

Synthetic inorganic chemists have focused much effort on the ability to control the primary coordination sphere around metal ions using organic ligand scaffolds. These covalently bound ligands help control key properties of the complex, such as electronic structure and redox properties. While these primary coordination sphere interactions are important, non-covalent interactions in the microenvironment, which includes the secondary coordination sphere, also play a vital role.[1–5] Structure-function studies on metalloproteins active sites have revealed the importance of these non-covalent interactions and have shown the role they play in tuning redox potentials and pK_a values, as well as assisting in ligand binding and stabilizing reactive species.[6,7] Hydrogen bonds (H-bonds) are the most prevalent non-covalent interaction observed in metalloproteins, and thus designing systems to install and examine the architectural features necessary to control these secondary coordination sphere interactions are of interest. As discussed in Chapter 1, many groups have developed purely synthetic systems using rigid ligand scaffolds to enforce formation of H-bonding interactions.[3,8–19]

Instead of using a synthetic organic ligand scaffold to control the secondary coordination sphere interactions, artificial metalloproteins (ArMs) offer another system that can be used to probe the effects of the microenvironment, including longer range interactions such as water channels, on metal active sites. There are many approaches to prepare ArMs, some of which have been discussed in Chapters 1 and 2.[20–26] Biotin-streptavidin (Sav) technology has been shown to be an effective method for producing ArMs.

There are numerous examples showing that incorporation of biotinylated organometallic complexes into Sav can produce highly selective artificial metalloenzymes.[22,27] Many systems have focused on catalytic function and thus, the role of the secondary coordination sphere is often inferred from reactivity and/or selectivity studies with different variants. In addition, the binding of external ligands or substrates is seldom observed, especially by X-ray diffraction (XRD) methods. As was discussed for the work by Ménage and coworkers in Chapter 1,[19] the ability to compare structural information with spectroscopic data collected *in situ* could provide a powerful tool to understand the effects of the secondary coordination sphere on metallo-active sites.

In Chapter 2, it was demonstrated that biotin-Sav technology could be used to engineer active sites that mimic many of the properties found for Type 1 Cu sites in cupredoxins.[28] This was done through spectroscopic and structural analysis of biotinylated Cu^{II} complexes anchored within a cysteine-containing variant of Sav. Many design principles were established in developing artificial Type 1 Cu sites, however they were predominantly focused on the primary coordination sphere of the immobilized copper center. The structure of $[Cu^{II}(\text{biot-et-dpea})(H_2O)_2]^{2+}\subset$Sav WT (**1a**) provided an excellent of example of how Sav can provide H-bonding interactions to a ligand coordinated to the copper complex. A coordinated water molecule (O2) was involved in an H-bonding network that included a structural water molecule (O1), the backbone carbonyl of A86, and the hydroxyl group of S112 (Fig. 3-1A, Table 3-1). This H-bonding network could be utilized to interact with an exogenous ligand (besides water).

This chapter describes how Sav can be used to regulate the binding of an external azide ion through control of the secondary coordination sphere. Taking advantage of the H-

bond network found in **1a**, as well as newly discovered H-bonding interactions, investigations done in solution and *in crystallo* provide evidence that modulation of the secondary coordination sphere can be achieved through changes in the H-bonding networks provided by the protein host.

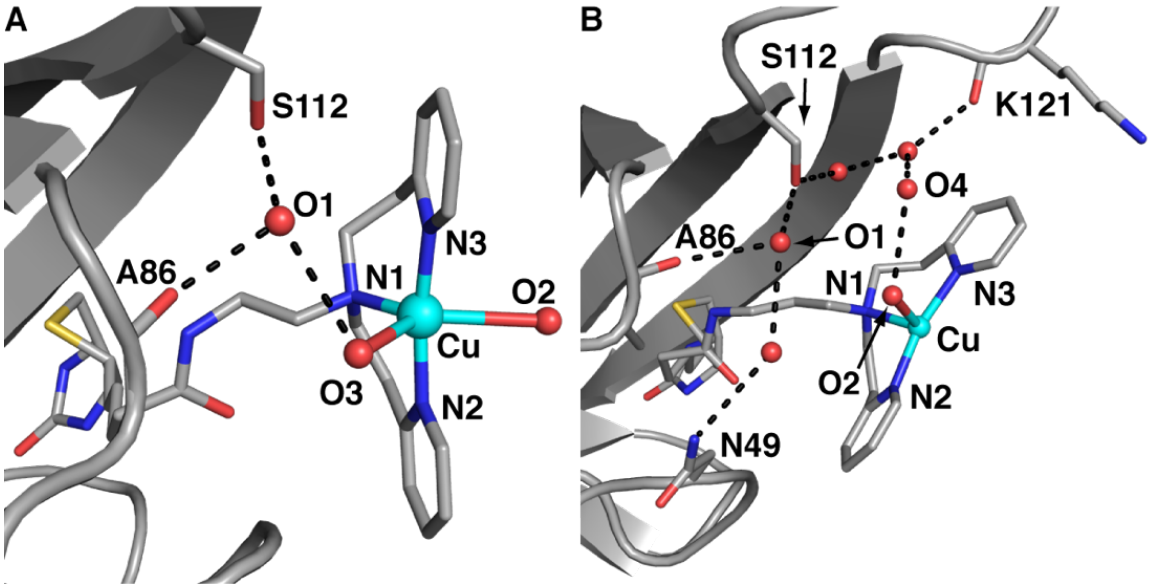

Figure 3-1. Molecular structures of **1** (**A,** PDB: 5K49) and **2** (**B**). Dashed lines indicate H-bonds.

Results and Discussion

The copper ArMs $[Cu^{II}(biot\text{-}n\text{-}dpea)(H_2O)_2]^{2+}\subset$Sav WT (n= et (**1a**) or pr (**1b**)) described in Chapter 2 were the starting points for this study. As described above and in Chapter 2, the molecular structure of **1a** showed a trigonal bipyramidal copper complex within each subunit of Sav that had two aqua ligands, one of which is involved in an extended H-bonding network. Singles crystals of **1b** were also obtained showing that the longer propyl spacer places the copper center 2 Å further from the biotin binding site. This placement induced a substantial structural change within the secondary coordination sphere with O1 no longer directly interacting with the aqua ligand of the complex. A new H-bonding network was observed in **1b** that is more extensive than in **1a.** The aqua ligand containing O2 forms

Table 3-1. Selected Bond Lengths (Å) and Angles (°) for **1a**, **1a-N$_3$**, **1b**, and **1b-N$_3$**

Metrical Parameters	**1a**	**1a-N$_3$**	**1b**	**1b-N$_3$**
Cu–N1	2.08(3)	2.10(3)	2.17(2)	2.14(3)
Cu–N2	2.02(3)	1.99(3)	2.07(2)	2.13(3)
Cu–N3	2.09(3)	2.11(3)	2.10(2)	2.04(3)
Cu–N4	–	1.88(3)	–	1.87(3)
Cu-O2	2.46(3)	–	2.32(2)	2.29(3)
Cu-O3	2.52(3)	–[a]	–[a]	–
τ_5[29]	0.72	–[a]	–[a]	0.52
N1–Cu–N2	102(3)	97(3)	94(3)	93(3)
N1–Cu–N3	88(3)	84(3)	101(3)	88(3)
N1–Cu–N4	–	106(3)	–	112(3)
N2–Cu–N3	170(3)	178(3)	165(3)	178(3)
N2–Cu–N4	–	95(3)	–	68(3)
N3–Cu–N4	–	87(3)	–	110(3)
N1–Cu–O2	127(3)	–	100(3)	96(3)
N2–Cu–O2	84(3)	–	91(3)	95(3)
N3–Cu–O2	88(3)	–	87(3)	86(3)
N4–Cu–O2	–	–[a]	–[a]	147(3)
N1–Cu–O3	104(3)	–[a]	–[a]	–
N2–Cu–O3	86(3)	–[a]	–[a]	–
N3–Cu–O3	94(3)	–[a]	–[a]	–

[a]aqua ligand in trigonal plane only visible in electron density F_o-F_c omit map at <3σ

a H-bond with a water molecule (O4) which further interacts with other water molecules (including O1) and residues K121, S112, and A86 within the active site (Fig. 3-1B and Table 3-1). Only weak electron density was observed for a second aqua ligand in the trigonal plane and therefore was not modelled (see experimental section). Spectroscopic data, however, suggests that the copper center in **1b** has a similar geometry in solution to **1a** (Table 3-2). These structural results further support the premise that changes in length of the linker group can be used to change the position of metal complexes within Sav.[28]

Preparation of Cu–N$_3$ ArMs. ArMs **1a** and **1b** contained water ligands which should be substitutionally labile, providing an opportunity to examine the effects of binding external ligands to the anchored Cu^{II} complexes. The binding of azide ions to **1a** and **1b** was examined

Table 3-2. Spectroscopic Data for ArMs

ArM	Abs λ_{max}, nm (ε, M^{-1} cm^{-1})[a]	CD λ_{max}, nm	g	A (MHz)
1a	625 (90)	333	2.05 2.22 2.26	522 484
1a-N_3	390 (6000) 750 (390)	324 382 445	2.07 2.23	430
3a	634 (120)	336	2.06 2.22 2.25	476 520
3a-N_3	390 ([b]) 702 ([b])	332 390 448	2.08 2.23	425
4a	616 (80)	334	2.06 2.22 2.27	487 497
4a-N_3	389 ([b]) 750 ([b])	334 379 439	2.07 2.23	455
1b	625 (100)	335	2.06 2.22 2.25	477 524
1b-N_3	393 (3200) 698 (290)	342 392 457	2.08 2.23	457
5b	620(120)	339	2.06 2.23 2.26	477 528
5b-N_3	390 (3300) 690 (290)	385 452	2.07 2.22	480

[a] extinction coefficients were calculated from extrapolated maximum intensities at infinite azide concentrations; [b] extinction coefficients were unable to be calculated due to poor azide binding

to probe changes in both the primary and secondary coordination spheres of the Cu^{II} centers. Cu^{II}–N_3 complexes are known to exhibit a strong azido-to-Cu^{II} ligand-to-metal charge transfer (LMCT) band that can be used to follow ligand binding in solution.[10,30–34] Azide ions have been used in many copper-containing metalloproteins, as well as synthetic complexes, to probe the structure and electronic properties in solution.[30,31,35–44] For example, Casella and coworkers studied binding of azide ions to a series of Cu^{II} complexes prepared with tridentate ligands[33] and, as discussed in Chapter 1, Masuda prepared a series of tripodal

ligands bearing different number of H-bond donors to study their effect on the electronic structure of Cu^{II}–azido complexes.[10]

Treating **1a** and **1b** with up to 40-fold excess of NaN_3 at pH 6 produced ArMs **1a-N_3** and **1b-N_3** containing a new absorption band at λ_{max} = 390 nm assigned to the N_3^-–Cu^{II} LMCT transition. Additionally, changes in the d–d bands were observed that are similar to those reported for related Cu^{II}–N_3 complexes (Figs. 3-2A-B and A-3, Table 3-2)).[10,34] Circular dichroism (CD) spectra were also collected of **1a-N_3** and **1b-N_3** showing strong bands associated with the LMCT transitions, supporting the optical bands observed arise from species influenced by the chiral environment enforced by the protein host (Figs. 3-2C-D and A-3, Table 3-2).[33] As expected, no CD signals were observed for Cu^{II}–N_3 complexes prepared in solution without of Sav. The EPR spectra of **1a-N_3** and **1b-N_3** showed only one predominant Cu^{II} species with a decreased hyperfine coupling constant (A), relative to **1a** and **1b,** consistent with azide-coordinated Cu^{II} complexes (Table 3-2).[10,33,42–44] These spectroscopic data for **1a** and **1b** are thus consistent with the formation of mononuclear Cu^{II}–N_3 centers within Sav WT in solution.

In Crystallo Studies. The molecular structures of **1a-N_3** and **1b-N_3** were determined using XRD methods. *In crystallo* preparation of **1a-N_3** and **1b-N_3** was accomplished by incubating single crystals of **1a** and **1b** in cryo-protectant containing 1.0 mM NaN_3 at pH 6 resulting in crystals changing from blue to green (Fig. 3-3A-B). The structure of **1a-N_3** was solved to 1.37 Å resolution showing a four-coordinate mononuclear Cu complex within each subunit of Sav. The dpea ligand is coordinated in a meridional fashion, as in **1a**, with an average Cu–N_{dpea} bond length of 2.07(3) Å (Fig. 3-3C, Table 3-1). Weak electron density (<3σ) was observed for an aqua ligand in the F_o-F_c omit map(O3 in **1**, see crystallographic

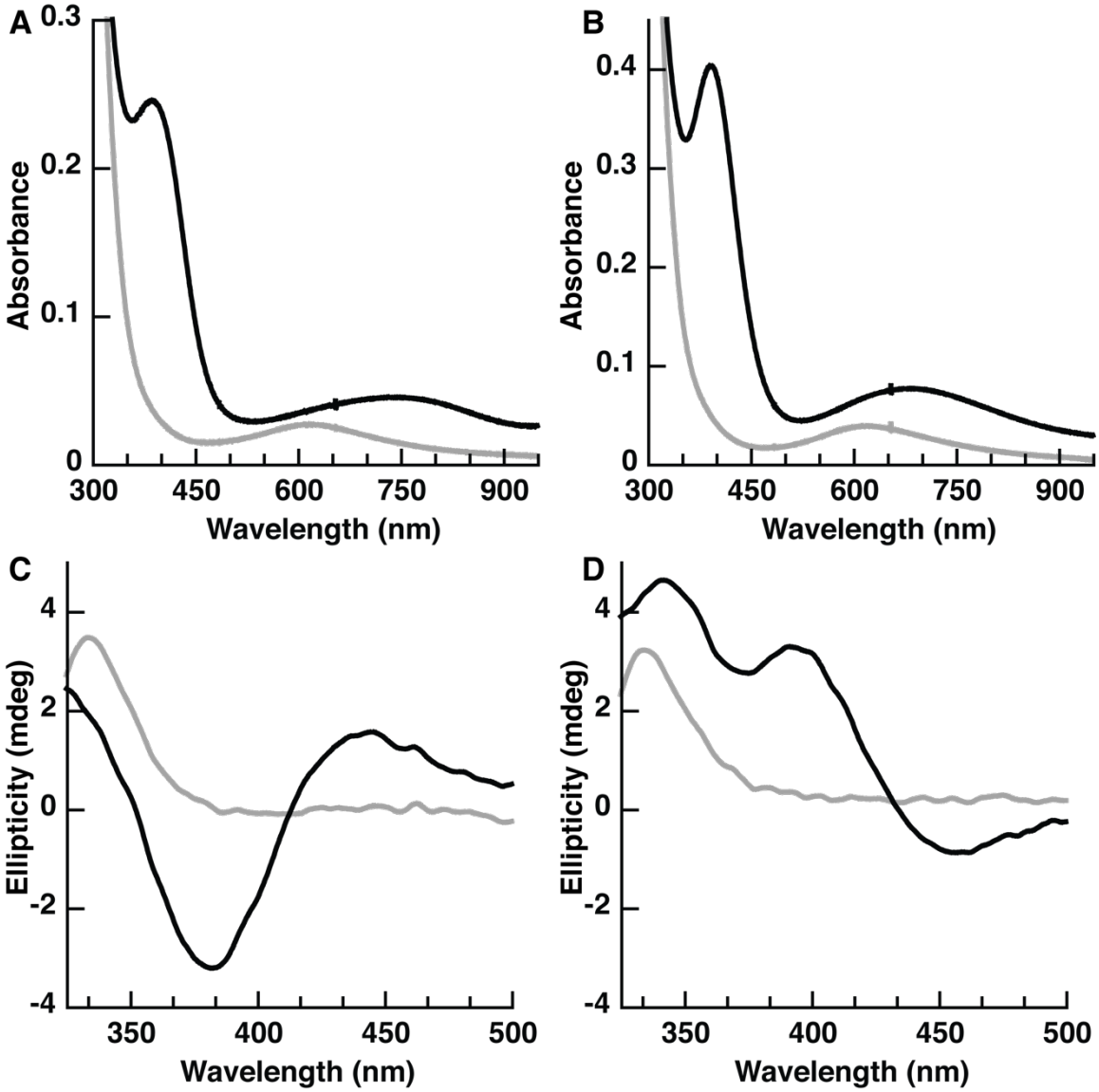

Figure 3-2. UV-vis and CD spectra of **1a/1a-N$_3$** (**A&C**) and **1b/1b-N$_3$** (**B&D**). **1a-b** are in grey and **1a-N$_3$** and **1b-N$_3$** are in black.

refinement in the experiment section).The stick-like electron density for a fourth ligand was accurately modeled as a three-atom unit assigned to a terminally coordinated azido ligand with a Cu–N4 bond length of 1.88(3) Å (Fig. 3-3D). The metrical parameters observed in **1a-N$_3$** are similar to those reported for other Cu^{II}–N_3 complexes,[10,34,45] such as the trigonal bipyramidal complex $[Cu^{II}(tpa)N_3]^+$ (tpa = tris(2-pyridylmethyl)amine) which has a Cu–N_{azido} bond length of 1.935(9) Å and an average N_{tpa}–Cu–N_{azido} bond angle of 99°.[10]

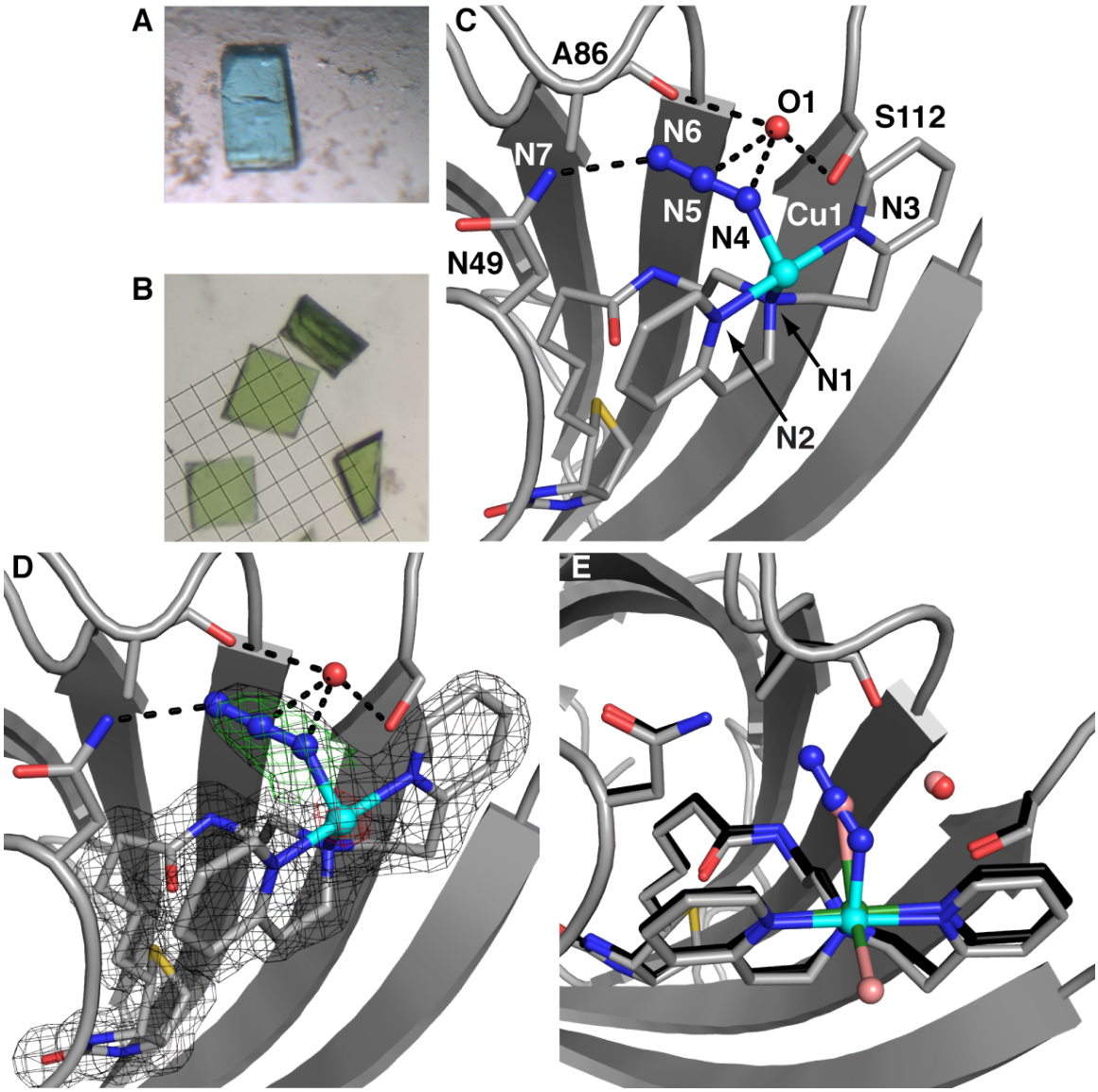

Figure 3-3 Photographs comparing crystals of **1a** (**A**) and **1a**-N_3 (**B**), the molecular structure of **1a**-N_3 (**C** & **D**), and structural overlay of **1a** and **1a**-N_3 (**E**). For the structure in D the position of the complex is indicated by the $2F_o$-F_c electron density (grey, contoured at 1σ), anomalous difference density (red, contoured at 15σ) and the azido ligand position is indicated with F_o-F_c omit map (green, contoured at 3σ). Copper ions are colored in cyan, nitrogen atoms are colored in blue, and oxygen atoms/water molecules are colored in red. H-bonds are displayed as dashed black lines. In E, **1a** is shown with carbon atoms in black, nitrogen atoms in blue, water molecules in salmon, and copper ions in green.

Hydrogen Bonding Network. One prominent feature of the structure of **1a-N_3** is the H-bonding network around the Cu–N_3 unit. Overlaying structures of **1a** and **1a-N_3** shows that the Cu(dpea) fragments are positioned in similar positions in both ArMs (Fig. 3-3E). This

comparison illustrates that the azido ligand displaces the aqua ligand (O2) in **1a**. This specific coordination site faces the azido ligand inward, toward the biotin binding site properly positioning it to form H-bonds. The H-bonding network observed in **1a** is conserved, however O1 is now H-bonded to N4 and N5 of the azido ligand. This H-bonding network extends from S112 to the backbone carbonyl of K121 through two other water molecules. Another H-bonding network was observed involving the distal N-atom of the azido ligand (N6) and nearby residue N49 (Fig. 3-4). This H-bond network also extends beyond the azido–N49 interaction. The carboxylate side chain of E51 is H-bonded to the HN_{ε} of the guanidinium side chain of R84, positioning $H_2N_{\eta 2}$ of R84 to donate an H-bond to the carbonyl of the N49 side chain. This network orients N49 and suggests that it donates an H-bond from the HN_{δ} of the amide side chain to N6 of the azido ligand (Fig. 3-4). This extended H-bond network that includes N49, R84, and E51 is formed upon biotin (or biotinylated complex) binding. Residues45-52 form a flexible loop that sits in an open conformation in apo-Sav, but closes

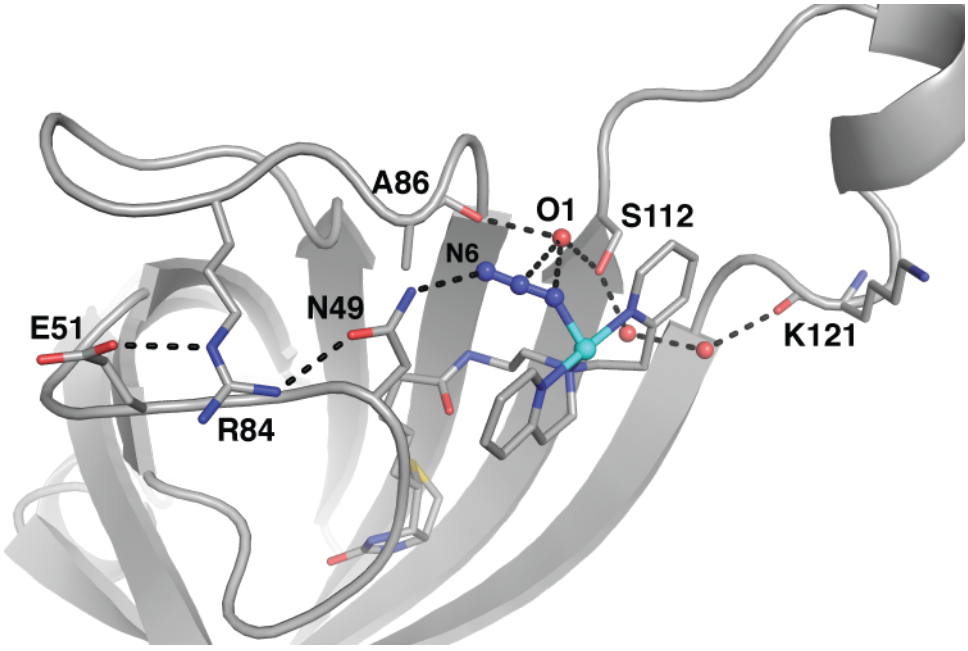

Figure 3-4. Structure of **1a-N_3** showing the extended H-bonding network that includes residues E51, R84, and N49.

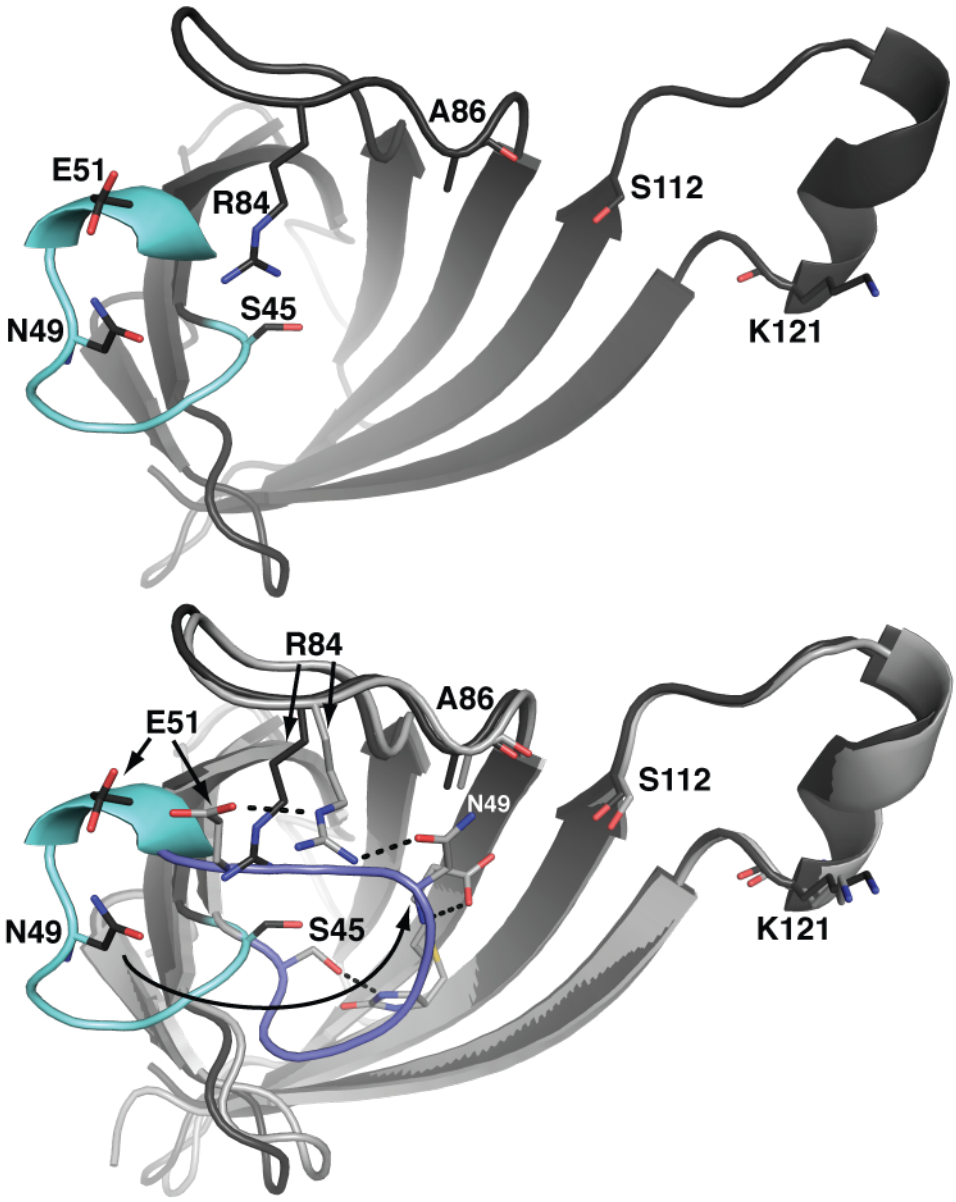

Figure 3-5. Structure of apo-Sav WT (top, PDB: 1SWC) with the flexible loop shown in teal and structural overlay (bottom) of apo-Sav WT (black) and biotin⊂Sav WT (grey, flexible loop is blue, PDB: 1SWE). Upon biotin binding, the flexible loop closes over biotin (teal to blue), S45 H-bonds to biotin, locking E51, R84, and N49 into an H-bonding network. H-bonds are shown as black dashed lines.

upon binding within the biotin binding site (Fig. 3-5).[46] In the open form, residues N49, R84, and E51 are not properly positioned to H-bond to each another. However, upon biotin binding, residues S45 and N49 H-bond to biotin causing the loop to close over the biotin binding site and thus orienting residues N49 and E51 on either side of R84, locking the orientation of all three residues. This H-bonding network is an illustration of the predictable long-range non-covalent interactions provided by the protein host that are difficult to engineer into purely synthetic systems.

*Structure of **1b-N$_3$***. The structure of **1b-N$_3$** was solved to 1.45 Å resolution and also showed a mononuclear copper complex within each subunit that has a geometry between trigonal bipyramidal and square pyramidal (τ_5 = 0.52, Fig. 3-6, Table 3-1).[29] The distorted square plane is composed of the two N-atom donors from the dpea prydines, an O-atom from an aqua ligand (O2), and an N-atom donor (N4) from the terminal azido ligand. The primary coordination sphere is completed by the amine N-atom of dpea which occupies the axial position. The metrical parameters are consistent with this assignment in which the O2–Cu–

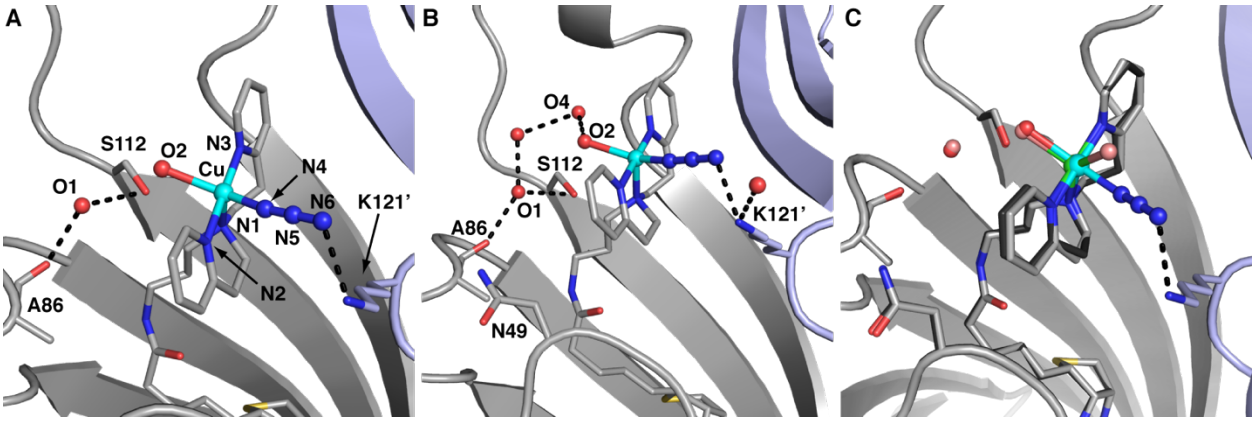

Figure 3-6. Molecular structure of **1b-N$_3$** showing the primary coordination sphere (**A**) and including the extended H-bonding network (**B**) and a structural overlay of **1b** and **1b-N$_3$** (**C**). Dashed lines indicate H-bonds. K121' is from the adjacent subunit (shown in light blue). Copper ions are colored in cyan, nitrogen atoms are colored in blue, and oxygen atoms/water molecules are colored in red. Atom labels for the structure in **B** are the same as in **A**. In **C**, **1b** is shown with carbon atoms in black, oxygen atoms/water molecules in salmon, and Cu ions in green.

N4 bond angle is 147(4)˚ and Cu–N4 and Cu–O2 bond lengths are 1.87(3) and 2.29(3) Å, respectively. Compared to **1a-N_3**, the Cu center in **1b-N_3** is located about 2 Å further from the biotin binding site, towards the adjacent subunit. This location change is due to the propyl spacer and places the metal cofactor far enough from N49 and O1 that they can no longer form H-bonds with the azido ligand. Instead, the azido ligand is in a coordination site on the Cu center (relative to **1b**) that allows it to form a single H-bond with residue K121' (' indicates a residue from the adjacent subunit, Fig. 3-6). The aqua ligand is also part of an extended H-bonding network that includes several water molecules, but not N49.

Solution Binding Studies. Equilibrium constants (*K*) were determined to further investigate the effects of the H-bonding networks on the confinement of Cu^{II}–N3 complexes. To establish the effect of the H-bonding interactions on azide binding, *K* was determined for **1a-N_3** and **1b-N_3** as well as three other variants where specific H-bonding interactions are removed: $[Cu^{II}(\text{biot-et-dpea})(H_2O)_2]^{2+}$⊂Sav N49A (**3a**), $[Cu^{II}(\text{biot-et-dpea})(H_2O)_2]^{2+}$⊂Sav S112A (**4a**), and $[Cu^{II}(\text{biot-pr-dpea})(H_2O)_2]^{2+}$⊂Sav K121A (**5b**). We hypothesized that these mutations were alter the H-bonds to the azido ligand which could affect binding. Equilibrium studies were performed spectrophotometrically by monitoring changes in the LMCT band of the Cu^{II}–N_3 complexes (Figs. 3-7 and A-4).[33] These studies also provided Hill coefficients (*n*, Table 3-3, see experimental section) confirming 1:1 binding of azide ions to Cu^{II} complexes which is consistent with non-cooperative binding of a terminal azido ligand. An $K = 23 \pm 4$ M^{-1} was measured for the formation of **1a-N_3** that decreased to an $K = 6 \pm 2$ M^{-1} for **3a-N_3** and an $K = 12 \pm 2$ M^{-1} for **4a-N_3**. A smaller, but still statistically significant trend was found for variants with the propyl spacer: an $K = 68 \pm 5$ M^{-1} was measured for **2b-N_3** which decreased to $K = 56 \pm 3$ M^{-1} for **5b-N_3** (Table 3-3).

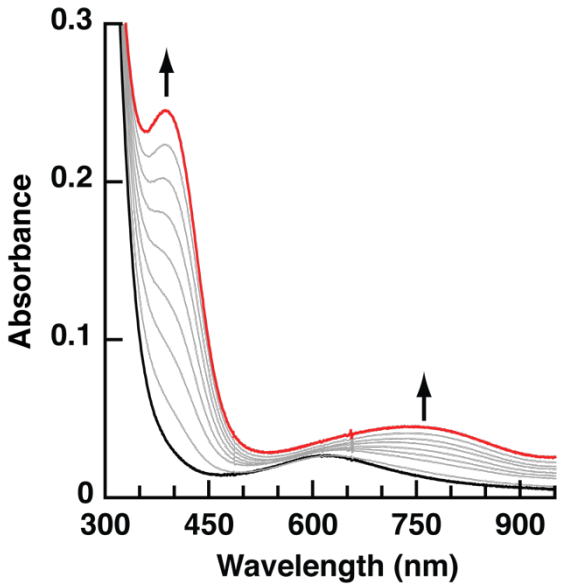

Figure 3-7. Spectrophotometric titration of **1a** to **1a-N$_3$** Initial spectrum is in black and the final spectrum is in red.

Table 3-3. Equilibrium Constants (K) and Hill Coefficients (n) for ArMs

ArM	K (M^{-1})[a]	n
1a	–	–
1a-N$_3$	23 ± 4	1.2
3a	–	–
3a-N$_3$	6 ± 2	0.99
4a	–	–
4a-N$_3$	12 ± 2	0.99
1b	–	–
1b-N$_3$	68 ± 5	0.98
5b	–	–
5b-N$_3$	56 ± 3	0.99

[a]measured at 294 K.

The trend in equilibrium constants within each variant support the premise that the secondary coordination sphere H-bonds provided by Sav influence azide ion binding. For variants with $[Cu^{II}(biot\text{-}et\text{-}dpea)]^{2+}$, K was reduced by nearly a factor of 4 when the H-bonding network was altered via mutation of N49 to alanine. This difference corresponds to a change in free energy of ~1.7 kcal/mol which is attributed to the loss of the distal H-bond to the azido ligand. Replacing S112 with an alanine in **4a** decreases the occupancy of the

structural water molecule (O1) (see Chapter 4),[47] eliminating the bifurcated H-bond to N4 and N5 of the azido ligand. The disruption of this H-bond causes a 2-fold decrease in *K*, corresponding to ~1.4 kcal/mol change in free energy. A similar effect of ~1.5 kcal/mol was measured for ArMs containing $[Cu^{II}(biot\text{-}pr\text{-}dpea)]^{2+}$ in which the distal H-bond was removed via mutation of K121 to an alanine residue. The values for *K* measured for these ArMs is consistent with the range of *K* values measured for synthetic Cu^{II} complexes in aqueous solutions (K = 10-298 M^{-1}).[33] Larger values are found for **1b-N$_3$** and **5b-N$_3$** (relative to **1a-N$_3$**, **3a-N$_3$**, and **4a-N$_3$**) which is likely due to the complexes being placed closer to the protein surface and are thus more accessible for binding.

Summary and Conclusion

Monitoring azide ion binding to confined Cu^{II} complexes afforded insight into the design of metalloprotein active sites. This work showed that manipulation of H-bonding networks can regulate the secondary coordination sphere around anchored metal complexes. Using *in crystallo* structural studies, binding of an external ligand was verified and H-bonding networks were identified. The structure of **1a-N$_3$** showed that N49 and the structural water O1 provide a local environment rich in H-bonding interactions to a coordinated azido ligand. The placement of the cofactor using an ethyl spacer positioned the complex to take advantage of these non-covalent interaction. Using a longer, propyl spacer in **1b-N$_3$** places the copper center in a new location further from the biotin binding site that provided a new H-bond to the azido ligand. These structural findings further demonstrate the importance of controlling the placement of the cofactor within the Sav vestibule. Additional structural tuning was accomplished via mutation of proximal residues that disrupted H-bonding interactions. Deletion of single H-bonding interactions decreased the

equilibrium binding constant of the azido ligands, emphasizing the importance of these non-covalent interactions in regulating properties in ArMs. This work established design principles necessary to control the secondary coordination sphere around metal ions using biotin-Sav technology.

Experimental

General Methods. All commercially available reagents were obtained of the highest purity and used as received. Dimethylsulfoxide (DMSO), *N,N*-dimethylformamide (DMF), and diethyl ether were degassed with argon and dried by vacuum filtration through activated alumina according to the procedure by Grubbs.[48] Triethylamine was distilled from KOH. Thin-layer chromatography (TLC) was performed on Whatman 250 μm layer 6 Å glass-backed silica gel plates. Eluted plates were visualized using UV light. Silica gel chromatography was performed with the indicated solvent system using Fisher reagent silica gel 60 (230-400 mesh). The ligands (biot-et-dpea and biot-pr-dpea) and Cu^{II} complexes ($[Cu^{II}$(biot-et-dpea)$Cl_2]H_2O$ and $[Cu^{II}$(biot-pr-dpea)$Cl_2]H_2O$) were prepared as previously described in Chapter 2.[28]

Physical Methods

Instrumentation. Electronic absorbance spectra were recorded with an 8453 Agilent UV-vis spectrophotometer. Circular dichroism (CD) spectra were collected on a Jasco J-810 spectropolarimeter equipped with a 163-900 nm laser. X-band (9.64 GHz) EPR spectra were recorded on a Bruker EMX spectrometer equipped with Oxford liquid helium cryostats. EPR spectra were simulated using (*SpinCount*).[49]

Electronic Absorption Studies. A typical azide titration experiment was performed using a 500 μL solution of 75 μM Sav prepared in 50 mM MES buffer, pH 6 in a low-volume 1 cm cuvette.

15 µL of a 10 mM solution of $[Cu^{II}(biot\text{-}n\text{-}dpea)Cl_2]H_2O$ (n = et or pr) in DMF was added and allowed to equilibrate for 5 minutes. Azide was titrated 5 equivalents at a time (7.5 µL of a 1 M solution of NaN_3).

HABA Titrations. A 2.4 mL of a 8 µM solution of Sav in 200 mM phosphate buffer pH 7 was added to a 1 cm cuvette. 288 µL of a 10 mM (150 equivalents) HABA was added to ensure saturation of Sav. A 1 mM solution of $[Cu^{II}(biot\text{-}n\text{-}dpea)Cl_2]H_2O$ in DMF was added in 9.6 µL portions (0.5 equivalents) until 5 equivalents were added. The titration was monitored by UV-vis at λ_{max} = 506 nm (Fig. 3-8).

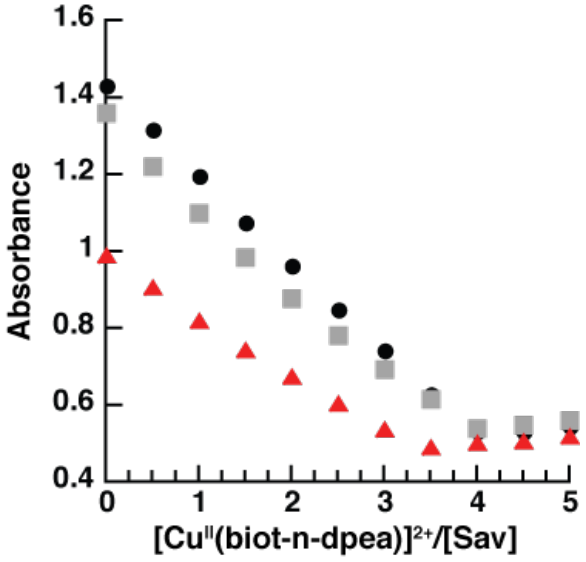

Figure 3-8. HABA titrations for **3a** (black circles), **4a** (grey squares), and **5b** (red triangles).

CD Studies. CD spectra were collected using a 500 µL solution of 75 µM Sav prepared in 50 mM MES buffer, pH 6. 15 µL of a 10 mM solution of $[Cu^{II}(biot\text{-}n\text{-}dpea)Cl_2]H_2O$ (n = et or pr) in DMF was added and allowed to equilibrate for 5 minutes. 40 equivalents (6 µL) were added from a 1.0 M solution of NaN_3. Spectra were collected with the following parameters: data pitch: 0.5 nm, DIT: 4 s, bandwidth: 2 nm, speed: 50 nm/min, and 4 accumulations.

EPR Experiments. To 250 μL of a 250 μM solution of Sav in 50 mM MES buffer, pH 6.0 was added 25 μL of a 10 mM solution of [Cu^{II}(biot-n-dpea)Cl_2]H_2O] (n = et or pr) in DMF. The solution was allowed to equilibrate for 5 minutes before addition of 40 equivalents of NaN_3 (10 μL of a 1 M solution). The solution was then transferred to an EPR tube and flash-frozen in liquid nitrogen.

Equilibrium Constant Determination.[33] To determine the effect of the H-bonding interaction on the binding affinity of azide to the anchored Cu complex, the binding equilibrium constants were determined for **1a-N_3**, **1b-N_3**, **3a-N_3**, **4a-N_3**, and **5b-N_3**. Azide binding studies were performed via addition of concentrated aqueous solutions of sodium azide to buffered solutions of Cu ArMs (see above). Despite being anchored within Sav, binding of the azide anion was rapid and therefore no incubation was necessary before measurement. We did not try to achieve saturation of the ligand binding sites on the Cu center because formation of Cu-azide adducts with a greater than 1:1 stoichiometry was possible and difficult to differentiate from 1:1 binding modes. The Sav host prohibits formation of azido-bridged dinuclear complexes. Following the methods described previously, the equilibrium constants were measured for each Cu ArM. Assuming 1:1 stoichiometry, the equilibrium constants can be determined using the following equilibrium expression:

$$K = \frac{[ML]}{[M][L]} = \frac{\Delta A}{(\Delta A_\infty - \Delta A)[L]} \qquad \text{Eq. 3-1}$$

where [M], [ML], and [L] are the concentrations of Cu ArM, Cu ArM azide adduct, and free azide, respectively. ΔA is the change in absorbance at the λ_{max} of the LMCT and ΔA_∞ is the absorbance change for complete formation of the 1:1 azide adduct. Equation 1 can be modified to give a double reciprocal plot:

$$\frac{1}{\Delta A} = \frac{1}{K\Delta A_\infty}\frac{1}{[L]} + \frac{1}{\Delta A_\infty} \qquad \text{Eq. 3-2}$$

Plotting $1/\Delta A$ versus $1/[L]$ should yield a straight line with a slope of $1/K\Delta A_\infty$ and x- and y-intercepts of $-K$ and $1/\Delta A_\infty$, respectively. Determining ΔA_∞ using this double reciprocal plot, the Hill equation can be used to confirm formation of 1:1 adducts:

$$\log\left[\frac{\Delta A}{(\Delta A_\infty - \Delta A)}\right] = n\log[L] + \log K \qquad \text{Eq. 3-3}$$

The slope of n = 1 for a plot of log $[\Delta A/(\Delta A_\infty - \Delta A)]$ versus log[L] indicates binding of a single azide ligand to the Cu center. Since the affinity for azide is low in these cases, it was assumed that the total azide concentration, $[L]_0$, is approximately equal to the free azide concentration ($[L]_0 \sim [L]$). The volume change in each solution was taken into account and the correlation coefficients for all lines fit in Excel were >0.99. Representative plots are shown in Figure 3-9 and the remaining plots are in Figure A-5 & 6.

The UV-vis features of the N_3^- to Cu^{II} LMCT, as well as the equilibrium constants (K) and n values for the Cu ArMs are summarized in Table 3-3. The Hill coefficients (n) were

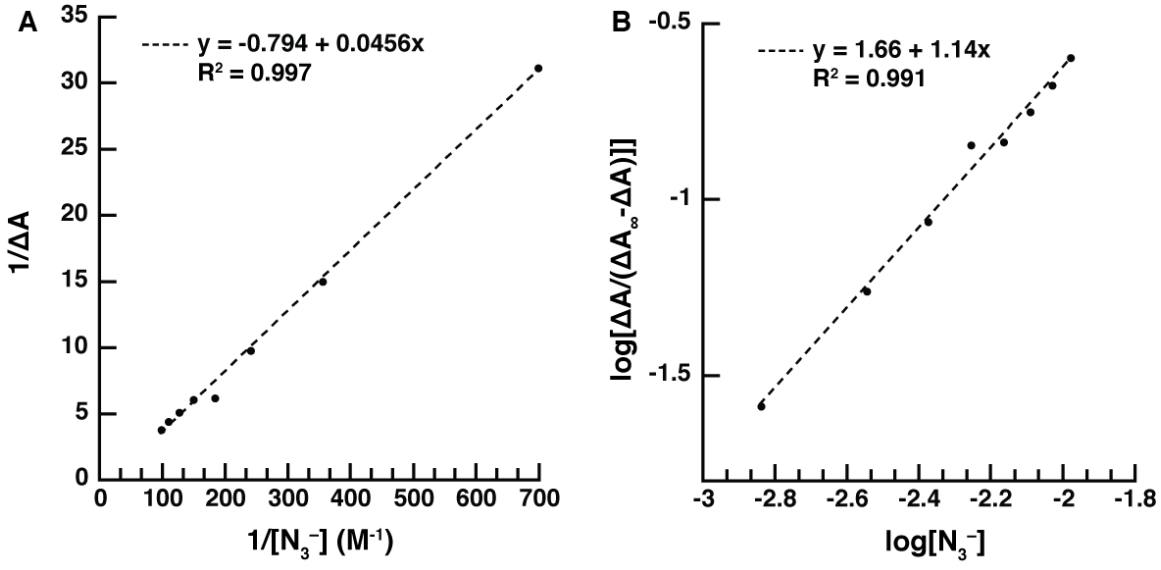

Figure 3-9. The double-reciprocal plot (**A**) and Hill equation plot (**B**) for **1a-N₃**.

sufficiently close to 1 to assume formation of 1:1 Cu-N_3 adducts. All titrations were performed in triplicate. The extinction coefficients in Table 3-2 are the extrapolated values calculated from ΔA_∞ from the double reciprocal plot. The optical activity of the LMCT band by CD was low, so numerical treatment of this titration data was unreliable. Instead, the spectra were measured with large excess of azide and those data are reported in Table 3-2.

*Crystallization of $[Cu^{II}(biot\text{-}pr\text{-}dpea)(OH_2)_2]^{2+}$⊂WT Sav***.** Apo-Sav protein crystals were obtained at 20°C within two days by sitting-drop vapor diffusion technique mixing 1.5 µL crystallization buffer (2.0 M ammonium sulfate, 0.1 M sodium acetate, pH 4.0) and 3.5 µL protein solution (26 mg/mL lyophilized protein in water). The droplet was equilibrated against a reservoir solution of 100 µL crystallization buffer. Subsequently, single crystals of Sav were soaked for 1 day at 20 °C in a soaking buffer, which was prepared by mixing 1 µL of a 10 mM stock solution of complex $[Cu^{II}(biot\text{-}pr\text{-}dpea(OH_2)Cl]Cl$ (in water with 100 mM $CuCl_2$), 9 µL crystallization buffer, and 0.5 µL of the original protein solution. After the soaking, crystals were transferred for 30 seconds into a cryo-protectant solution consisting of 30 % (v/v) glycerol in crystallization buffer. Next, crystals were shock-frozen in liquid nitrogen.

Crystallization of $[Cu^{II}(biot\text{-}n\text{-}dpea)(OH_2)N_3]^{2+}$⊂WT Sav. Single crystals of $[Cu^{II}(biot\text{-}n\text{-}dpea)(OH_2)_2]^{2+}$⊂WT Sav (n = et or pr) were prepared as described above. The crystals were transferred to a solution of 1.0 mM NaN_3 in cryo-protectant for 5 minutes causing the crystals to turn from blue to green. The crystals were then shock-frozen in liquid nitrogen.

Data Processing. X-ray diffraction data were collected at the Stanford Synchrotron Radiation Lightsource (BL 14-1 and 9-2) at a wavelength of 1 Å and processed with software XDS[50] and scaled with AIMLESS (CCP4 Suite)[51]. The structure was solved by molecular replacement

using program PHASER (CCP4 Suite)[51] and the structure 2QCB from the PDB as input model with ligand and water molecules removed. For structure refinement REFMAC5 (CCP4 Suite)[52] and PHENIX.REFINE[53] were used. Cu-complex manipulation was carried out with programs REEL and COOT using the Cu-complex coordinates of PDB structures 5K49 and 5K67 for ethyl and propyl linkers, respectively.[28] For water picking, electron density, and structure visualization, the software COOT[54] was used. Figures were drawn with PyMOL (the PyMOL Molecular Graphics System, Version 1.5.0.5, Schrödinger, LLC). Crystallographic details, processing and refinement statistics are given in Tables 4-4 and 4-5.

Overall Structures. Apo-crystals of proteins WT Sav soaked with Cu-complexes [Cu^{II}(biot-n-dpea(OH_2)Cl]Cl (n = et or pr) constituted space group $I4_122$ with virtually identical unit cell parameters (Table 4-4). A single Sav monomer was obtained per asymmetric unit after molecular replacement. Protein residues 2-11 and 135-159 of the N- and C-terminus, respectively, were not resolved in the electron density, presumably due to disorder. Starting from the Sav monomer, the biological homotetramer is generated by application of crystallographic C2-symmetry axes along the x-, y- and z-axes of the unit cell. The overall protein structures are virtually identical to structure biotin⊂WT Sav (PDB 1STP, see Table 4-4).

General Complex Modeling. For all structures of apo-protein crystals soaked with the corresponding Cu-complexes, the following general observations were made: i) residual electron density in the F_o-F_c map was observed in the biotin binding pocket and in the biotin vestibule, which is flanked by protein residues of loop-3,4^A (the superscript number indicates Sav monomer within tetramer) loop-4,5^C, loop-5,6^A loop-7,8^A and loop-7,8^B, and iii) an anomalous dispersion density map indicated a significant peak in the vestibule

superimposed with the electron density peak (Figs. 3-3 and 3-10). The residual electron density was fit with the corresponding Cu-complexes which projected Cu to the position of the strong anomalous density peak.

Structure Refinement of 1a-N_3. The complex $[Cu^{II}(biot\text{-}et\text{-}dpea)N_3]^+$ was modeled with 100 % occupancy. The overall geometry of the Cu complex is similar to the previously published structure of **1a**.[28] The coordinating pyridine nitrogen atoms of the dpea ligand were modeled as the axial ligands of a trigonal bipyramidal Cu-complex (Figure 3-3, Tables 3-1 and 3-5). However, in contrast to (**1a**), the aquo ligand pointing towards the biotin binding site is replaced by a stick-like density that was modeled as an azide ion. Only very weak electron density (< 3 σ) was observed in an F_o-F_c omit map in the third position of the trigonal plane suggesting that a water ligand in this position binds transiently. One of the two pyridine rings (containing N3, N3 hereafter) of dpea is nestled within loop-7,8^A residues S112^A, T114^A, K121^A, L124^A and five water molecules (w66, w72, w136, 176, and w175^B) that form an H-bonding network. The second pyridine of dpea (containing N2, N2 hereafter) is in close proximity to loop-3,4^A and loop-7,8^B residues side chains N49^A and K121^B, as well as a glycerol molecule. The azido ligand is involved in H-bonds with N49^A and O1 (w66). The coordinated azido ligand is located near loop-5,6^C near side chain N49^A and O1 (w66). The Cu⋯Cu distance between two symmetry-related complexes is 11.3 Å (Figs 3-11). A free Cu ion was found near H87 from the crystal soaking condition and was modeled with 20% occupancy.

Structure refinement of complex 1b. In structure $[Cu^{II}(biot\text{-}pr\text{-}dpea(OH_2)]^{2+}$⊂Sav WT (**1b**) the copper complex is fully occupied. The copper complex was modeled in a trigonal bipyramidal geometry (Fig. 3-1B and 3-10A), Tables 3-1 and 3-5). This is in stark contrast to the trigonal

monopyramidal geometry of the corresponding complex [Cu^{II}(biot-pr-dpea)]$^{+}$⊂Sav S112C which was published earlier.[28] The nitrogens of the two pyridine rings are coordinated in the axial positions, the dpea tertiary amine and one aquo ligand are positioned in the trigonal equatorial plane. The aquo ligand points away from the neighboring Sav monomer. The Cu–O_{aquo} bond length is 2.3 Å. Only weak electron density (< 3 σ) was found in an F_o-F_c complex omit map in the remaining position within the trigonal plane that is facing towards the neighboring Sav monomer. This suggests transient binding of an aqua ligand in this position. Occupation of this position seems to be sterically hindered by the proximity of the pyridine ring of the symmetry-related Cu-complex from the neighboring Sav monomer (Figure 3-12). Note that two symmetry-related Cu-complex pyridine rings form a π-stacking interaction that presumably stabilizes the complex conformation. Two neighboring Cu-complexes have a Cu---Cu distance of 7.2 Å. The conformation of the two symmetry-related complexes are further stabilized by hydrophobic interactions with residues $L110^{A}$, $L110^{B}$, $K121^{A}$, $K121^{B}$, $L124^{A}$ and $L124^{B}$. An extended H-bonding network including several water molecules is connecting the aquo ligand of the Cu-complex with residues in loops 3,4, 5,6 and 7,8 (Fig. 3-1B). A free Cu ion was found near H87 from the crystal soaking condition and was modeled with 50% occupancy.

Structure refinement of complex 1b-N_3. Except for the azide ligand the structure of complex [Cu^{II}(biot-pr-dpea(OH_2)N_3]$^{+}$ ⊂ Sav (**1b-N_3**) is virtually identical to the structure of complex **2** (Fig. 3-6 & 13). The fourth ligand in the equatorial plane is occupied by an azide ligand. Due to the proximity of the symmetry-related Cu-complex pyridine, the azide is slightly tilted out of the square plane (angle O_{aquo}–Cu–N_{azide} = 148°). The azide ion was modelled with 50% occupancy, attributed to this steric interaction. The Cu–N_{azide} bond length is 1.9 Å. The distal

azide nitrogen (N6) forms an H-bond with N_ζ of K121. A free Cu ion was found near H87 from the crystal soaking condition and was modeled with 50% occupancy.

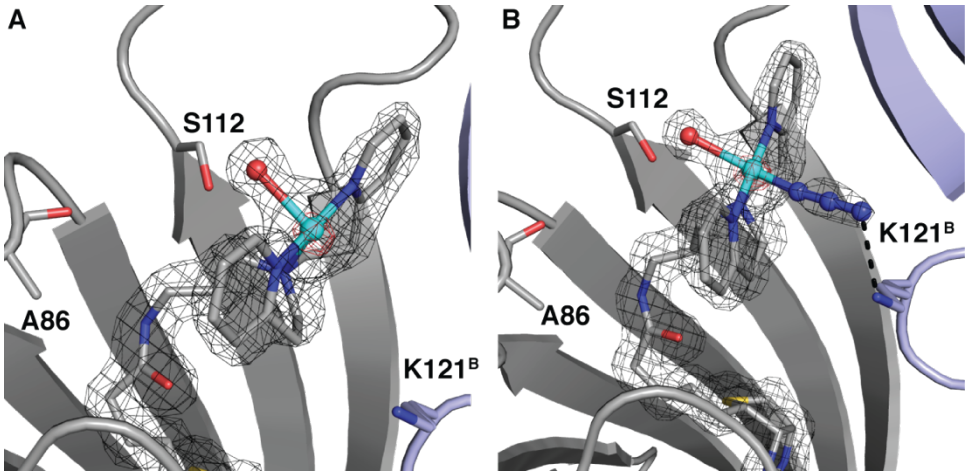

Figure 3-10. Structures of **1b** (**A**) and **1b-N_3** (**B**) with cofactor positions indicated by $2F_o$-F_c electron density (black mesh, contoured at 1σ) and anomalous difference density (red mesh, contoured at 7σ). Copper ions are colored in cyan, oxygen atoms/water molecules are colored in red, and nitrogen atoms are colored in blue. H-bonding interactions are shown as dashed lines. $K121^B$ from the adjacent subunit shown in light blue.

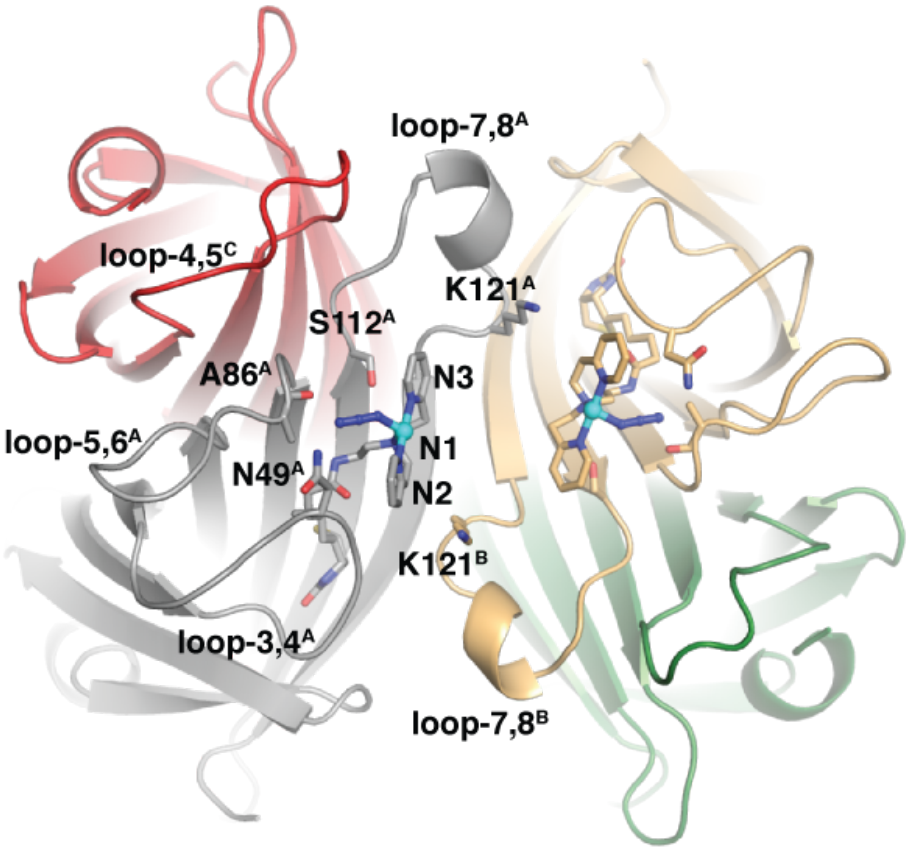

Figure 3-11. Tetrameric view of **1a-N$_3$** shown as a cartoon. Subunit A is in grey, subunit B is in tan, subunit C is in red, and subunit D is in green.

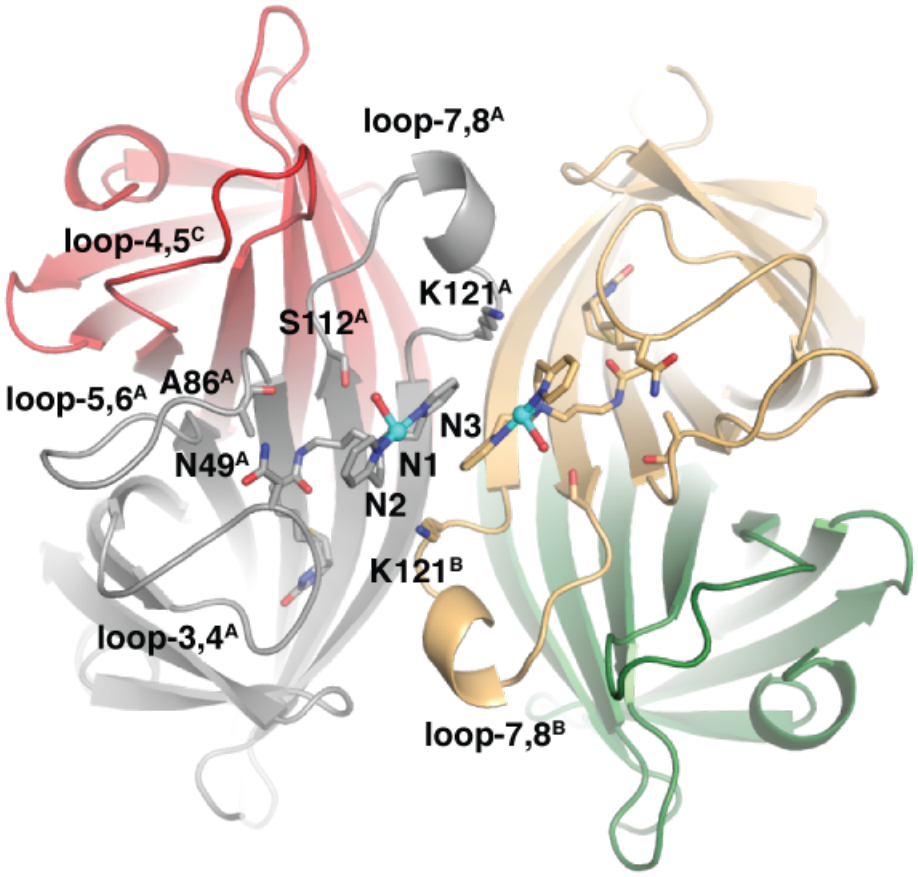

Figure 3-12. Tetrameric view of **1b** shown as a cartoon. Subunit A is in grey, subunit B is in tan, subunit C is in red, and subunit D is in green.

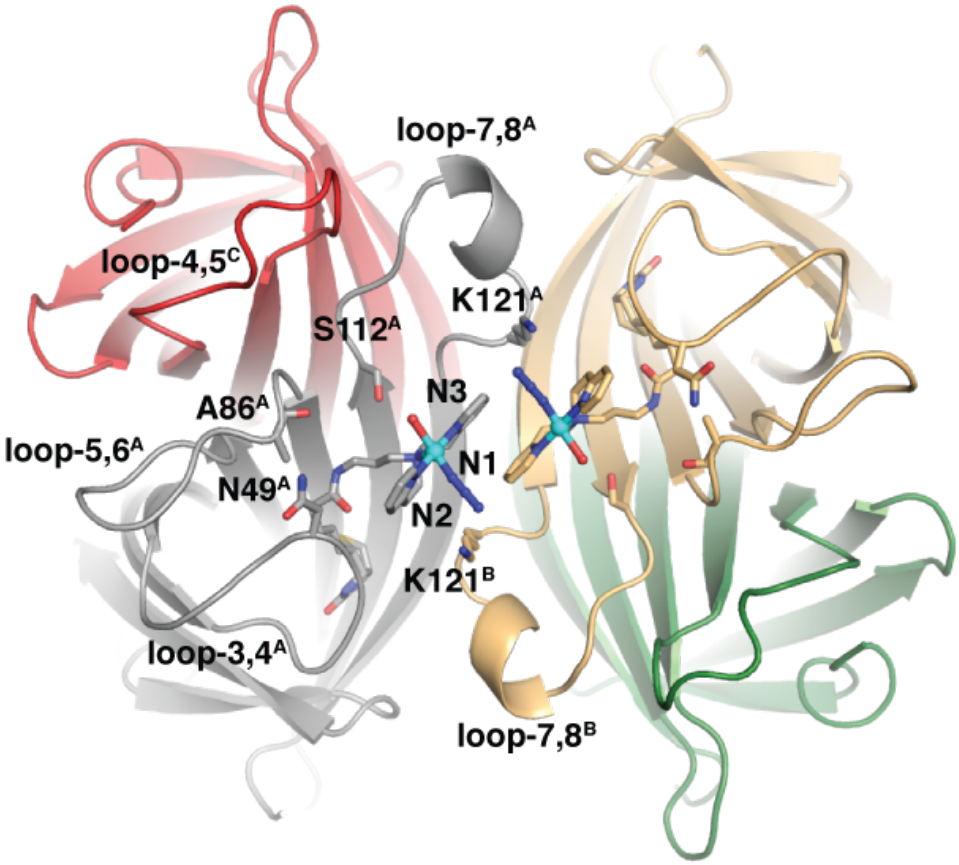

Figure 3-13. Tetrameric view of **1b-N_3** shown as a cartoon. Subunit A is in grey, subunit B is in tan, subunit C is in red, and subunit D is in green.

Table 3-4. X-ray Crystallographic Data Processing and Refinement Statistics

Sav Mutant	WT	WT	WT
Cu complex	$[Cu^{II}$(biot-pr-dpea)$(OH_2)]^{2+}$ (**1b**)	$[Cu^{II}$(biot-pr-dpea)$(OH_2)N_3]^{+}$ (**1b-N_3**)	$[Cu^{II}$(biot-et-dpea)$(OH_2)N_3]^{+}$ (**1a-N_3**)
PDB code	5VL8	5VL5	5VKX
Cu complex PDB 3-letter code	S32	S31	S18
Data Processing			
Unit Cell	a, b, c = 57.6 Å, 57.6 Å, 183.6 Å; α, β, γ = 90°	a, b, c = 57.7 Å, 57.7 Å, 183.6 Å; α, β, γ = 90°	a, b, c = 57.9 Å, 57.9 Å, 184.4 Å; α, β, γ = 90°
Space group	$I4_122$	$I4_122$	$I4_122$
Resolution (Å)	54.9 – 1.70	55.1 – 1.46	37.4 – 1.37
Highest resolution shell (Å)	1.73 - 1.70	1.49 – 1.46	1.40 – 1.37
R_{merge} (%)	12.7 (129.3)	18.8 (148.3)	4.9 (96.2)
No. of unique reflections	17570 (904)	27425 (1349)	33187 (1457)
Multiplicity	8.7 (6.1)	8.1 (7.6)	11.1 (7.7)
I/sig(I)	9.3 (1.0)	3.9 (0.5)	22.2 (1.4)
Completeness	100 (100)	100 (100)	99.5 (90.8)
CC(1/2)	0.997 (0.27)	0.99 (0.62)	1.00 (0.74)
Structure Refinement			
R_{work}	0.18	0.23	0.16
R_{free}	0.21	0.26	0.19
Rmsd bond length (Å)	0.021	0.025	0.031
Rmsd bond angle (°)	3.431	3.242	2.874
Rmsd compared to biotin-SAV WT (PDB 1STP) (Å)	0.71	0.70	0.73
No ligands Cu complex Water Glycerol Cu(B)	 1 146 1 1	 1 152 - 1	 1 178 1 1

Table 3-5. Summary of Structural Details

PDB code	5VL8	5VL5	5VKX
Complex	**1b**	**1b-N_3**	**1a-N_3**
Electron density at Cu in F_o-F_c omit map (σ)	21	20	28
Anomalous dispersion density at Cu (σ)	15	11	26
Geometry of Cu complex	Trigonal bipyramidal[a]	Distorted square pyramidal	Trigonal bipyramidal[a]
Coordination number of Cu complex	5[a]	5	5 [a]
Occupancy of Cu complex (%)	100	100	100
B-factor (Å^2) Overall protein Loop 7,8 Loop 3,4 Cu complex DPEA Cu N_3^-	 25.5 25.3 25.0 29.8 29.5 36.0 –	 23.0 22.7 23.6 28.4 27.7 34.4 32.6	 20.6 20.0 20.3 26.5 24.8 32.3 44.6
Distance Cu-Cu (Å)	7.2	7.3	11.3

[a]Aquo ligand in equatorial plane was only weakly visible (< 3 σ) in electron density of F_0-F_c omit map.

References

(1) Shook, R. L.; Borovik, A. S. Role of the Secondary Coordination Sphere in Metal-Mediated Dioxygen Activation. *Inorg. Chem.* **2010**, *49* (8), 3646–3660.

(2) Shook, R. L.; Borovik, A. S. The Effects of Hydrogen Bonds on Metal-Mediated O_2 Activation and Related Processes. *Chem. Commun.* **2008**, No. 46, 6095.

(3) Cook, S. A.; Borovik, A. S. Molecular Designs for Controlling the Local Environments around Metal Ions. *Acc. Chem. Res.* **2015**, *48* (8), 2407–2414.

(4) Cook, S. A.; Hill, E. A.; Borovik, A. S. Lessons from Nature: A Bio-Inspired Approach to Molecular Design. *Biochemistry* **2015**, *54* (27), 4167–4180.

(5) Dawson, J. H. Probing Structure-Function Relations in Heme-Containing Oxygenases and Peroxidases. *Science* **1988**, *240* (4851), 433–439.

(6) Lu, Y.; Valentine, J. S. Engineering Metal-Binding Sites in Proteins. *Curr. Opin. Struct. Biol.* **1997**, *7* (4), 495–500.

(7) Paoli, M.; Liddington, R.; Tame, J.; Wilkinson, A.; Dodson, G. Crystal Structure of T State Haemoglobin with Oxygen Bound At All Four Haems. *J. Mol. Biol.* **1996**, *256* (4), 775–

792.
(8) Wuenschell, G. E.; Tetreau, C.; Lavalette, D.; Reed, C. A. H-Bonded Oxyhemoglobin Models with Substituted Picket-Fence Porphyrins - the Model-Compound Equivalent of Site-Directed Mutagenesis. *J. Am. Chem. Soc.* **1992**, *114* (9), 3346–3355.
(9) Natale, D.; Mareque-Rivas, J. C. The Combination of Transition Metal Ions and Hydrogen-Bonding Interactions. *Chem. Commun.* **2008**, No. 4, 425–437.
(10) Wada, A.; Honda, Y.; Yamaguchi, S.; Nagatomo, S.; Kitagawa, T.; Jitsukawa, K.; Masuda, H. Steric and Hydrogen-Bonding Effects on the Stability of Copper Complexes with Small Molecules. *Inorg. Chem.* **2004**, *43* (18), 5725–5735.
(11) Maglio, O.; Nastri, F.; Calhoun, J. R.; Lahr, S.; Wade, H.; Pavone, V.; DeGrado, W. F.; Lombardi, A. Artificial Di-Iron Proteins: Solution Characterization of Four Helix Bundles Containing Two Distinct Types of Inter-Helical Loops. *J. Biol. Inorg. Chem.* **2005**, *10* (5), 539–549.
(12) DeGrado, W. F.; Summa, C. M.; Pavone, V.; Nastri, F.; Lombardi, A. De Novo Design and Structural Characterization of Proteins and Metalloproteins. *Annu. Rev. Biochem.* **1999**, *68* (1), 779–819.
(13) Summa, C. M.; Lombardi, A.; Lewis, M.; DeGrado, W. F. Tertiary Templates for the Design of Diiron Proteins. *Curr. Opin. Struct. Biol.* **1999**, *9* (4), 500–508.
(14) Yu, F.; Cangelosi, V. M.; Zastrow, M. L.; Tegoni, M.; Plegaria, J. S.; Tebo, A. G.; Mocny, C. S.; Ruckthong, L.; Qayyum, H.; Pecoraro, V. L. Protein Design: Toward Functional Metalloenzymes. *Chem. Rev.* **2014**, *114* (7), 3495–3578.
(15) Tebo, A. G.; Pecoraro, V. L. Artificial Metalloenzymes Derived from Three-Helix Bundles. *Curr. Opin. Chem. Biol.* **2015**, *25*, 65–70.
(16) Lu, Y. Metalloprotein and Metallo-DNA/RNAzyme Design: Current Approaches, Success Measures, and Future Challenges. *Inorg. Chem.* **2006**, *45* (25), 9930–9940.
(17) Lu, Y. Biosynthetic Inorganic Chemistry. *Angew. Chem., Int. Ed. Engl.* **2006**, *45* (34), 5588–5601.
(18) Berggren, G.; Adamska, A.; Lambertz, C.; Simmons, T. R.; Esselborn, J.; Atta, M.; Gambarelli, S.; Mouesca, J. M.; Reijerse, E.; Lubitz, W.; Happe, T.; Artero, V.; Fontecave, M. Biomimetic Assembly and Activation of [FeFe]-Hydrogenases. *Nature* **2013**, *498* (7456), 66–69.
(19) Cavazza, C.; Bochot, C.; Rousselot-Pailley, P.; Carpentier, P.; Cherrier, M. V; Martin, L.; Marchi-Delapierre, C.; Fontecilla-Camps, J. C.; Ménage, S. Crystallographic Snapshots of the Reaction of Aromatic C-H with O_2 Catalysed by a Protein-Bound Iron Complex. *Nat. Chem.* **2010**, *2* (12), 1069–1076.
(20) Ueno, T.; Abe, S.; Yokoi, N.; Watanabe, Y. Coordination Design of Artificial Metalloproteins Utilizing Protein Vacant Space. *Coord. Chem. Rev.* **2007**, *251* (21–24), 2717–2731.
(21) Lu, Y.; Yeung, N.; Sieracki, N.; Marshall, N. M. Design of Functional Metalloproteins. *Nature* **2009**, *460* (7257), 855–862.
(22) Heinisch, T.; Ward, T. R. Artificial Metalloenzymes Based on the Biotin-Streptavidin Technology: Challenges and Opportunities. *Acc. Chem. Res.* **2016**, *49* (9), 1711–1721.
(23) Dürrenberger, M.; Ward, T. R. Recent Achievments in the Design and Engineering of Artificial Metalloenzymes. *Curr. Opin. Chem. Biol.* **2014**, *19*, 99–106.
(24) Heinisch, T.; Ward, T. R. Design Strategies for the Creation of Artificial Metalloenzymes. *Curr. Opin. Chem. Biol.* **2010**, *14* (2), 184–199.

(25) Lewis, J. C. Artificial Metalloenzymes and Metallopeptide Catalysts for Organic Synthesis. *ACS Catal.* **2013**, *3* (12), 2954–2975.
(26) McIntosh, J. A.; Farwell, C. C.; Arnold, F. H. Expanding P450 Catalytic Reaction Space through Evolution and Engineering. *Curr. Opin. Chem. Biol.* **2014**, *19*, 126–134.
(27) Wilson, M. E.; Whitesides, G. M. Conversion of a Protein to a Homogeneous Asymmetric Hydrogenation Catalyst by Site-Specific Modification with a diphosphinerhodium(I) Moiety. *J. Am. Chem. Soc.* **1978**, *100* (1), 306–307.
(28) Mann, S. I.; Heinisch, T.; Weitz, A. C.; Hendrich, M. P.; Ward, T. R.; Borovik, A. S. Modular Artificial Cupredoxins. *J. Am. Chem. Soc.* **2016**, *138* (29), 9073–9076.
(29) Addison, A. W.; Rao, T. N.; Reedijk, J.; van Rijn, J.; Verschoor, G. C. Synthesis, Structure, and Spectroscopic Properties of copper(II) Compounds Containing Nitrogen–sulphur Donor Ligands; the Crystal and Molecular Structure of aqua[1,7-bis(N-Methylbenzimidazol-2′-Yl)-2,6-dithiaheptane]copper(II) Perchlorate. *J. Chem. Soc., Dalt. Trans.* **1984**, No. 7, 1349–1356.
(30) Pate, J. E.; Ross, P. K.; Thamann, T. J.; Reed, C. A.; Karlin, K. D.; Sorrell, T. N.; Solomon, E. I. Spectroscopic Studies of the Charge Transfer and Vibrational Features of Binuclear copper(II) Azide Complexes: Comparison to the Coupled Binuclear Copper Active Site in Met Azide Hemocyanin and Tyrosinase. *J. Am. Chem. Soc.* **1989**, *111* (14), 5198–5209.
(31) Karlin, K. D.; Cohen, B. I.; Hayes, J. C.; Farooq, A.; Zubieta, J. Models for Methemocyanin Derivatives: Structural and Spectroscopic Comparisons of Related Azido-Coordinated (N3-) Mono-and Dinuclear Copper (II) Complexes. *Inorg. Chem.* **1987**, *26* (1), 147–153.
(32) Casella, L.; Gullotti, M.; Pallanza, G.; Buga, M. Binding of Azide and Thiocyanate Ligands to copper(II) Model Complexes. *Biol. Met.* **1990**, *3* (2), 137–140.
(33) Casella, L.; Gullotti, M.; Pallanza, G.; Buga, M. Spectroscopic and Binding Studies of Azide-Copper (II) Model Complexes. *Inorg. Chem.* **1991**, *30* (2), 221–227.
(34) Lee, D. H.; Murthy, N. N.; Karlin, K. D. Binuclear Copper Complexes Based on the 6, 6'-bis [[Bis (2-Pyridylmethyl) Amino] Methyl]-2, 2'-bipyridine Ligand. *Inorg. Chem.* **1997**, *36* (25), 5785–5792.
(35) Byers, W.; Curzon, G.; Garbett, K.; Speyer, B. E.; Young, S. N.; Williams, R. J. Anion-Binding and the State of Copper in Caeruloplasmin. *Biochim. Biophys. Acta* **1973**, *310* (1), 38–50.
(36) Casella, L.; Carugo, O.; Gullotti, M.; Garofani, S.; Zanello, P. Hemocyanin and Tyrosinase Models. Synthesis, Azide Binding, and Electrochemistry of Dinuclear Copper(II) Complexes with Poly(benzimidazole) Ligands Modeling the Met Forms of the Proteins. *Inorg. Chem.* **1993**, *32* (10), 2056–2067.
(37) Messerschmidt, A.; Luecke, H.; Huber, R. X-Ray Structures and Mechanistic Implications of Three Functional Derivatives of Ascorbate Oxidase from Zucchini. *J. Mol. Biol.* **1993**, *230* (3), 997–1014.
(38) Tsai, L. C.; Bonander, N.; Harata, K.; Karlsson, G.; Vänngård, T.; Langer, V.; Sjölin, L. Mutant Met121Ala of Pseudomonas Aeruginosa Azurin and Its Azide Derivative: Crystal Structures and Spectral Properties. *Acta Crystallogr. D. Biol. Crystallogr.* **1996**, *52* (Pt 5), 950–958.
(39) Zaitsev, V. N.; Zaitseva, I.; Papiz, M.; Lindley, P. F. An X-Ray Crystallographic Study of the Binding Sites of the Azide Inhibitor and Organic Substrates to Ceruloplasmin, a Multi-Copper Oxidase in the Plasma. *J. Biol. Inorg. Chem.* **1999**, *4* (5), 579–587.

(40) Tocheva, E. I.; Eltis, L. D.; Murphy, M. E. P. Conserved Active Site Residues Limit Inhibition of a Copper-Containing Nitrite Reductase by Small Molecules. *Biochemistry* **2008**, *47* (15), 4452–4460.
(41) Chufan, E. E.; Prigge, S. T.; Siebert, X.; Eipper, B. A.; Mains, R. E.; Amzel, L. M. Differential Reactivity between Two Copper Sites in Peptidylglycine Alpha-Hydroxylating Monooxygenase. *J. Am. Chem. Soc.* **2010**, *132* (44), 15565–15572.
(42) Hemsworth, G. R.; Taylor, E. J.; Kim, R. Q.; Gregory, R. C.; Lewis, S. J.; Turkenburg, J. P.; Parkin, A.; Davies, G. J.; Walton, P. H. The Copper Active Site of CBM33 Polysaccharide Oxygenases. *J. Am. Chem. Soc.* **2013**, *135* (16), 6069–6077.
(43) Hemsworth, G. R.; Henrissat, B.; Davies, G. J.; Walton, P. H. Discovery and Characterization of a New Family of Lytic Polysaccharide Monooxygenases. *Nat. Chem. Biol.* **2014**, *10* (2), 122–126.
(44) Lo Leggio, L.; Simmons, T. J.; Poulsen, J.-C. N.; Frandsen, K. E. H.; Hemsworth, G. R.; Stringer, M. A.; von Freiesleben, P.; Tovborg, M.; Johansen, K. S.; De Maria, L.; Harris, P. V; Soong, C.-L.; Dupree, P.; Tryfona, T.; Lenfant, N.; Henrissat, B.; Davies, G. J.; Walton, P. H. Structure and Boosting Activity of a Starch-Degrading Lytic Polysaccharide Monooxygenase. *Nat. Commun.* **2015**, *6*, 1–9.
(45) Rahaman, S. H.; Ghosh, R.; Lu, T.-H.; Ghosh, B. K. Chelating N,N′-(Bis(pyridin-2-Yl)alkylidene)propane-1,3-Diamine Pseudohalide copper(II) and cadmium(II) Coordination Compounds: Synthesis, Structure and Luminescence Properties of [M(bpap)(X)]ClO_4 and [M(bpap)$(X)_2$] [M=Cu, Cd; , NCS−]. *Polyhedron* **2005**, *24* (12), 1525–1532.
(46) Freitag, S.; Le Trong, I.; Klumb, L.; Stayton, P. S.; Stenkamp, R. E.; Trong, I. Le; Klumb, L.; Stayton, P. S.; Freitag, S. Structural Studies of the Streptavidin Binding Loop. *Protein Sci.* **1997**, *6* (6), 1157–1166.
(47) Dürrenberger, M.; Heinisch, T.; Wilson, Y. M.; Rossel, T.; Nogueira, E.; Knörr, L.; Mutschler, A.; Kersten, K.; Zimbron, M. J.; Pierron, J.; Schirmer, T.; Ward, T. R. Artificial Transfer Hydrogenases for the Enantioselective Reduction of Cyclic Imines. *Angew. Chem. Int. Ed..* **2011**, *50* (13), 3026–3029.
(48) Pangborn, A. B.; Giardello, M. A.; Grubbs, R. H.; Rosen, R. K.; Timmers, F. J. Safe and Convenient Procedure for Solvent Purification. *Organometallics* **1996**, *15*, 1518–1520.
(49) Petasis, D. T.; Hendrich, M. P. Quantitative Interpretation of Multifrequency Multimode EPR Spectra of Metal Containing Proteins, Enzymes, and Biomimetic Complexes. *Methods Enzymol.* **2015**, *563*, 171–208.
(50) Kabsch, W. XDS. *Acta Crystallogr. D. Biol. Crystallogr.* **2010**, *66* (2), 125–132.
(51) Evans, P. R. An Introduction to Data Reduction: Space-Group Determination, Scaling and Intensity Statistics. *Acta Crystallogr. Sect. D Biol. Crystallogr.* **2011**, *67* (4), 282–292.
(52) Murshudov, G. N.; Vagin, A. A.; Dodson, E. J. Refinement of Macromolecular Structures by the Maximum-Likelihood Method. *Acta Crystallogr. D. Biol. Crystallogr.* **1997**, *53* (3), 240–255.
(53) Adams, P. D.; Afonine, P. V; Bunkóczi, G.; Chen, V. B.; Davis, I. W.; Echols, N.; Headd, J. J.; Hung, L.-W.; Kapral, G. J.; Grosse-Kunstleve, R. W.; McCoy, A. J.; Moriarty, N. W.; Oeffner, R.; Read, R. J.; Richardson, D. C.; Richardson, J. S.; Terwilliger, T. C.; Zwart, P. H. PHENIX: A Comprehensive Python-Based System for Macromolecular Structure Solution. *Acta Crystallogr. D. Biol. Crystallogr.* **2010**, *66* (2), 213–221.

(54) Emsley, P.; Cowtan, K. Coot: Model-Building Tools for Molecular Graphics. *Acta Crystallogr. D. Biol. Crystallogr.* **2004**, *60* (Pt 12 Pt 1), 2126–2132.

CHAPTER 4

Peroxide Activation Regulated by Hydrogen Bonds within Artificial Cu Proteins

Introduction

The utilization of dioxygen in biology is critical for most forms of life and is often achieved using metalloenzymes that perform essential transformations in metabolic processes, mammalian physiology, and biodegradation processes. A subset of these enzymes contain mononuclear Cu centers within their active sites, these include dopamine β-monooxygenase (DβM),[1,2] peptidylglycine α-hydroxylating monooxygenase (PHM),[1,3–5] and amine oxidase.[6] Another family of Cu-containing metalloenzymes that has received recent interest in the area of biofuel production are lytic polysaccharide monooxygenases (LPMOs), such as AA9.[7–12] These metalloenzymes have a mononuclear Cu center in their active site that can oxidize the strong C–H bonds of cellulose and chitin (Fig. 4-1). The mechanistic details for many of these oxidative processes are still uncertain and questions remain about the identity of the key dioxygen adducts. Possible candidates include $Cu^{II}–O_2^-$ (superoxido) and Cu^{II}–OOH (hydroperoxido), however the structures of these species are often inferred

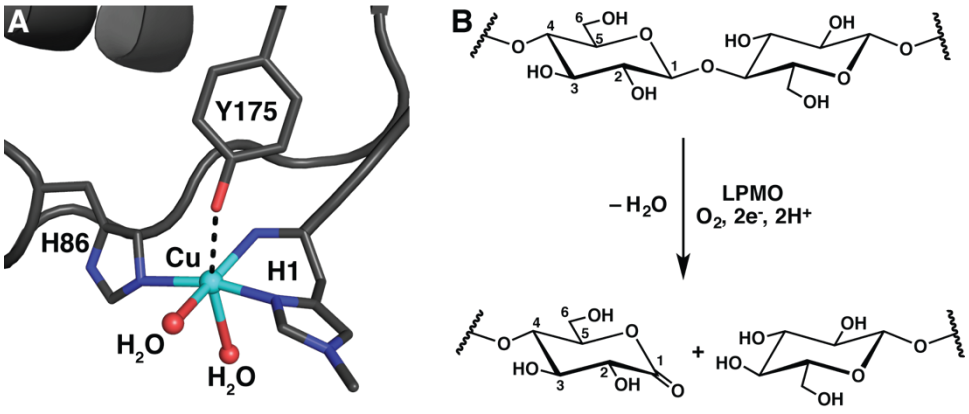

Figure 4-1. Resting state structure of LPMO AA9 with a proximal tyrosine residue (PDB: 2YET) (**A**) and a typical reaction catalyzed by LPMOs (C1 oxidation) (**B**). in A, the tyrosine–Cu interaction has a Cu–O distance of 1.8 Å and is shown as a dashed line.

because they are inherently unstable at room temperature.

The activation of dioxygen at metallo-active sites is regulated by structural properties provided by the protein matrix and it is difficult to design model systems that incorporate these features. Even though the site architectures of monoxygenases are diverse, they share the common characteristic that non-covalent interactions, especially hydrogen bonds (H-bonds), control metal-mediated O_2 activation.[13–24] For instance, the specific H-bonding interactions found in P450s and hemoglobin (Hb) that were discussed in Chapter 1 control the stability and function of Fe–OO(H) species (Fig. 4-2A & B).[25–35]

In many copper-containing metalloenzymes, such as DβM and LPMOs, Cu^{II}–OOH species are proposed intermediates along the catalytic pathway. Enzymatic studies on DβM have proposed that an H-bond to the distal O-atom of the Cu^{II}–OOH species assists in cleavage of the O–O bond.[36,37] Recently, a structural study by Marletta and coworkers on LPMO *Mt*PMO3* has suggested that H-bonds to the distal O-atom of a Cu^{II}–OOH species could be important in controlling function (Fig. 4-2C).[38] One challenge in exploring these systems is finding suitable model systems whose structure can accurately simulate the local

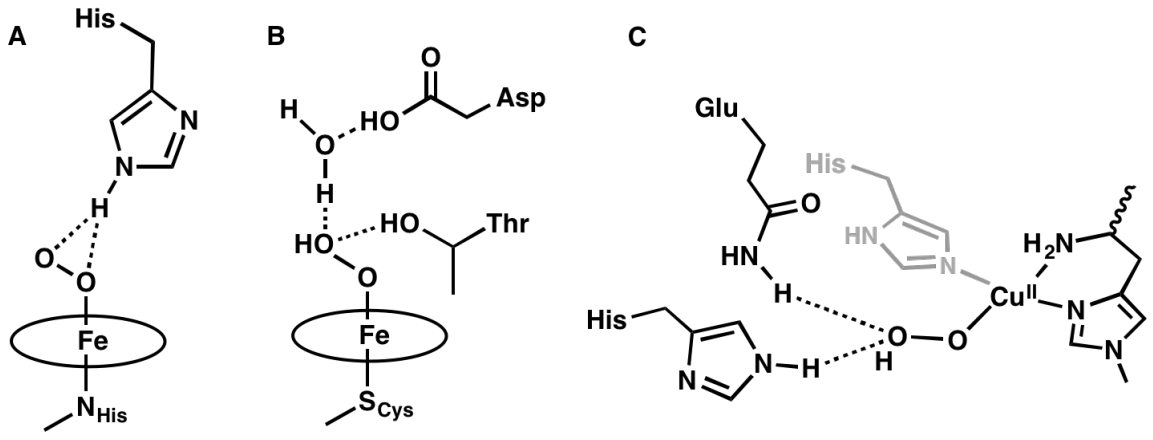

Figure 4-2. ChemDraw representations of the H-bonding networks in (**A**) oxy-Hb (PDB: 1GZX) and the proposed H-bonding interactions in (**B**) P450s and (**C**) LPMO *Mt*PMO3*. Circles represent protoporphyrin IX.

environment within a protein active site. Masuda has developed ligands bearing different H-bonding groups to examine the effects of H-bonds to the proximal or distal O-atoms of hydroperoxido ligands. In Chapter 1, Masuda's tripodal pivalamide-functionalized pyridine based ligand was shown to stabilize a Cu^{II}–OOH at room temperature and provide the only structurally characterized synthetic Cu^{II}–OOH species.[39] The thermal stability of this species was attributed to the intramolecular H-bonds provided by the pivalamide groups to the proximal O-atom of the hydroperoxido ligand (Fig. 4-3A). Karlin prepared a similar tripodal ligand with a benzylamine functionalized pyridine ring which formed a Cu^{II}–OOH complex at –90 ˚C with increased stability relative to ligands that did not contain H-bonding groups, again due to an H-bonding interaction with the proximal O-atom (Fig. 4-3B).[40] Masuda also

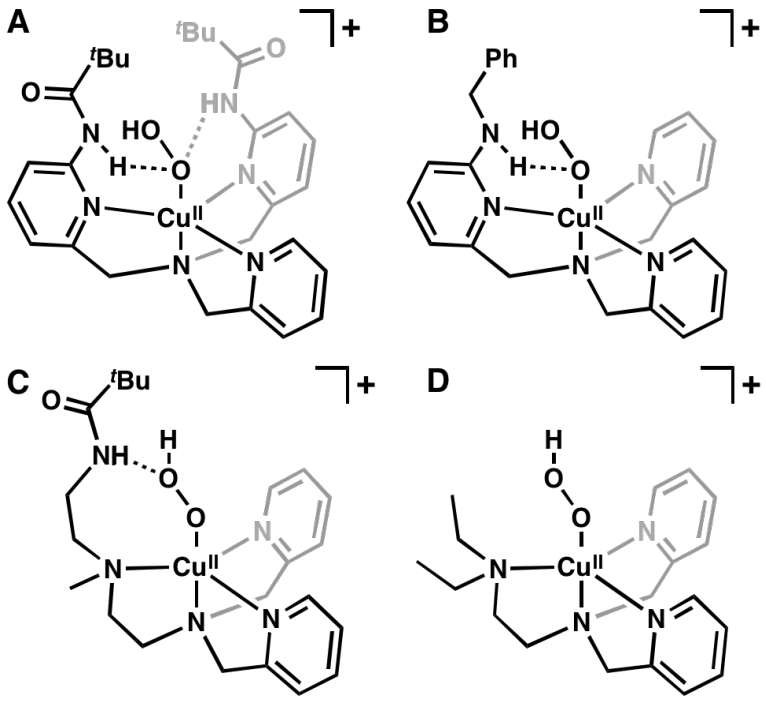

Figure 4-3. ChemDraw structures of Cu^{II}–OOH species with proposed intramolecular H-bonds. **A** and **B** show ligands that can donate H-bonds to the proximal O-atom of the hydroperoxido ligand. **C** and **D** compare Cu^{II}–OOH species with and without an H-bond to the distal O-atom of the OOH^- ligand. Note that **A** is the only structurally characterized species, in **B-D** H-bonds are inferred.

developed a ligand system designed to donate an H-bond to the distal O-atom of a hydroperoxido ligand. This study compared the stability of two Cu–OOH species, one with a H-bonding group and one without (Fig. 4-3C & D).[36] Masuda proposed that H-bonds to the proximal O-atom instill stability while H-bonds to the distal O-atom contribute to the activation of the hydroperoxido ligand, however there is no structural or spectroscopic evidence that the H-bond to the distal O-atom exists in this complex.

To further investigate the relationship between H-bonding interactions and Cu–hydroperoxido complexes, I utilized the H-bonding network provided by streptavidin (Sav) in the artificial metalloproteins (ArMs) discussed in Chapters 2 and 3. The ability to precisely engineer H-bonding interactions within Sav allowed for the preparation and stabilization of Cu^{II}–OOH species at ambient conditions in aqueous solution. *In crystallo* studies allowed for the identification of the H-bonding network within the local environment, allowing us to systematically modify each H-bond to pinpoint which interactions instilled stability or reactivity.

Results and Discussion

Solution Properties of $[Cu^{II}(biot\text{-}et\text{-}dpea)(H_2O)_2]^{2+}$. Initial studies performed with the biotinylated complex $[Cu^{II}(biot\text{-}et\text{-}dpea)(H_2O)_2]^{2+}$ showed that it reacts with H_2O_2 in 50 mM MES pH 6 at room temperature to form a new complex with spectroscopic features of a Cu^{II}–OOH species (Scheme 4-1). This new species has an absorption band at λ_{max} = 375 nm (ε = 1800 $M^{-1}cm^{-1}$) which is consistent with a hydroperoxido-to-Cu^{II} charge transfer transition (Fig. 4-4, Table 4-1).[36,40–46] The complex is unstable and decays with a half-life of 6 min. The decay of $[Cu^{II}(biot\text{-}et\text{-}dpea)(OOH)]^{+}$ is similar to that observed in other synthetic systems and is illustrative of the inherent instability of Cu^{II}–OOH species at room temperature.[47]

Scheme 4-1. Reaction Cu Complex and Cu ArMs with H_2O_2

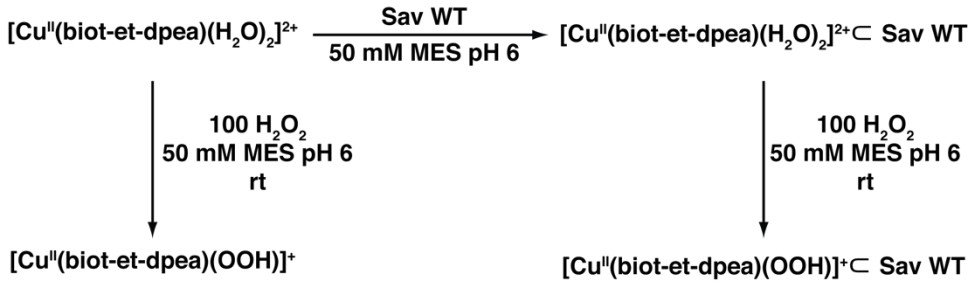

$[Cu^{II}(biot\text{-}et\text{-}dpea)(H_2O)_2]^{2+}$⊂Sav WT: Solution Properties. Confinement of this species within Sav produced a stable Cu^{II}–OOH species. The ArM $[Cu^{II}(biot\text{-}et\text{-}dpea)(H_2O)_2]^{2+}$⊂Sav WT (**1a**) was used for these studies which contains a five-coordinate Cu^{II} center with two coordinated water molecules. ArM **1a** and the azide-coordinated ArM **1a-N_3** unveiled two H-bonding networks that included aqua or azido ligands bound to the copper center. Chapter 3 also discussed the effect of these H-bonds on azide ligand binding. These results suggested that aqua ligand O2 can be displaced by an exogenous ligand, such as hydroperoxide. Treating **1a**

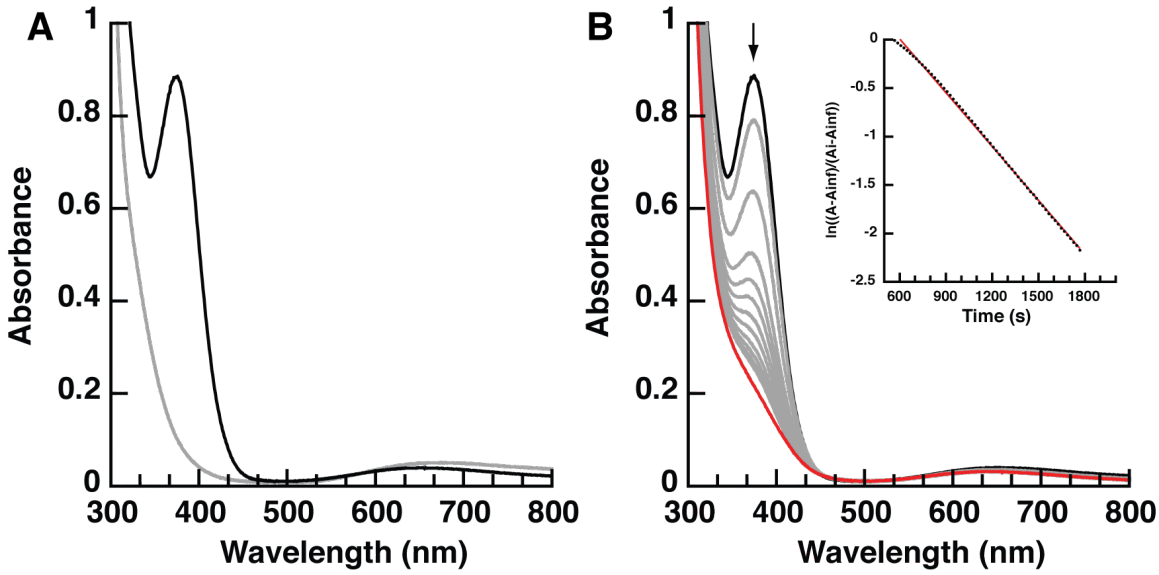

Figure 4-4. (**A**) UV-vis spectra of $[Cu^{II}(biot\text{-}et\text{-}dpea)(H_2O)_2]^{2+}$ before (grey) and after (black) reaction with H_2O_2 and (**B**) the decay of $[Cu^{II}(biot\text{-}et\text{-}dpea)(OOH)]^{+}$ with rate data used to calculate half-life (inset).

Table 4-1. UV-vis and EPR Spectroscopic Parameters for ArMs and Cu complexes

Host	WT		N49A		S112A		No Sav	
ArM	**1a**	**1a-OOH**	**3a**	**3a-OOH**	**4a**	**4a-OOH**	w/o H_2O_2	with H_2O_2
λ_{max},nm (ε_M)	625 (90)	370 (610) 480 (100) 615 (80)	630 (110)	375 (750) 480 (150) 620 (80)	615 (100)	375 (720) 480 (110) 600 (100)	670 (100)	373 (1500) 650 (80)
g	2.06 2.22 2.26	2.06 2.23 2.26	2.07 2.25	2.07 2.22 2.26	2.07 2.22 2.25	2.06 2.22 2.27	2.10 2.24	2.07 2.25
A, MHz	511 535	485 525	541	493 522	486 530	505 490	441	534

with excess H_2O_2 in 50 mM MES pH 6 produced changes in the absorption spectrum indicative of formation of the Cu^{II}–OOH species, $[Cu^{II}$(biot-et-dpea)(OOH)$]^+$⊂Sav WT (**1a-OOH**) (Scheme 4-1, Fig. 4-5, Table 4-1). Unlike $[Cu^{II}$(biot-et-dpea)(OOH)$]^+$, **1a-OOH** persisted in solution for over a day at room temperature, indicating that confinement within Sav WT increased the stability of the Cu^{II}–OOH adduct.

$[Cu^{II}$(biot-et-dpea)(OOH)$]^+$⊂Sav WT: Structure. **1a-OOH** was also prepared *in crystallo* by soaking single crystals of **1a** in cryoprotectant solution containing 1.0 mM H_2O_2 at pH 6 (see experimental section). The 1.50 Å structure of **1a-OOH** showed a four-coordinate copper complex with a distorted see-saw geometry (Fig. 4-6A & B, Table 4-2). Three coordination site are occupied by the N-atoms of the meridionally coordinated dpea ligand and the fourth site was modeled as a two-atom fragment assigned to an end-on hydroperoxido ligand with Cu–O2 and O2–O3 bond lengths of 1.93(1) and 1.54(1) and a Cu–O2–O3 bond angle of 143(1)°. Comparing the structures of **1a** and **1a-OOH** shows that the Cu(dpea) components of the complexes occupy the same position, but the aqua ligand O2 is replaced with a hydroperoxido ligand resulting in a decrease of the Cu–O2 bond length by nearly 0.6 Å

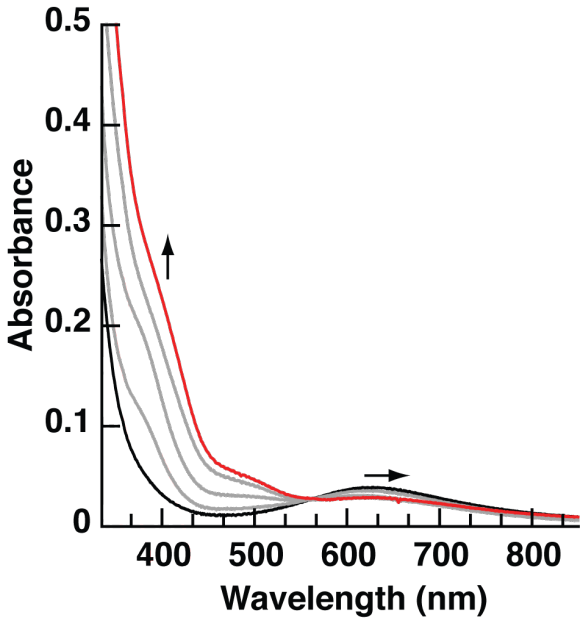

Figure 4-5. UV-vis spectrum of the reaction of **1a** (black) with H_2O_2 to make **1a-OOH** (red).

(Fig. 4-6C). These metrical parameters are similar to those reported by Masuda for the only structurally characterized synthetic Cu^{II}–OOH complex that was crystallized at low temperature: the Cu–N bond lengths are statistically the same, while the Cu–O2 and O2–O3 bond lengths are slightly longer.[41] Additionally, the O–O bond length in **1a-OOH** is similar to those found in the structures of LPMOs whose Cu^{II} active sites are proposed to also contain

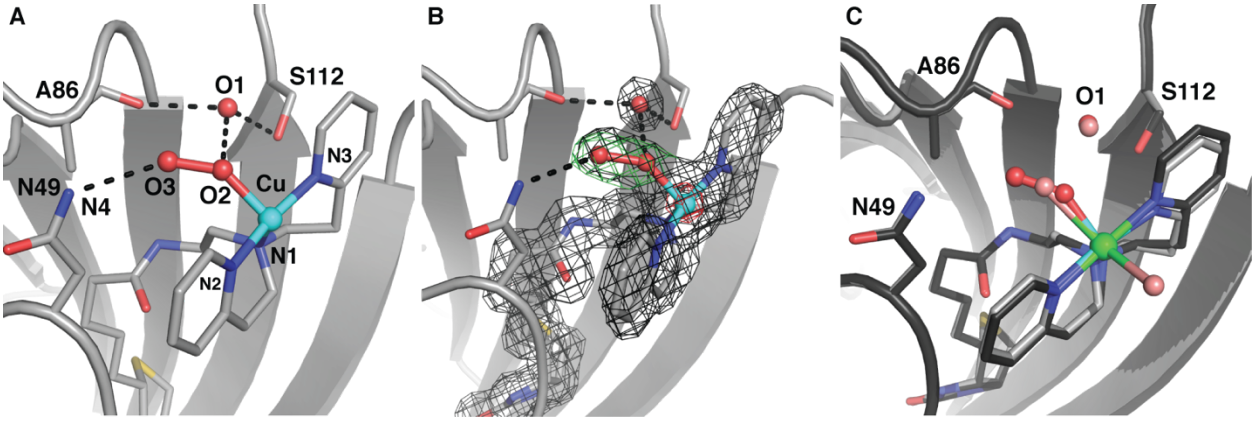

Figure 4-6. Structure of **1a-OOH** (**A-B**) and structural overlay of **1a** and **1a-OOH** (**C**). In **B**, the cofactor location is highlighted by the $2F_O$-F_C electron density map (grey mesh, contoured at 1σ), the F_O-F_C omit map (green mesh, contoured at 3σ), and the anomalous difference density (red mesh, contoured at 10σ). Copper ions are colored in cyan, O-atoms/water molecules are colored in red, N-atoms are colored in blue, and C-atoms are colored in grey. In **C**, **1a** has C-atoms in black, copper ions in green, and O-atoms/water molecules in salmon.

Table 4-2. Bond Lengths (Å) and Angles (°) for ArMs

Metrical Parameters	**1a-OOH**	**3a**	**4a**[a]	**4a**[b]
Cu–N1	2.01(1)	2.00(1)	1.98(1)	1.96(1)
Cu–N2	1.98(1)	1.98(1)	1.97(1)	1.97(1)
Cu–N3	1.99(1)	1.98(1)	1.97(1)	1.95(1)
Cu-O2	1.93(1)	2.49(1)	–	–
O2-O3	1.54(1)	–	–	–
N1–Cu–N2	101(1)	92(1)	92(1)	101(1)
N1–Cu–N3	95(1)	99(1)	102(1)	103(1)
N2–Cu–N3	164(1)	169(1)	165(1)	150(1)
N1–Cu–O2	107(1)	108(1)	–	–
N2–Cu–O2	88(1)	91(1)	–	–
N3–Cu–O2	91(1)	86(1)	–	–
Cu–O2–O3	143(1)	–	–	–

[a]primary conformation; [b]secondary conformation

a peroxide ion.[48,49] The Cu–O2 and O2–O3 bond lengths are also similar to those found for the proposed Cu–OOH species in ascorbate oxidase trapped *in crystallo*.[50]

The H-bonding interactions present in **1a-N_3** were also present in **1a-OOH** and are attributed for the stability of this reactive species. The immobilized Cu complex sits within the vestibule near residue N49 which forms an H-bond with the distal O-atom (O3) of the hydroperoxido ligand. A second H-bond is also formed between the proximal O-atom (O2) and the structural water molecule O1. This type of H-bonding network between both O-atoms of a hydroperoxido ligand is unknown in other Cu systems but is reminiscent of the type of interactions found in the heme proteins discussed in Chapter 1. The extended H-bonding network involving E51, R84, and N49 and the other involving O1, S112, O4, O5, and K121 were shown in Chapter 3 and are also present in **1a-OOH** (Fig. 4-7). The makeup of this network suggests that N49 acts as an H-bond donor to O3 and O1 donates an H-bond to O2.

Probing the Role of the H-bonding Network. The premise that the stability of the Cu^{II}–OOH

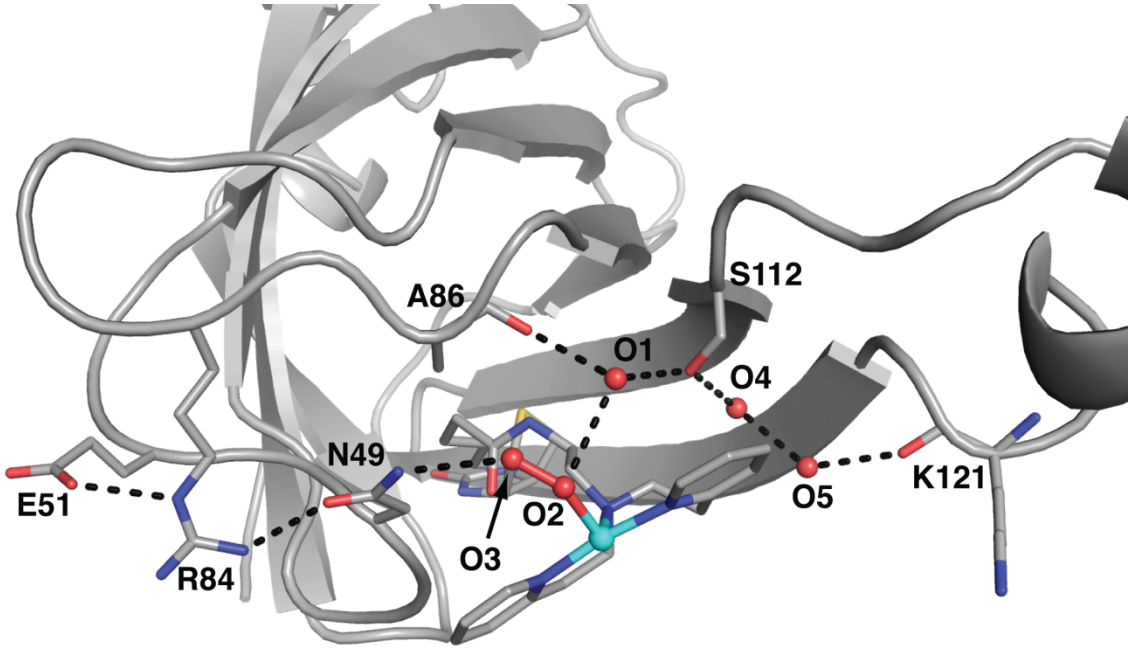

Figure 4-7. Structure of **1a-OOH** showing the extended H-bonding network within the local environment.

complex is due to H-bond network provided by the local environment was evaluated using different variants of Sav. Mutations of N49 or S112 to alanine would alter the H-bonding networks to possibly reduce the stability of the Cu^{II}–OOH unit. $[Cu^{II}$(biot-et-dpea)$(H_2O)_2]^{2+}$⊂Sav S112A (**4a**) was utilized, as in Chapter 3, to remove the structural water molecule O1 because it can no longer H-bond with S112. The 1.40 Å structure of **4a** showed that the occupancy of O1 is reduced substantially by 50%. Since O1 is not present to form an H-bond to an aqua ligand on the anchored Cu complex, as in **1a**, the complex is disordered over two positions (Fig. 4-8). Treating a solution of **4a** with H_2O_2 in 50 mM MES pH 6 gave an absorption spectrum like that for **1a-OOH**, however **4a-OOH** was not stable and decayed with a half-life of 20 minutes (Fig. 4-9, Table 4-1). *In crystallo* formation of **4a-OOH** was not successful. The other variant, N49A was used to prepare $[Cu^{II}$(biot-et-dpea)$(H_2O)_2]^{2+}$⊂Sav N49A (**3a**) to remove the H-bond to the distal O-atom of the hydroperoxido ligand. XRD

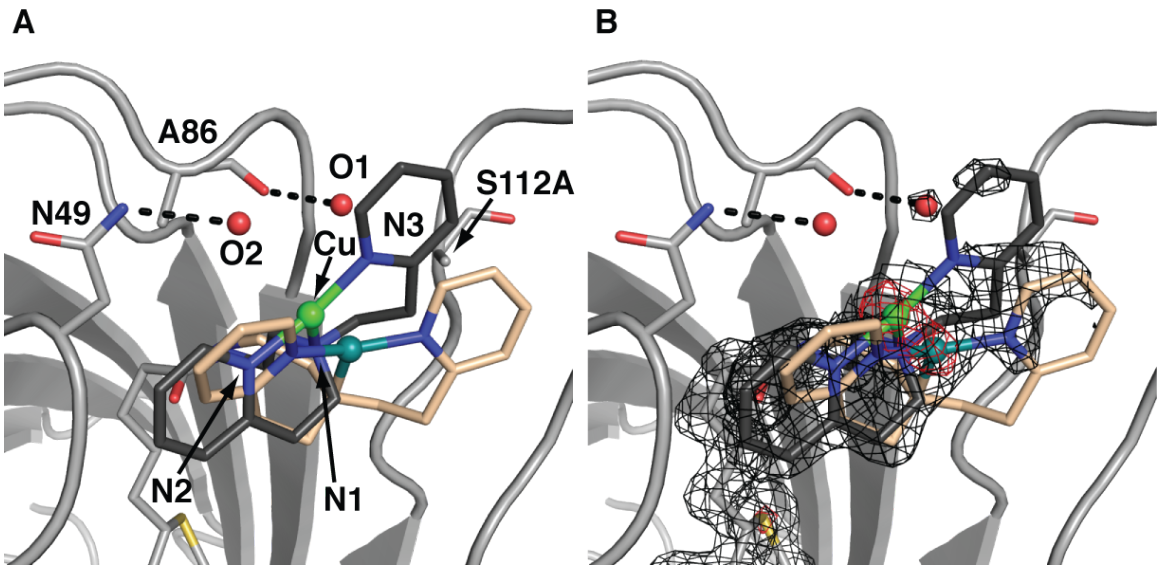

Figure 4-8. Structure of **4a** showing the two conformations of the disordered cofactor. The primary conformation has C-atoms in black and copper ions in green and the secondary conformation has C-atoms in tan and copper ions in teal. **B** shows the disordered cofactor position with $2F_O$-F_C electron density map (black mesh, contoured at 1σ) and anomalous difference density (red mesh, contoured at 4σ). Note the minimal density around O1 and O2 is ~ 3 Å from the copper center indicating that its transient binding.

analysis of **3a** showed multiple anomalous signals suggesting a disordered complex within the vestibule (see experimental section). The structure also showed that mutation of N49 to alanine disrupted the H-bonding network involving E51 and R84. **3a** was reacted with H_2O_2 *in situ* under the same conditions and produced $[Cu^{II}$(biot-et-dpea)(OOH)$]^+$⊂Sav N49A (**3a-OOH**) that had similar solution stability as **1a-OOH** (Fig. 4-10). Despite the solution stability of **3a-OOH**, attempts to prepare the variant *in crystallo* were unsuccessful – all H_2O_2 treated crystals showed a discorded Cu-aqua complex that was the same as observed in **3a.**

Reactivity Studies. The effects of the intramolecular H-bonds were further explored with reactivity studies involving external substrates. No reactivity was observed when **1a-OOH** was treated with substrates at room temperature in 50 mM MES pH 6. For example, addition of 4-chlorobenzylamine to **1a-OOH** resulted in no change in the absorbance spectrum and no detectable products after 1 h. A similar lack

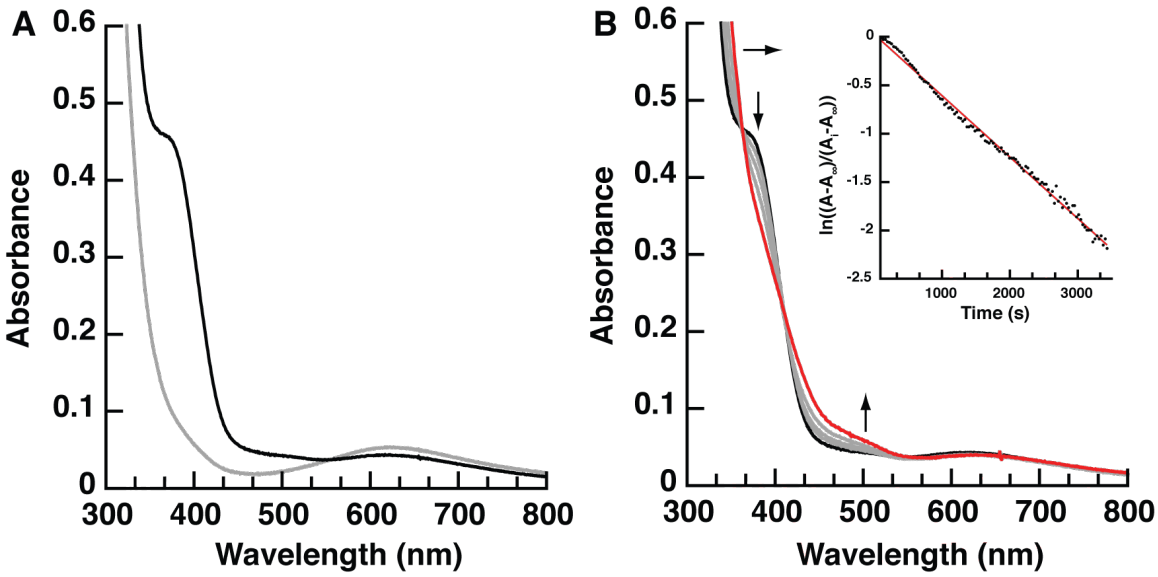

Figure 4-9. UV-vis spectra of **4a** before (grey) and after (black) reaction with H_2O_2 and (**B**) the decay of **4a-OOH** with rate data used to calculate half-life (inset).

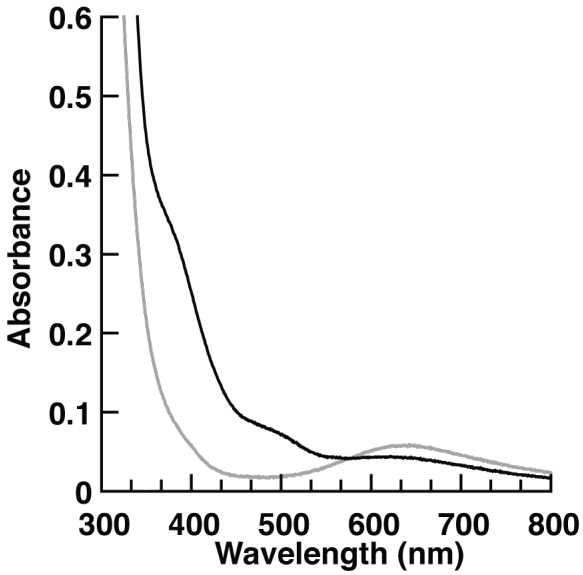

Figure 4-10. UV-vis spectra of **3a** before (grey) and after (black) reaction with H_2O_2.

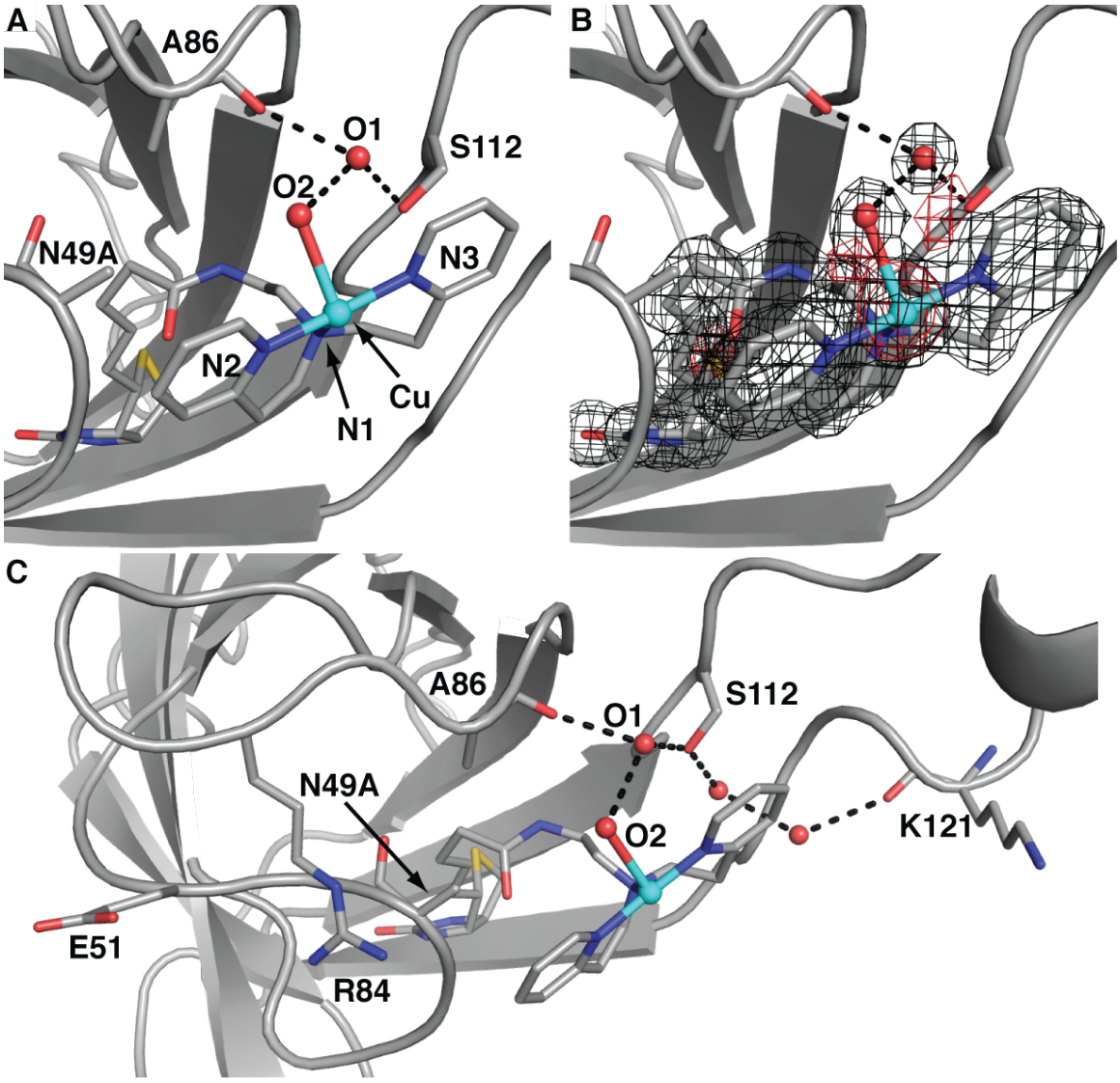

Figure 4-11. Structure of **3a** showing the primary cofactor position (**A-B**). **B** shows the cofactor position with $2F_O$-F_C electron density map (black mesh, contoured at 1σ) and anomalous difference density (red mesh, contoured at 4σ). Note there are two other anomalous signals indicating disorder. Copper ions are in cyan, O-atoms/water molecules are in red, and n-atoms are in blue. **C** shows the disrupted H-bonding network between E51, R84, and N49A.

of reactivity was observed for **3a-OOH**, the ArM produced with Sav N49A. However, oxidation reactions were observed with **4a-OOH**: in a typical reaction, ArM **4a-OOH** was treated with 4-chlorobenzylamine at room temperature and the absorbance band at λ_{max} = 375 nm disappeared within 10 minutes (Fig. 4-11). Analysis of the organic products by NMR spectroscopy showed production of *N*-(4-chorobenzyl)-1-(4-chlorophenyl)methanimine (**6**)

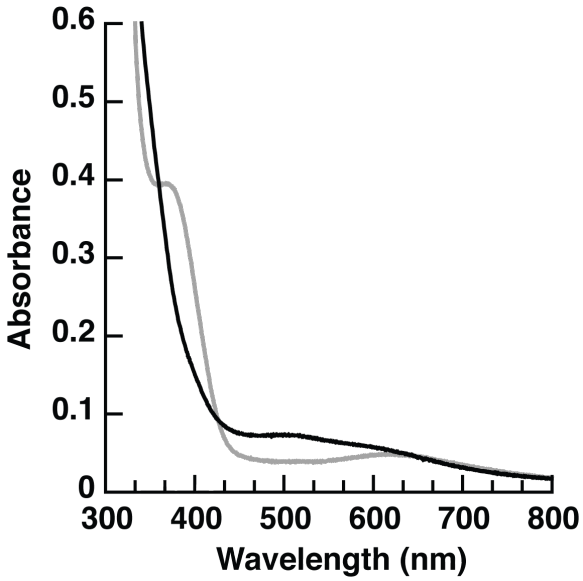

Figure 4-12. UV-vis spectra of **4a-OOH** before (grey) and after reaction with 4-chlorobenzylamine (black).

in 65% yield. The formation of this product is consistent with initial deamination of the amine to afford the oxidized species 4-chlorobenzaldehyde, which then reacts further with the remaining amine to produce the observed Schiff base (Scheme 4-2). In control experiments, $[Cu^{II}(biot\text{-}et\text{-}dpea)(OOH)]^+$ was treated with 4-chlorobenzylamine under the same conditions used with **4a-OOH**: analysis of the reaction mixture by ESI-MS showed a small molecular ion peak for **6**, but attempts to quantify the amount produced by NMR spectroscopy were unsuccessful as the amount of product was below the detection limit.

Summary and Conclusions. This study demonstrates that a Cu^{II}–OOH unit can be produced within a protein host in solution and *in crystallo* and that structural changes within the local environment can be used to control stability and reactivity. Cu^{II}–OOH complexes are normally unstable but within Sav WT a stable species was produced that we suggest was

Scheme 4-2. Oxidation of 4-chlorobenzylamine Mediated by **4a-OOH**

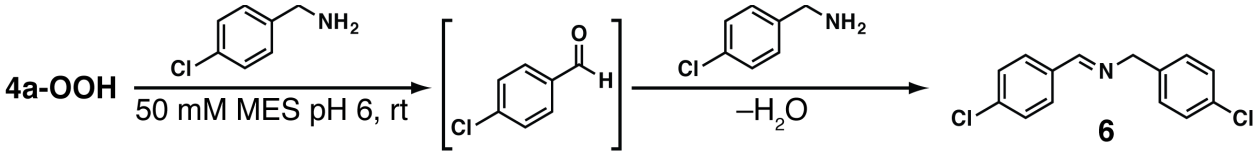

achieved through its confinement within the vestibule which provided H-bonding interactions to the hydroperoxido ligand. Protein function has been clearly linked to H-bonding networks that surround metal active sites, however it is still difficult to pinpoint the effects of individual interactions to understand their contributions to activity. ArMs **1a-OOH**, **3a-OOH**, and **4a-OOH** showed how changes in the H-bonds to a Cu^{II}–OOH center correlate with chemical function. An H-bond to each O-atom of the hydroperoxido ligand produced a stable species, however analysis of each individual interaction highlighted the importance of the H-bond to the proximal O-atom. Removal of this H-bond produced unstable ArM **4a-OOH** that could oxidize an external substrate, while removal of the H-bond to the distal O-atom in **3a-OOH** did not affect the stability of the Cu^{II}–OOH species. Similar effects from modulation of the H-bonding network have been observed in heme proteins in which function is linked to H-bonds with the Fe–OO(H) unit. Furthermore, our findings support the premise that specific placement of H-bonds around Cu–OOH intermediates assist in the activation of peroxides in PMOs and possibly other Cu monooxygenases.

Future Studies. Another outstanding question is the role of proximal residues within the local environment of LPMOs. Of particular interest is the placement of either a tyrosine or phenylalanine residue near the Cu active site that are not oxidized during enzymatic turnover. For instance, PMO AA9[51] contains a nearby tyrosine residue that has been shown to be weakly coordinating (Fig. 4-1), while, PMO *Jd*PMO10A[52] has a phenylalanine in the same position, which has no donor atoms to act as a ligand. It is difficult to engineer these types of proximal functional groups in purely synthetic system, however the relative ease with which Sav can be mutated provides an opportunity to explore these active sites.

To study the effect of having a tyrosine residue in the secondary coordination sphere, Sav K121Y was used to prepare ArM $[Cu^{II}(biot\text{-}et\text{-}dpea)(H_2O)_2]^{2+}\subset$Sav K121Y (**7a**). Reaction of this ArM with H_2O_2 using the same conditions as for **1a-OOH** gave a new absorption spectrum with the hydroperoxido-to-Cu^{II} LMCT at λ_{max} = 375 nm as well as a new band at λ_{max} = 485 nm (Fig. 4-12). This absorption band is only present when a tyrosine is present in the local environment, suggesting that this could be due to an oxidized tyrosine species. The absorption band is similar to that reported for the tyrosine-derived cofactor topaquinone (TPQ).[6] The identity of the species in **7a-OOH** responsible for the 480 nm band is still unknown; nevertheless, this results suggests that a tyrosine in the secondary coordination sphere, such as in LPMOs, must be appropriately placed to avoid non-productive oxidation.

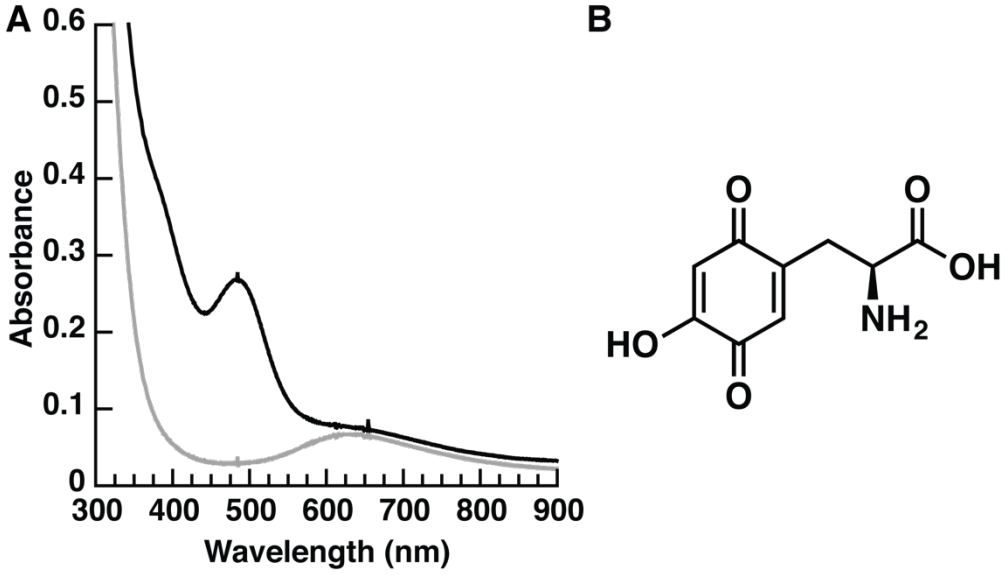

Figure 4-13. (**A**) UV-vis spectrum of **7a** before (grey) and after (black) reaction with H_2O_2 and (**B**) a ChemDraw of TPQ.

Experimental

General Methods. All commercially available reagents were obtained of the highest purity and used as received. Dimethylsulfoxide (DMSO), *N,N*-dimethylformamide (DMF), and

diethylether were degassed with argon and dried by vacuum filtration through activated alumina according to the procedure by Grubbs.[53] Triethylamine was distilled from KOH. The ligand (biot-et-dpea) and Cu^{II} complex $[Cu^{II}(biot\text{-}et\text{-}dpea)Cl_2]H_2O$ were prepared as published previously and discussed in Chapter 2.[54] The substrate 4-chlorobenzylamine was purchased from Sigma and used without further purification. The Schiff base N-4(-chlorobenzylidene)-4-chlorobenzylamine (**6**) was prepared as reported previously.[55]

Physical Methods

*Instrumentation***.** Electronic absorbance spectra were recorded with an 8453 Agilent UV-vis spectrophotometer. X-band (9.64 GHz) EPR spectra were measured on a Bruker spectrometer equipped with Oxford liquid helium cryostats.

Preparation of ArMs in Solution. A typical experiment was performed using a 350 μL solution of 150 μM Sav prepared in 50 mM MES buffer, pH 6 in a low-volume 1 cm cuvette. 21 μL of a 10 mM solution of $[Cu^{II}(biot\text{-}et\text{-}dpea)Cl_2]H_2O$ in DMF was added and allowed to incubate for 5 min. 100 equiv (2.14 μL) of H_2O_2 was added from a 9.8 M stock solution.

EPR Measurements. Reactions were monitored by UV-vis before being quickly transferred to an EPR tube and frozen in liquid nitrogen. To 500 μL of a 250 μM solution of Sav in 50 mM MES buffer, pH 6.0 was added 10 μL of a 50 mM solution of $[Cu^{II}(biot\text{-}et\text{-}dpea)Cl_2]H_2O$ in DMF. The solution was allowed to incubate for 5 min before addition of H_2O_2 (5.1 μL of a 9.8 M solution). The absorbance at λ_{max} = 375 nm was monitored and samples were frozen once the maximum absorbance was reached.

Substrate Reactivity Studies. In a typical experiment 700 μL 150 μM Sav in 50 mM MES pH6 and 42 μL 10 mM $[Cu^{II}(biot\text{-}et\text{-}dpea)Cl_2]H_2O$ in DMF were added to a cuvette. 4.28 μL of 9.8 M H_2O_2 was then added. The UV-vis spectrum was monitored until maximum growth of the

λ_{max} = 375 nm absorption band and then 20.8 µL of 1 M 4-chlorobenzylamine was added. After 10 min, the solution was transferred to a vial and diluted with 2 mL of nanopure H_2O. The reaction was then extracted with 3 x 6 mL Et_2O. The organic layer was dried over $MgSO_4$, filtered, and dried under vacuum. The residue was then dissolved in 500 µL of $CDCl_3$ and 10 µL of 0.132 M ferrocene in $CDCl_3$ (for an internal reference) was added before analysis by ^1H NMR and ESI-MS (Fig. 4-14 & 15). The ^1H NMR spectrum was compared to independently synthesized **6**. The amount of product (**6**) was determined by comparing the integration of the imine proton signal at 8.345 ppm to the $FeCp_2$ signal at 4.16 ppm (Fig. 4-14).[56]

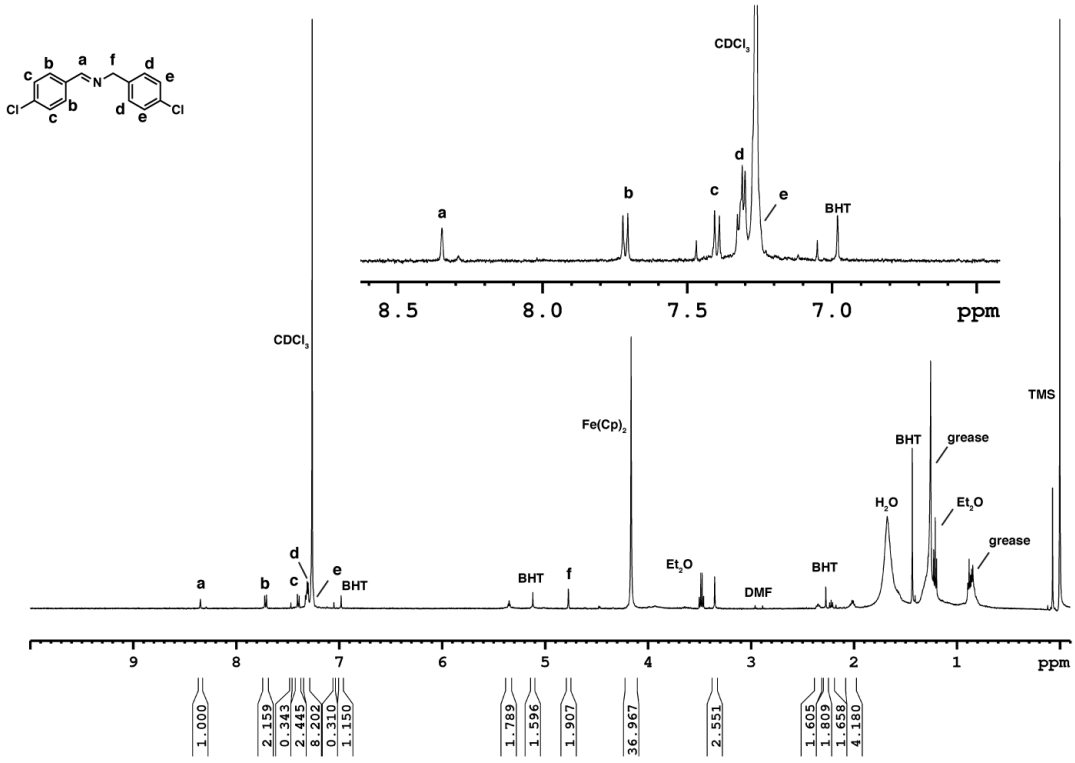

Figure 4-14. ^1H NMR spectrum of **6** isolated from the reaction of **4a-OOH** with 4-chlorobenzylamine.

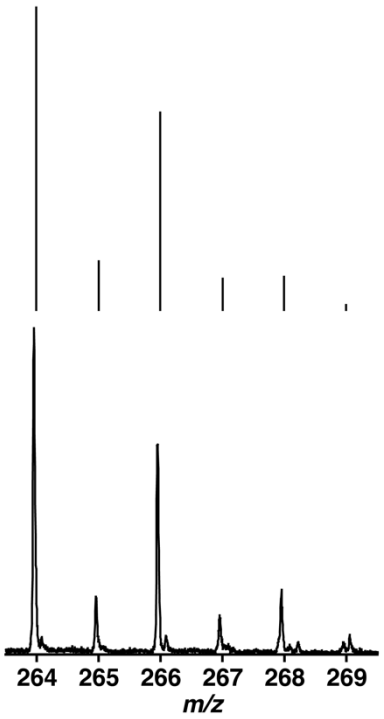

Figure 4-15. ESI-mass spectrum with calculated isotope distribution pattern of [**6**+H]$^+$ isolated from the reaction of **4a-OOH** with 4-chlorobenzylamine.

Protein Crystallization, X-ray Data Collection and Processing

*Crystallization of [Cu^{II}(biot-et-dpea)(OO(H))]$^+$⊂Sav WT (**1a-OOH**).* Apo-Sav WT protein crystals were obtained at 20 °C within two days by sitting-drop vapor diffusion technique mixing 1.5 µL crystallization buffer (2.0 M ammonium sulfate, 0.1 M sodium acetate, pH 4.0) and 3.5 µL protein solution (26 mg/mL lyophilized protein in water). The droplet was equilibrated against a reservoir solution of 100 µL crystallization buffer. Subsequently, single crystals of Sav were soaked for 1 day at 20 °C in a soaking buffer, which was prepared by mixing 1 µL of a 10 mM stock solution of complex [Cu^{II}(biot-et-dpea)Cl$_2$]H$_2$O (in water with 100 mM CuCl$_2$), 9 µL crystallization buffer, and 0.5 µL of the original protein solution. After the soaking, crystals were transferred for 10 min into a cryo-protectant solution (30 %

(v/v) glycerol in crystallization buffer) containing 1 mM H_2O_2. The crystals were then shock-frozen in liquid nitrogen.

*Crystallization of [Cu^{II}(biot-et-dpea)(OH_2)]$^{2+}$⊂N49A Sav (**3a**).* Apo-Sav N49A protein crystals were obtained following the same procedure used to isolate crystals of **1a**. The single crystals of Sav $N_{49}A$ were soaked for 1 day at 20 °C in a soaking buffer, which was prepared by mixing 1 μL of a 10 mM stock solution of [Cu^{II}(biot-et-dpea)Cl_2]H_2O in water, 9 μL crystallization buffer, and 0.5 μL of the original protein solution. After soaking, the crystals were transferred into a cryo-protectant solution (30 % (v/v) glycerol in crystallization buffer) before being shock-frozen in liquid nitrogen.

*Crystallization of [Cu^{II}(biot-et-dpea)]$^{2+}$⊂S112A Sav (**4a**).* Apo-Sav S112A crystals were obtained following the same procedure used to isolate crystals of **1a**. The single crystals of Sav S112A were then soaked for 1 d at 20 °C in a soaking buffer, which was prepared by mixing 1 μL of a 10 mM stock solution of complex [Cu^{II}(biot-et-dpea)Cl_2]H_2O in water, 9 μL crystallization buffer, and 0.5 μL of the original protein solution. After soaking, the crystals were transferred into a cryo-protectant solution (30 % (v/v) glycerol in crystallization buffer) before being shock-frozen in liquid nitrogen.

Diffraction Data Processing. X-ray diffraction data were collected at the Advanced Light Source (BL 8.2.1 and 8.2.2) at a wavelength of 1 Å and processed with software XDS[57] and scaled with AIMLESS (CCP4 Suite).[58] The structure was solved by molecular replacement using program PHASER (CCP4 Suite) [58] and the structure 2QCB from the PDB as input model with ligand and water molecules removed. For structure refinement REFMAC5 (CCP4 Suite)[59] and PHENIX.REFINE[60] were used. Cu-complex manipulation was carried out with programs REEL and COOT using the Cu-complex coordinates of PDB structures 5K49.[54] For

water picking, electron density, and structure visualization, the software COOT[61] was used. Figures were drawn with PyMOL (the PyMOL Molecular Graphics System, Version 1.5.0.5, Schrödinger, LLC). Crystallographic details, processing and refinement statistics are given in Supplementary Table 4-3 and 4-4.

Crystal Structures

Overall Structures. Apo-crystals of proteins WT, N49A, and S112A Sav soaked with [Cu^{II}(biot-et-dpea(OH_2)Cl]Cl constituted space group $I4_122$ with unit cell parameters reported in Table S1. A single Sav monomer was obtained per asymmetric unit after molecular replacement. Protein residues 2-9 and 135-159 of the N- and C-terminus, respectively, were not resolved in the electron density, presumably due to disorder. Starting from the Sav monomer the biological homotetramer is generated by application of crystallographic C2-symmetry axes along the x-, y- and z-axes of the unit cell. The overall protein structures are virtually identical to structure biotin⊂WT Sav (PDB 1STP, see Table 4-4).

General Complex Modeling. For all structures of apo-protein crystals soaked with the Cu-complex the following general observations were made: i) residual electron density in the F_o-F_c map was observed in the biotin binding pocket and in the biotin vestibule, ii) one (complex **1a-OOH** and **7a-OOH**) or more (complexes **3a** and **4a**) peaks in an anomalous dispersion density map in the biotin vestibule superimposed with the electron density peak (Figures 4-6, 8, & 10). The residual electron density was fit with the Cu-complex which projected Cu to the position of the strong anomalous density peak.

*Structural Details for Complexes **1a-OOH**, **3a**, **4a**, and **7a-OOH**.* For structural details see main text and the following figures and tables: Fig. 6-8, 10, 13-16, Table 4-2-4.

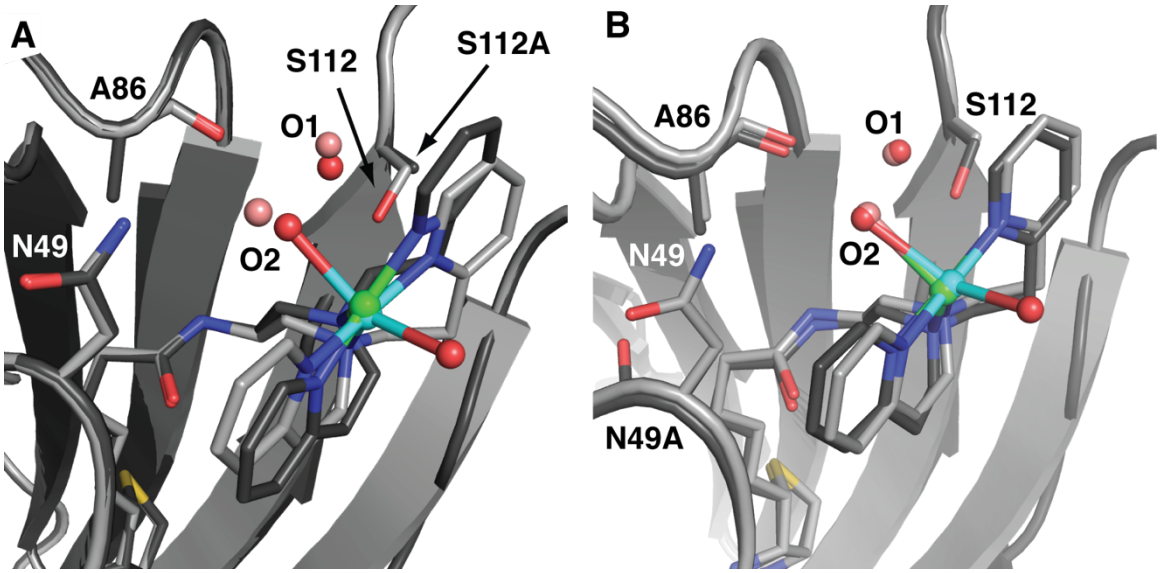

Figure 4-16. Structural overlays of **1a** and **4a** (**A**) and **1a** and **3a** (**B**). Note in **A**, only the primary structure of **4a** is shown.

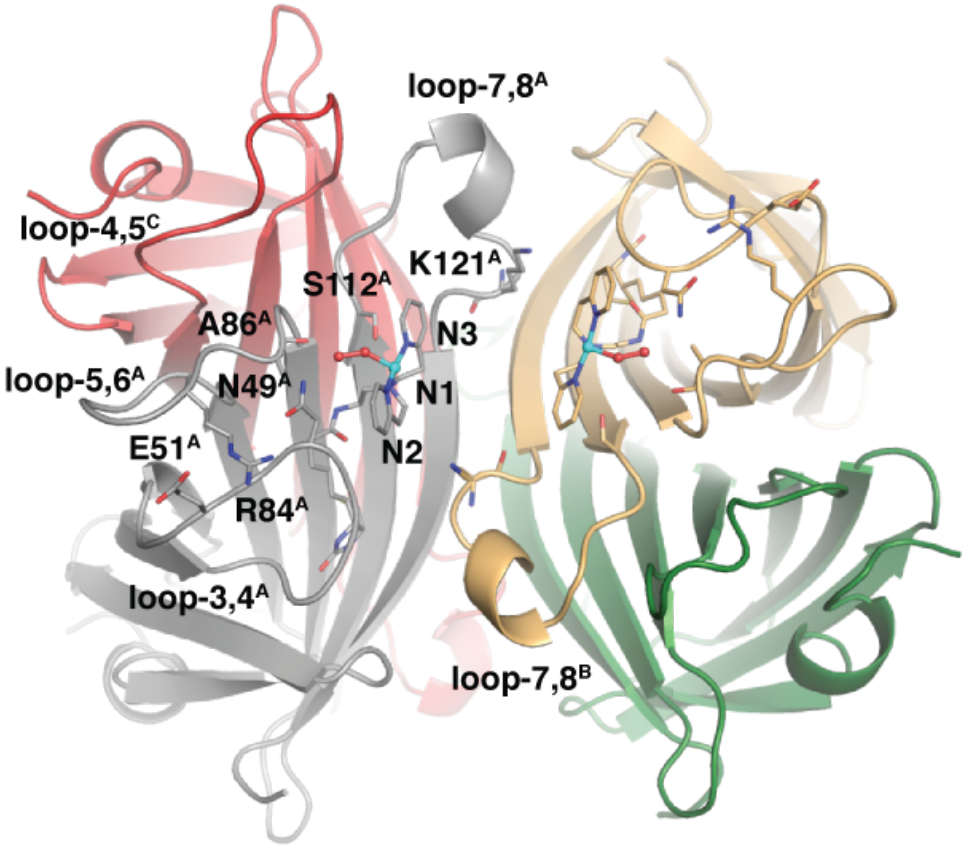

Figure 4-17. Tetrameric view of **1a-OOH** shown as a cartoon. Subunit A is in grey, subunit B is in tan, subunit C is in red, and subunit D is in green.

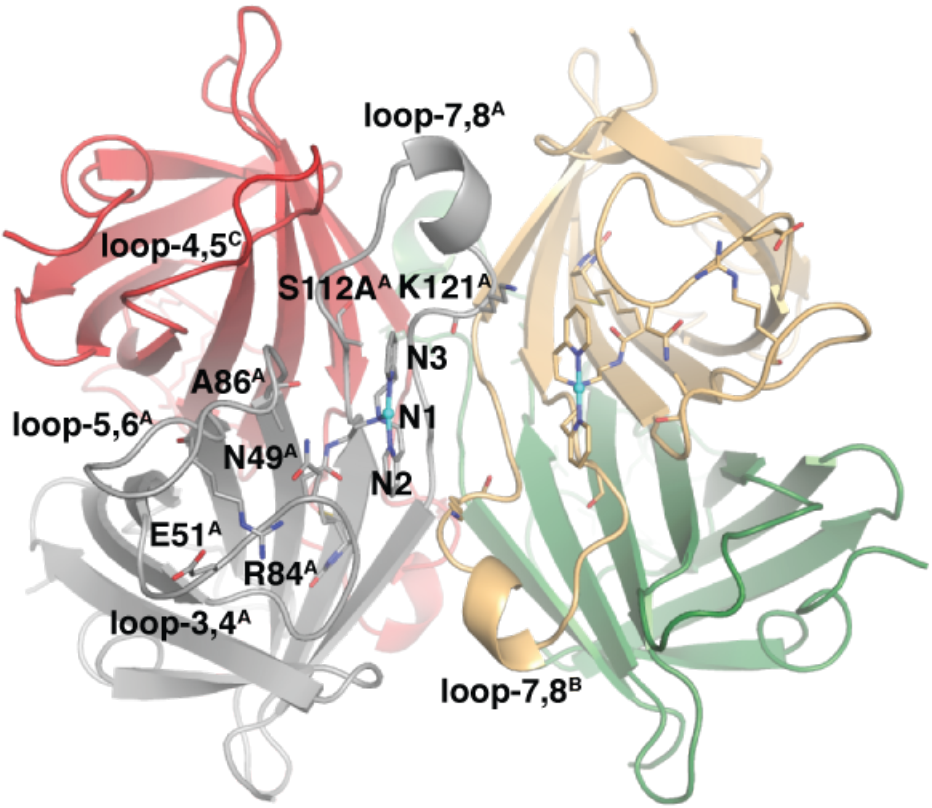

Figure 4-18. Tetrameric view of **4a** shown as a cartoon. Subunit A is in grey, subunit B is in tan, subunit C is in red, and subunit D is in green.

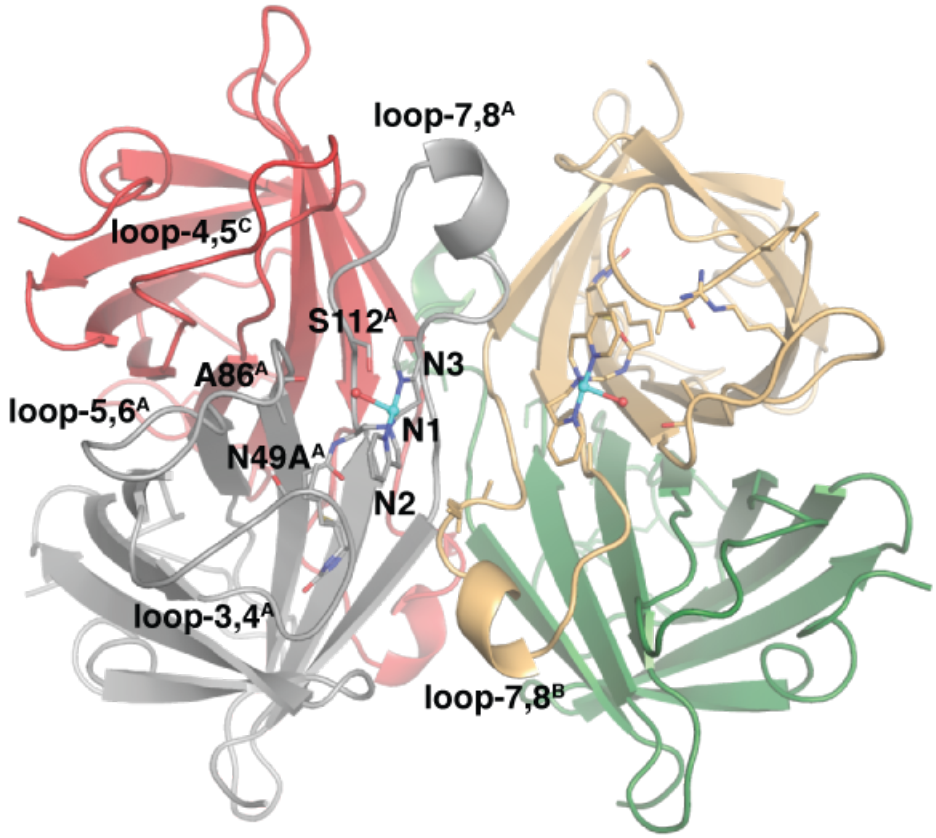

Figure 4-19. Tetrameric view of **3a** shown as a cartoon. Subunit A is in grey, subunit B is in tan, subunit C is in red, and subunit D is in green.

Table 4-3. X-ray Crystallographic Data Processing and Refinement Statistics

Sav Mutant	WT	N49A	S112A
Cu complex	$[Cu^{II}$(biot-et-dpea)(OO(H))$]^{+}$ (**1a-OOH**)	Cu^{II}(biot-et-dpea)$(OH_2)]^{2+}$ (**3a**)	$[Cu^{II}$(biot-et-dpea)$(OH_2)]^{2+}$ (**4a**)
PDB code	5WBA	5WBD	5WBB
Cu complex PDB 3-letter code	SI8	S17	SQ1
Data Processing			
Unit Cell	a, b, c = 57.5 Å, 57.5 Å, 183.1 Å; α, β, γ = 90°	a, b, c = 57.5 Å, 57.5 Å, 174.8 Å; α, β, γ = 90°	a, b, c = 57.6 Å, 57.6 Å, 184.0 Å; α, β, γ = 90°
Space group	$I4_122$	$I4_122$	$I4_122$
Resolution (Å)	54.9 – 1.50	54.63-1.50	55.0-1.50
Highest resolution shell (Å)	1.53 - 1.50	1.53-1.50	1.54-1.50
R_{merge} (%)	5.2 (28.2)	7.5 (36.1)	4.1 (20.1)
No. of unique reflections	24121 (858)	24051 (1139)	20815 (842)
Multiplicity	7.0 (2.1)	11.2 (8.6)	6.0 (3.1)
I/sig(I)	20.2 (2.3)	18.6 (3.3)	23.5 (4.2)
Completeness	95.8 (71.1)	99.9 (97.8)	95.8 (81.6)
CC(1/2)	0.998 (0.84)	0.998 (0.941)	0.999 (0.945)
Structure Refinement			
R_{work}	0.14	0.15	0.16
R_{free}	0.15	0.18	0.19
Rmsd bond length (Å)	0.0093	0.0078	0.0088
Rmsd bond angle (°)	1.4330	1.4612	1.7848
Rmsd compared to biotin-SAV WT (PDB 1STP) (Å)	0.72	0.78	0.71
No ligands Cu complex Water Acetate $SO4^{2-}$ Glycerol Cu	 1 105 1 1 - 1	 1 98 1 - - -	 1 111 - 1 1 1

Table 4-4. Summary of Structural Details

PDB code	5WBA	5WBD	5WBB
Sav Mutant	WT	N49A	S112A
Complex	**1a-OOH**	**3a**	**4a**
Electron density at Cu (primary) in FoFc omit map (σ)	25	34	22
Anomalous dispersion density at primary Cu (σ)	18	33	16
Anomalous dispersion density at secondary Cu (σ)	-	6	8
Geometry of Cu complex	Distorted see-saw	Distorted see-saw	Distorted see-saw
Coordination number of Cu complex	4	4	3[c]
Occupancy of structural water (O1)[a]	0.7	0.7	0.3
Occupancy of Cu complex in primary site (%)	100	100	70
Occupancy of Cu complex in secondary site (%)	0	0[d]	30
B-factor (Å^2) Overall protein Loop-7,8[b] Cu complex Cu (primary site) Cu (secondary site)	 20 21 29 38 -	 15 16 18 24 -	 20 20 23 30 22
Distance Cu-Cu (primary sites) (Å)	11.2	11.4	11.6

[a]Occupancies were determined using PHENIX.REFINE automatic occupancy refinement
[b]loop-7,8 comprises residues 114-121
[c]A water molecule in close proximity to the primary Cu (3 Å) presumably is only transiently coordinated.
[d]No density was observed for additional ligand conformations, however small amounts of additional anomalous signals suggest multiple copper conformations

References

(1) Klinman, J. P. The Copper-Enzyme Family of Dopamine β-Monooxygenase and Peptidylglycine α-Hydroxylating Monooxygenase: Resolving the Chemical Pathway for Substrate Hydroxylation. *J. Biol. Chem.* **2006**, *281* (6), 3013–3016.

(2) Kunishita, A.; Ertem, M. Z.; Okubo, Y.; Tano, T.; Sugimoto, H.; Ohkubo, K.; Fujieda, N.; Fukuzumi, S.; Cramer, C. J.; Itoh, S. Active Site Models for the CuA Site of Peptidylglycine α-Hydroxylating Monooxygenase and Dopamine β-Monooxygenase. *Inorg. Chem.*

2012, *51* (17), 9465–9480.
(3) Prigge, S. T.; Kolhekar, A. S.; Eipper, B. A.; Mains, R. E.; Amzel, L. M. Amidation of Bioactive Peptides: The Structure of Peptidylglycine α-Hydroxylating Monooxygenase. *Science* **1997**, *278* (5341), 1300–1305.
(4) Abad, E.; Rommel, J. B.; Kästner, J. Reaction Mechanism of the Bicopper Enzyme Peptidylglycine α-Hydroxylating Monooxygenase. *J. Biol. Chem.* **2014**, *289* (20), 13726–13738.
(5) Chen, P.; Solomon, E. I. Oxygen Activation by the Noncoupled Binuclear Copper Site in Peptidylglycine Alpha-Hydroxylating Monooxygenase. Reaction Mechanism and Role of the Noncoupled Nature of the Active Site. *J. Am. Chem. Soc.* **2004**, *126* (15), 4991–5000.
(6) Mure, M. Tyrosine-Derived Quinone Cofactors. *Acc. Chem. Res.* **2004**, *37* (2), 131–139.
(7) Hemsworth, G. R.; Henrissat, B.; Davies, G. J.; Walton, P. H. Discovery and Characterization of a New Family of Lytic Polysaccharide Monooxygenases. *Nat. Chem. Biol.* **2014**, *10* (2), 122–126.
(8) Span, E. A.; Marletta, M. A. The Framework of Polysaccharide Monooxygenase Structure and Chemistry. *Curr. Opin. Struct. Biol.* **2015**, *35*, 93–99.
(9) Beeson, W. T.; Vu, V. V; Span, E. A.; Phillips, C. M.; Marletta, M. A. Cellulose Degradation by Polysaccharide Monooxygenases. *Annu. Rev. Biochem.* **2015**, *84*, 923–946.
(10) Vaaje-Kolstad, G.; Westereng, B.; Horn, S. J.; Liu, Z.; Zhai, H.; Sorlie, M.; Eijsink, V. G. H.; Sørlie, M.; Eijsink, V. G. H. An Oxidative Enzyme Boosting the Enzymatic Conversion of Recalcitrant Polysaccharides. *Science* **2010**, *330* (6001), 219–222.
(11) Hemsworth, G. R.; Davies, G. J.; Walton, P. H. Recent Insights into Copper-Containing Lytic Polysaccharide Mono-Oxygenases. *Curr. Opin. Struct. Biol.* **2013**, *23* (5), 660–668.
(12) Hemsworth, G. R.; Taylor, E. J.; Kim, R. Q.; Gregory, R. C.; Lewis, S. J.; Turkenburg, J. P.; Parkin, A.; Davies, G. J.; Walton, P. H. The Copper Active Site of CBM33 Polysaccharide Oxygenases. *J. Am. Chem. Soc.* **2013**, *135* (16), 6069–6077.
(13) Jackson, T. A.; Brunold, T. C. Combined Spectroscopic/computational Studies on Fe- and Mn-Dependent Superoxide Dismutases: Insights into Second-Sphere Tuning of Active Site Properties. *Acc. Chem. Res.* **2004**, *37* (7), 461–470.
(14) Lah, M. S.; Dixon, M. M.; Pattridge, K. A.; Stallings, W. C.; Fee, J. A.; Ludwig, M. L. Structure-Function in Escherichia-Coli Iron Superoxide-Dismutase - Comparisons with the Manganese Enzyme from Thermus-Thermophilus. *Biochemistry* **1995**, *34* (5), 1646–1660.
(15) Xie, J.; Yikilmaz, E.; Miller, A. F.; Brunold, T. C. Second-Sphere Contributions to Substrate-Analogue Binding in iron(III) Superoxide Dismutase. *J. Am. Chem. Soc.* **2002**, *124* (14), 3769–3774.
(16) Yikilmaz, E.; Xie, J.; Brunold, T. C.; Miller, A. F. Hydrogen-Bond-Mediated Tuning of the Redox Potential of the Non-Heme Fe Site of Superoxide Dismutase. *J. Am. Chem. Soc.* **2002**, *124* (14), 3482–3483.
(17) Edwards, R. A.; Whittaker, M. M.; Whittaker, J. W.; Baker, E. N.; Jameson, G. B. Outer Sphere Mutations Perturb Metal Reactivity in Manganese Superoxide Dismutase. *Biochemistry* **2001**, *40* (1), 15–27.
(18) Ramilo, C. A.; Leveque, V.; Guan, Y.; Lepock, J. R.; Tainer, J. A.; Nick, H. S.; Silverman, D. N. Interrupting the Hydrogen Bond Network at the Active Site of Human Manganese Superoxide Dismutase. *J. Biol. Chem.* **1999**, *274* (39), 27711–27716.

(19) Yikilmaz, E.; Porta, J.; Grove, L. E.; Vahedi-Faridi, A.; Bronshteyn, Y.; Brunold, T. C.; Borgstahl, G. E. O.; Miller, A.-F. How Can a Single Second Sphere Amino Acid Substitution Cause Reduction Midpoint Potential Changes of Hundreds of Millivolts? *J. Am. Chem. Soc.* **2007**, *129* (32), 9927–9940.
(20) Miller, A.-F. Redox Tuning over Almost 1 V in a Structurally Conserved Active Site: Lessons from Fe-Containing Superoxide Dismutase. *Acc. Chem. Res.* **2008**, *41* (4), 501–510.
(21) Cook, S. A.; Hill, E. A.; Borovik, A. S. Lessons from Nature: A Bio-Inspired Approach to Molecular Design. *Biochemistry* **2015**, *54* (27), 4167–4180.
(22) Cook, S. A.; Borovik, A. S. Molecular Designs for Controlling the Local Environments around Metal Ions. *Acc. Chem. Res.* **2015**, *48* (8), 2407–2414.
(23) Liu, J.; Chakraborty, S.; Hosseinzadeh, P.; Yu, Y.; Tian, S.; Petrik, I.; Bhagi, A.; Lu, Y. Metalloproteins Containing Cytochrome, Iron–Sulfur, or Copper Redox Centers. *Chem. Rev.* **2014**, *114* (8), 4366–4469.
(24) Itoh, S. Mononuclear Copper Active-Oxygen Complexes. *Curr. Opin. Chem. Biol.* **2006**, *10* (2), 115–122.
(25) Shaanan, B. The Iron-Oxygen Bond in Human Oxyhaemoglobin. *Nature* **1982**, *296* (5858), 683–684.
(26) Yang, J.; Kloek, A. P.; Goldberg, D. E.; Mathews, F. S. The Structure of Ascaris Hemoglobin Domain I at 2.2 Å Resolution: Molecular Features of Oxygen Avidity. *Proc. Natl. Acad. Sci. U. S. A.* **1995**, *92* (10), 4224–4228.
(27) Condon, P. J.; Royer, W. E. Crystal Structure of Oxygenated Scapharca Dimeric Hemoglobin at 1.7-Å Resolution. *J. Biol. Chem.* **1994**, *269* (41), 25259–25267.
(28) Huang, S.; Huang, J.; Kloek, A. P.; Goldberg, D. E.; Friedman, J. M. Hydrogen Bonding of Tyrosine B10 to Heme-Bound Oxygen in Ascaris Hemoglobin. Direct Evidence from UV Resonance Raman Spectroscopy. *J. Biol. Chem.* **1996**, *271* (2), 958–962.
(29) Paoli, M.; Liddington, R.; Tame, J.; Wilkinson, A.; Dodson, G. Crystal Structure of T State Haemoglobin with Oxygen Bound At All Four Haems. *J. Mol. Biol.* **1996**, *256* (4), 775–792.
(30) Poulos, T. L. Heme Enzyme Crystal-Structures. *Adv. Inorg. Biochem.* **1988**, *7*, 1–36.
(31) Poulos, T. L. Heme Enzyme Structure and Function. *Chem. Rev.* **2014**, *114* (7), 3919–3962.
(32) Martinis, S. A.; Atkins, W. M.; Stayton, P. S.; Sligar, S. G. A Conserved Residue of Cytochrome-P-450 Is Involved in Heme-Oxygen Stability and Activation. *J. Am. Chem. Soc.* **1989**, *111* (26), 9252–9253.
(33) Nagano, S.; Poulos, T. L. Crystallographic Study on the Dioxygen Complex of Wild-Type and Mutant Cytochrome P450cam - Implications for the Dioxygen Activation Mechanism. *J. Biol. Chem.* **2005**, *280* (36), 31659–31663.
(34) Schlichting, I.; Berendzen, J.; Chu, K.; Stock, A. M.; Maves, S. A.; Benson, D. E.; Sweet, R. M.; Ringe, D.; Petsko, G. A.; Sligar, S. G. The Catalytic Pathway of Cytochrome P450cam at Atomic Resolution. *Science* **2000**, *287* (5458), 1615–1622.
(35) Gerber, N. C.; Sligar, S. G. Catalytic Mechanism of Cytochrome P-450: Evidence for a Distal Charge Relay. *J. Am. Chem. Soc.* **1992**, *114* (22), 8742–8743.
(36) Yamaguchi, S.; Nagatomo, S.; Kitagawa, T.; Funahashi, Y.; Ozawa, T.; Jitsukawa, K.; Masuda, H. Copper Hydroperoxo Species Activated by Hydrogen-Bonding Interaction with Its Distal Oxygen. *Inorg. Chem.* **2003**, *42* (22), 6968–6970.

(37) Tian, G.; Berry, J. A.; Klinman, J. P. Oxygen-18 Kinetic Isotope Effects in the Dopamine β-Monooxygenase Reaction: Evidence for a New Chemical Mechanism in Non-Heme Metallomonooxygenases. *Biochemistry* **1994**, *33* (1), 226–234.
(38) Span, E. A.; Suess, D. L. M.; Deller, M. C.; Britt, R. D.; Marletta, M. A. The Role of the Secondary Coordination Sphere in a Fungal Polysaccharide Monooxygenase. *ACS Chem. Biol.* **2017**, *12* (4), 1095–1103.
(39) Wada, A.; Harata, M.; Hasegawa, K.; Jitsukawa, K.; Masuda, H.; Mukai, M.; Kitagawa, T.; Einaga, H. Structural and Spectroscopic Characterization of a Mononuclear Hydroperoxo-Copper(II) Complex with Tripodal Pyridylamine Ligands. *Angew. Chem. Int. Ed..* **1998**, *37* (6), 798–799.
(40) Kim, S.; Saracini, C.; Siegler, M. A.; Drichko, N.; Karlin, K. D. Coordination Chemistry and Reactivity of a Cupric Hydroperoxide Species Featuring a Proximal H-Bonding Substituent. *Inorg. Chem.* **2012**, *51* (23), 12603–12605.
(41) Wada, A.; Harata, M.; Hasegawa, K.; Jitsukawa, K.; Masuda, H.; Mukai, M.; Kitagawa, T.; Einaga, H. Structural and Spectroscopic Characterization of a Mononuclear Hydroperoxo - copper(II) Complex with Tripodal Pyridylamine Ligands. *Angew. Chem. Int. Ed.* **1998**, *37* (6), 798–799.
(42) Chen, P.; Fujisawa, K.; Solomon, E. I. Spectroscopic and Theoretical Studies of Mononuclear Copper(II) Alkyl- and Hydroperoxo Complexes: Electronic Structure Contributions to Reactivity. *J. Am. Chem. Soc.* **2000**, *122* (41), 10177–10193.
(43) Fujii, T.; Naito, A.; Yamaguchi, S.; Wada, A.; Funahashi, Y.; Jitsukawa, K.; Nagatomo, S.; Kitagawa, T.; Masuda, H. Construction of a Square-Planar Hydroperoxo-Copper (II) Complex Inducing a Higher Catalytic Reactivity. *Chem. Comm.* **2003**, 2700–2701.
(44) Maiti, D.; Sarjeant, A. A. N.; Karlin, K. D. Copper(II)-Hydroperoxo Complex Induced Oxidative N-Dealkylation Chemistry. *J. Am. Chem. Soc.* **2007**, *129* (21), 6720–6721.
(45) Kunishita, A.; Kubo, M.; Ishimaru, H.; Ogura, T.; Sugimoto, H.; Itoh, S. H2O2-Reactivity of copper(II) Complexes Supported by Tris[(pyridin-2-Yl)methyl]amine Ligands with 6-Phenyl Substituents. *Inorg. Chem.* **2008**, *47* (24), 12032–12039.
(46) Itoh, S. Developing Mononuclear Copper–Active-Oxygen Complexes Relevant to Reactive Intermediates of Biological Oxidation Reactions. *Acc. Chem. Res.* **2015**, *48* (7), 2066–2074.
(47) Zhu, Q.; Lian, Y.; Thyagarajan, S.; Rokita, S. E.; Karlin, K. D.; Blough, N. V. Hydrogen Peroxide and Dioxygen Activation by Dinuclear Copper Complexes in Aqueous Solution: Hydroxyl Radical Production Initiated by Internal Electron Transfer. *J. Am. Chem. Soc.* **2008**, *130* (20), 6304–6305.
(48) Li, X.; Beeson, W. T.; Phillips, C. M.; Marletta, M. A.; Cate, J. H. D. Structural Basis for Substrate Targeting and Catalysis by Fungal Polysaccharide Monooxygenases. *Structure* **2012**, *20* (6), 1051–1061.
(49) O'Dell, W. B.; Agarwal, P. K.; Meilleur, F. Oxygen Activation at the Active Site of a Fungal Lytic Polysaccharide Monooxygenase. *Angew. Chem. Int. Ed..* **2017**, *56* (3), 767–770.
(50) Messerschmidt, A.; Luecke, H.; Huber, R. X-Ray Structures and Mechanistic Implications of Three Functional Derivatives of Ascorbate Oxidase from Zucchini. *J. Mol. Biol.* **1993**, *230* (3), 997–1014.
(51) Quinlan, R. J.; Sweeney, M. D.; Lo Leggio, L.; Otten, H.; Poulsen, J.-C. N.; Johansen, K. S.; Krogh, K. B. R. M.; Jorgensen, C. I.; Tovborg, M.; Anthonsen, A.; Tryfona, T.; Walter, C. P.; Dupree, P.; Xu, F.; Davies, G. J.; Walton, P. H. Insights into the Oxidative Degradation of

Cellulose by a Copper Metalloenzyme That Exploits Biomass Components. *Proc. Natl. Acad. Sci.* **2011**, *108* (37), 15079–15084.
(52) Gudmundsson, M.; Kim, S.; Wu, M.; Ishida, T.; Momeni, M. H.; Vaaje-Kolstad, G.; Lundberg, D.; Royant, A.; Ståhlberg, J.; Eijsink, V. G. H.; Beckham, G. T.; Sandgren, M. Structural and Electronic Snapshots during the Transition from a Cu(II) to Cu(I) Metal Center of a Lytic Polysaccharide Monooxygenase by X-Ray Photoreduction. *J. Biol. Chem.* **2014**, *289* (27), 18782–18792.
(53) Pangborn, A. B.; Giardello, M. A.; Grubbs, R. H.; Rosen, R. K.; Timmers, F. J. Safe and Convenient Procedure for Solvent Purification. *Organometallics* **1996**, *15*, 1518–1520.
(54) Mann, S. I.; Heinisch, T.; Weitz, A. C.; Hendrich, M. P.; Ward, T. R.; Borovik, A. S. Modular Artificial Cupredoxins. *J. Am. Chem. Soc.* **2016**, *138* (29), 9073–9076.
(55) Küçükgüzel, I.; Ülgen, M.; Gorrod, J. W. In Vitro Microsomal Metabolism of Nuclear Chloro Substituted Secondary Amines and Imines. *Eur. J. Drug Metab. Pharmacokinet.* **1997**, *22* (4), 351–358.
(56) Bogart, J. A.; Lippincott, C. A.; Carroll, P. J.; Schelter, E. J. An Operationally Simple Method for Separating the Rare-Earth Elements Neodymium and Dysprosium. *Angew. Chem. Int. Ed..* **2015**, *54* (28), 8222–8225.
(57) Kabsch, W. Integration, Scaling, Space-Group Assignment and Post-Refinement. *Acta Crystallogr. Sect. D Biol. Crystallogr.* **2010**, *66* (2), 133–144.
(58) Evans, P. R. An Introduction to Data Reduction: Space-Group Determination, Scaling and Intensity Statistics. *Acta Crystallogr. Sect. D Biol. Crystallogr.* **2011**, *67* (4), 282–292.
(59) Murshudov, G. N.; Vagin, A. A.; Dodson, E. J. Refinement of Macromolecular Structures by the Maximum-Likelihood Method. *Acta Crystallogr. D. Biol. Crystallogr.* **1997**, *53* (3), 240–255.
(60) Adams, P. D.; Afonine, P. V; Bunkóczi, G.; Chen, V. B.; Davis, I. W.; Echols, N.; Headd, J. J.; Hung, L.-W.; Kapral, G. J.; Grosse-Kunstleve, R. W.; McCoy, A. J.; Moriarty, N. W.; Oeffner, R.; Read, R. J.; Richardson, D. C.; Richardson, J. S.; Terwilliger, T. C.; Zwart, P. H. PHENIX: A Comprehensive Python-Based System for Macromolecular Structure Solution. *Acta Crystallogr. D. Biol. Crystallogr.* **2010**, *66* (2), 213–221.
(61) Emsley, P.; Cowtan, K. Coot: Model-Building Tools for Molecular Graphics. *Acta Crystallogr. D. Biol. Crystallogr.* **2004**, *60* (Pt 12 Pt 1), 2126–2132.

APPENDIX A

Supplemental Information

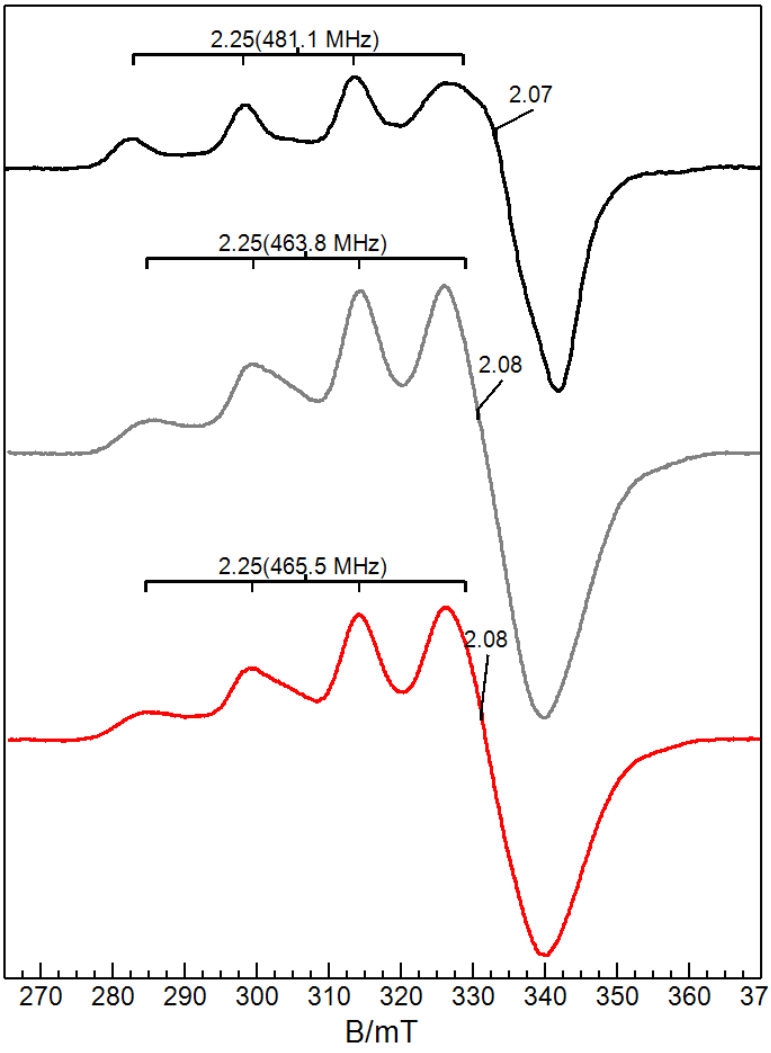

Figure A-1. EPR spectra for $[Cu^{II}(biot\text{-}et\text{-}dpea)Cl_2]H_2O$ (black), $[Cu^{II}(biot\text{-}pr\text{-}dpea)Cl_2]H_2O$ (grey), and $[Cu^{II}(biot\text{-}bu\text{-}dpea)Cl_2]H_2O$ (red).

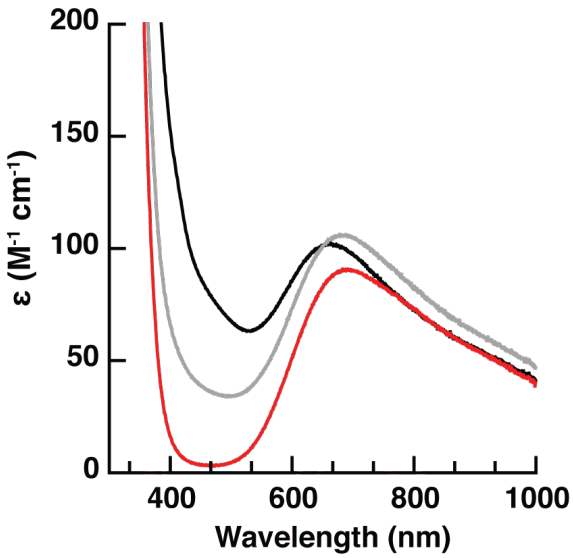

Figure A-2. UV-vis spectra for $[Cu^{II}(biot\text{-}et\text{-}dpea)Cl_2]H_2O$ (black), $[Cu^{II}(biot\text{-}pr\text{-}dpea)Cl_2]H_2O$ (grey), and $[Cu^{II}(biot\text{-}bu\text{-}dpea)Cl_2]H_2O$ (red).

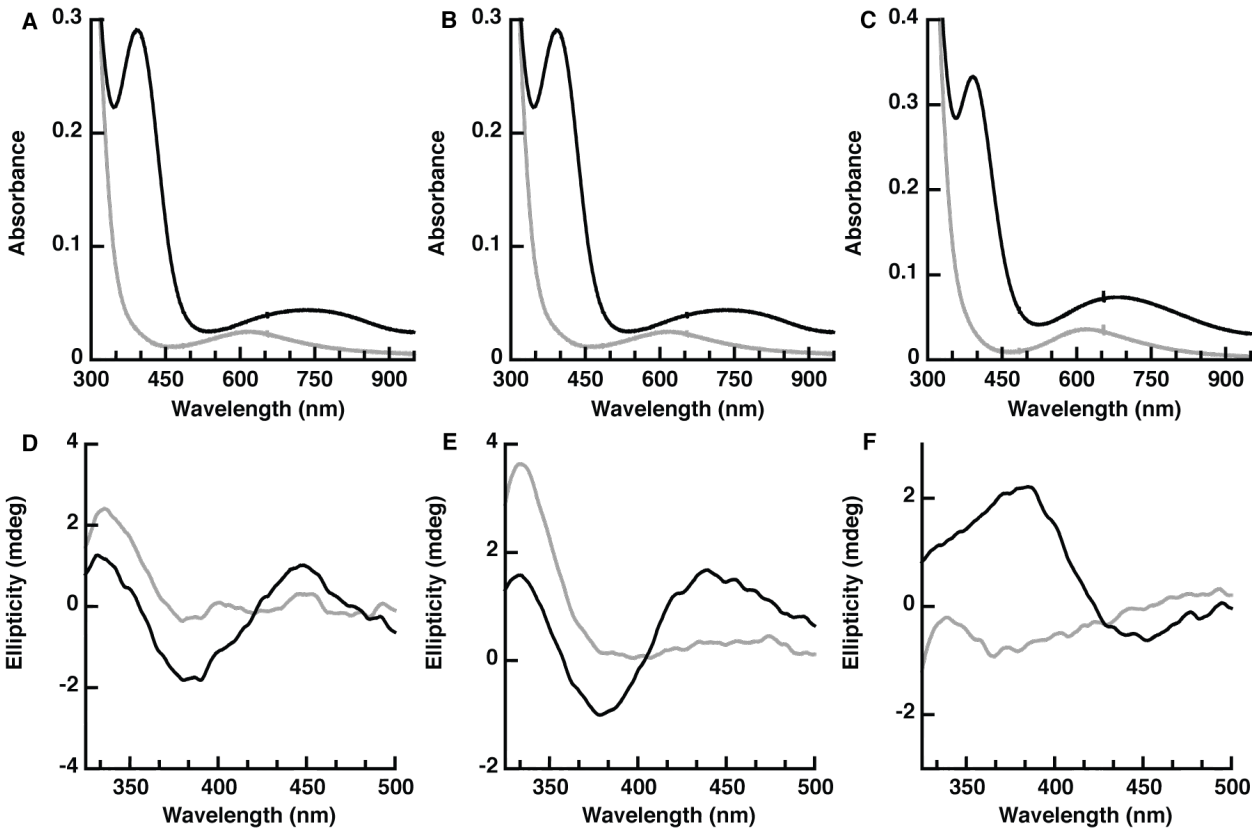

Figure A-3. UV-vis and CD spectra before (grey) and after (black) addition of NaN_3 to **3a** (**A&D**), **4a** (**B&E**), and **5** (**C&F**).

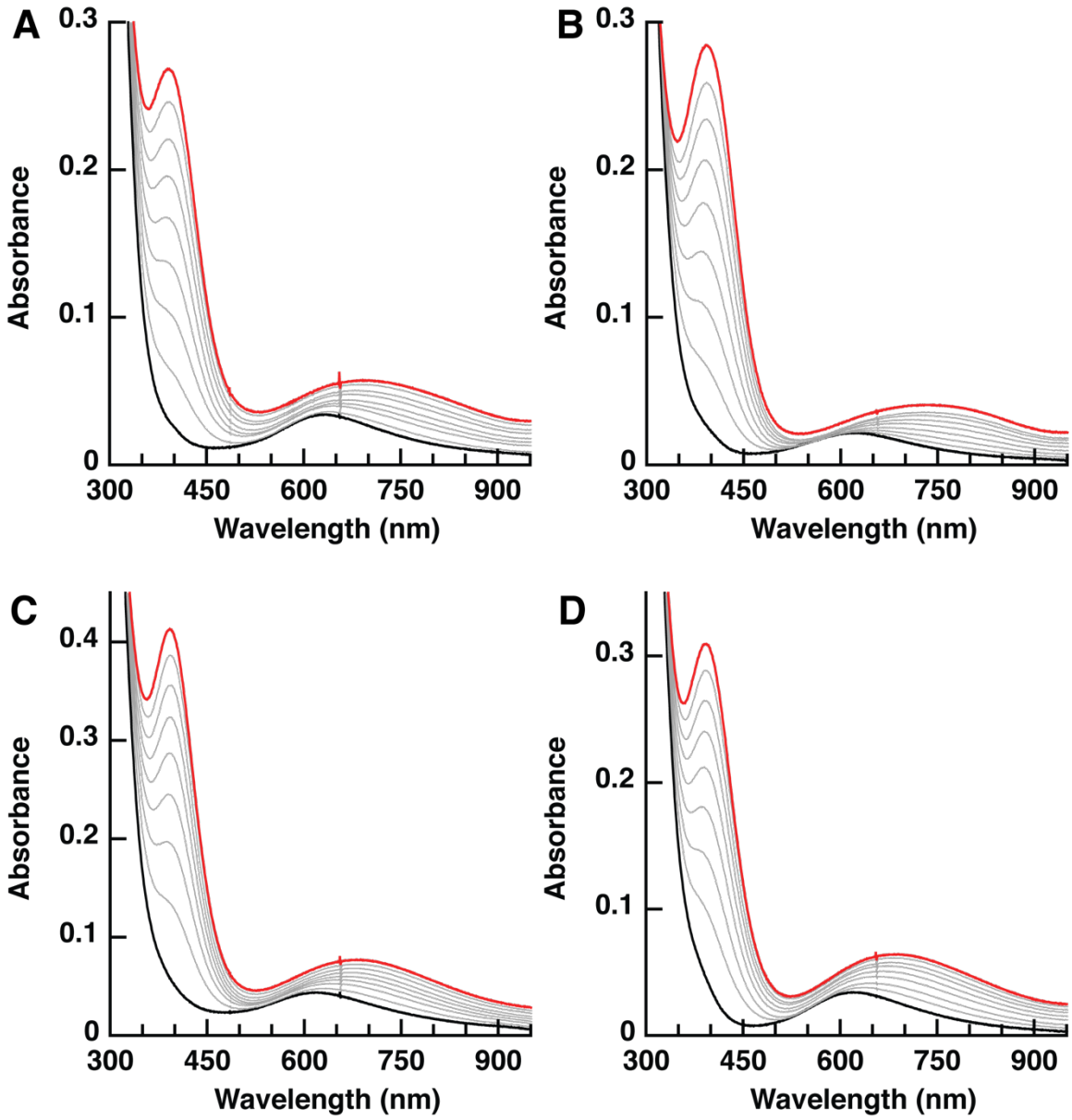

Figure A-4. Spectrphotometric titrations of **3a/3a-N$_3$** (**A**), **4a/4a-N$_3$** (**B**), **1b/1b-N$_3$** (**C**), and **5b/5b-N$_3$** (**D**). Initial spectra are in black and final are in red.

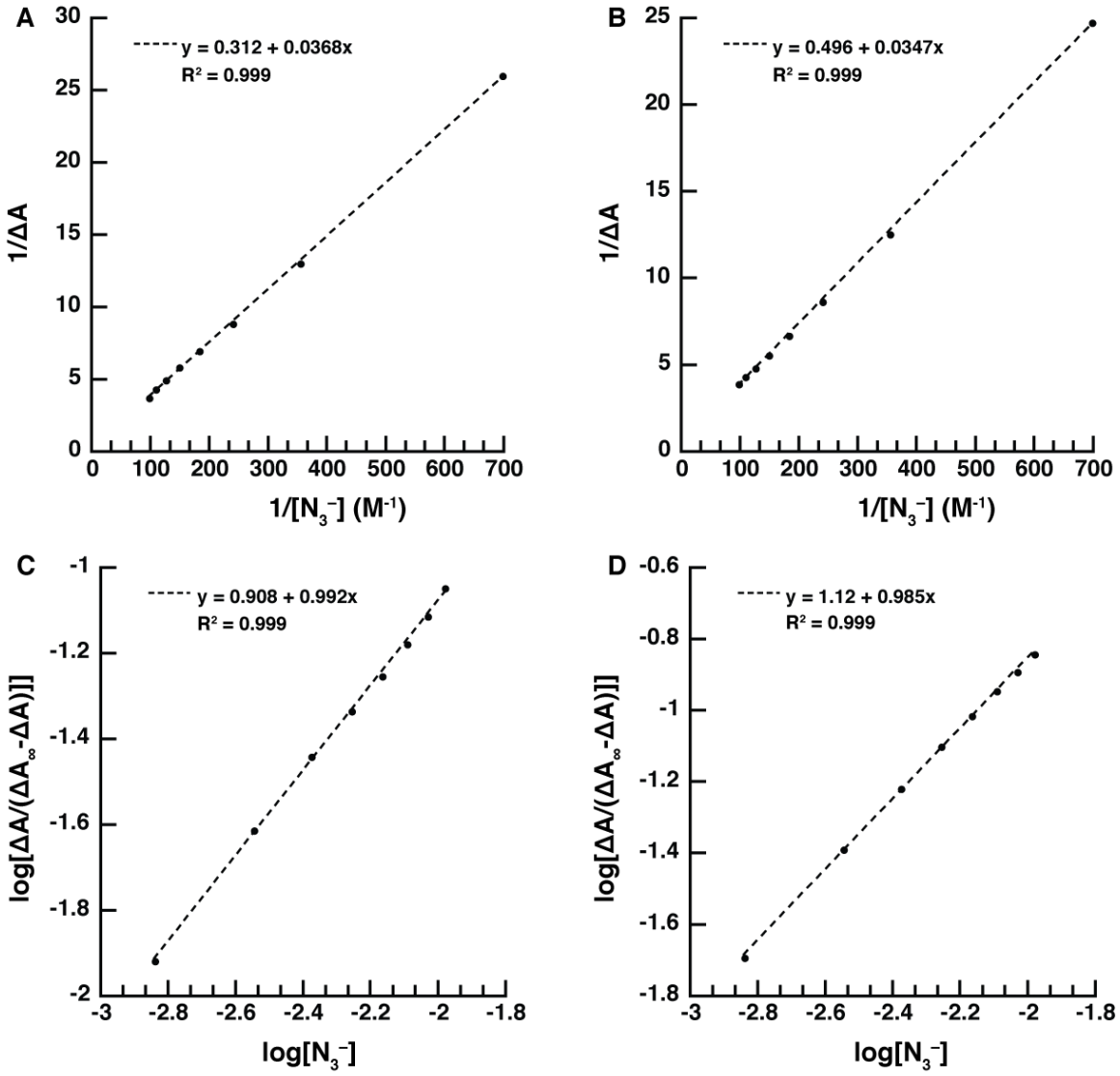

Figure A-5. Double reciprocal plots for **3a-N$_3$** (**A**) and **4a-N$_3$** (**B**) and Hill equation plots for **3a-N$_3$** (**C**) and **4a-N$_3$** (**D**).

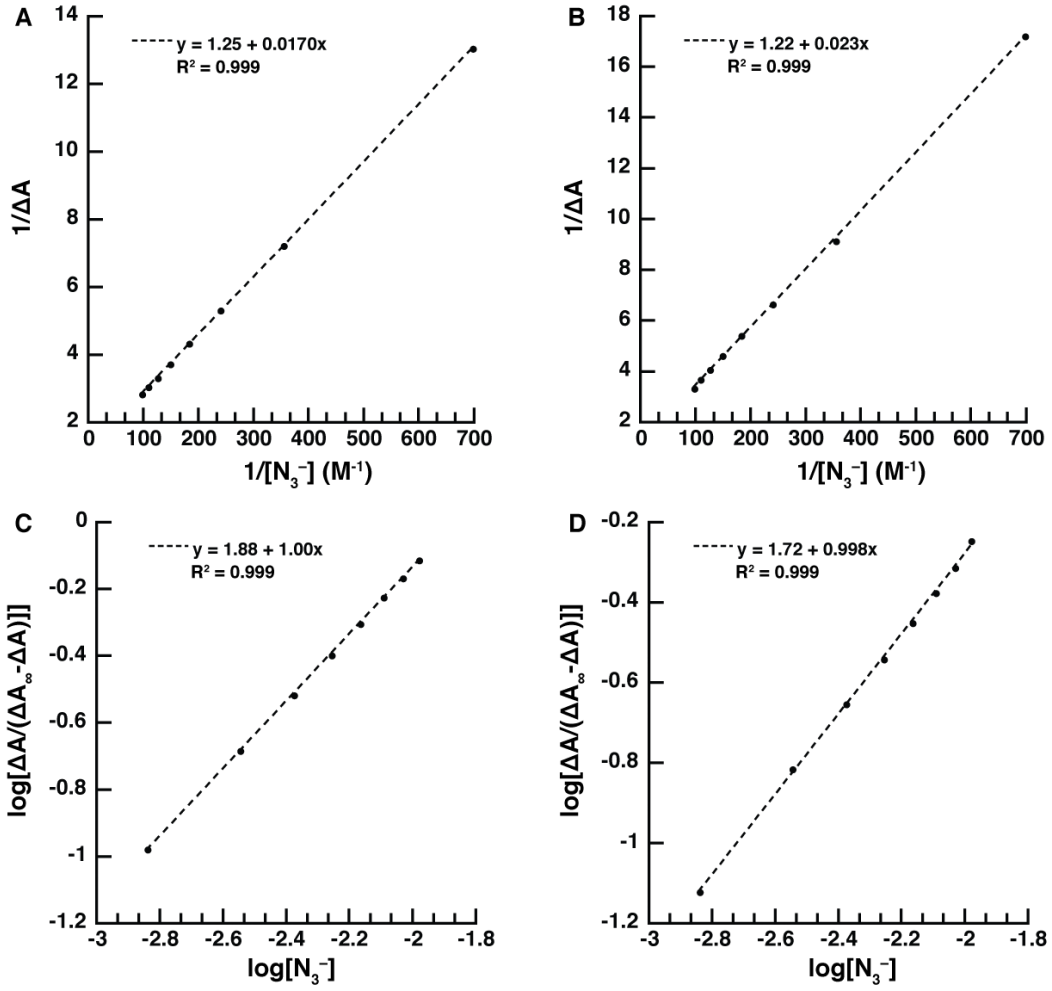

Figure A-6. Double reciprocal plots for **1b-N$_3$** (**A**) and **5b-N$_3$** (**B**) and Hill equation plots for **1b-N$_3$** (**C**) and **5b-N$_3$** (**D**).